Numerical Studies of Heavy Precipitation over West Java in January–February 2007

Nurjanna Joko Trilaksono

January 2012

Abstract

Risk of natural disasters related to severe weather is increasing due to global warming, particularly in Southeast Asia. Moreover, utilization of probabilistic information obtained from ensemble numerical weather predictions is a challenging subject for prevention of meteorological disasters. This study uses a regional non-hydrostatic model with a time-lagged ensemble forecast method to investigate a heavy precipitation event over West Java, Indonesia in January–February 2007. The study is comprised of two parts. First, we examine temporal modulation of three-dimensional synoptic fields and precipitation in the periods before, during and after the heavy rainfall over Jakarta, West Java in January–February 2007. Second, we examine dependence of simulated heavy precipitation by the model on the horizontal resolution (2, 4, 5, and 20 km). Each part includes statistical analysis of precipitation to utilize the probabilistic information obtained from the ensemble simulations.

To investigate the temporal modulation of the synoptic fields and precipitation, we perform a numerical experiment with a 20-km resolution for two-month period from January to February 2007. A comparison between the numerical results and the Tropical Rainfall Measuring Mission 3B42 data shows a fundamental agreement on the temporal modulation of the spatial distributions of precipitation, as well as the surface winds in the model and the QuikSCAT data. In addition to the modulation of precipitation, we investigate modulation of meridional winds, temperature, and relative humidity, finding that several monsoon surges are observed during the two months, but only the surge related to the Jakarta flood was a cold one. The top of the cold northerly is about 1.5 km above the surface. The cold surge event was preceded by Borneo vortex event, which is dominated by a cyclonic vortex around Borneo, Indonesia with a horizontal scale of 1000 km and a vertical scale of 3 km.

An analysis of cumulative distribution functions on the time scale of pentad shows the modulation of the probability of precipitation rate. In pentad 7 (31 January–4 February), which includes the heavy rainfall event, the fraction of the area with precipitation is the highest and the contribution of heavy rainfall to the total amount is one of the highest in

the two-month period. The diurnal cycle of occurrence of heavy rainfall is also modulated; in pentad 7, a semidiurnal variation becomes dominant, and the largest peak appears in the early morning.

To investigate the dependence of the model-simulated heavy precipitation on the horizontal resolution of the model, we perform ensemble hindcast experiments for the five-day period from 0000 UTC 31 January to 2300 UTC 4 February 2007, when the Jakarta flood event occurred. The model runs with horizontal resolutions of 2, 4, and 5 km downscaled from the 20-km runs demonstrate the ability to reproduce a region of strong convective activity to the north of Java Island during the event. Daily meridional propagation of enhanced precipitation signals is simulated in the model runs with 2- and 4-km resolutions.

Cumulative distribution functions of precipitation rate in the model are analyzed for four different regions: ocean, northern coast, mountain, and southern coast. The northern coast region shows the highest contribution of heavy precipitation compared to other regions for all the experiments as well as for satellite-based precipitation estimates. The statistics on the frequency of heavy precipitation show that the diurnal variation of heavy precipitation produced by the model with a 2-km resolution agrees well with that of satellite-based precipitation estimates.

Acknowledgments

Alhamdulillah. The author would like to express his gratitude to Professor Shigeo Yoden who providing an opportunity to the author to conduct this study. The author thanks Dr. Shigenori Otsuka for numerous helpful discussions and comments, kindly guidance, and technical support for the research; the author deeply indebted to him for his help. The author wishes to thank Prof. Takehiko Satomura, Prof. Hirohiko Ishikawa, Prof. Masato Shiotani, Dr. Tetsuya Takemi, Dr. Keiichi Ishioka, Dr. Yoko Naito for their helpfull comments.

The author acknowledges help from Dr. Kazuo Saito, who give the opportunity to have internship training at Research and Forecast Laboratory, Meterological Reseach Institute Tsukuba. Thanks are extended to Mr. Syugo Hayashi and Mr. Takuya Kawabata, who willing to share their knowledge to the author, and including but not limited to Dr. Hiromu Seko, Dr. Yoshinori Shoji, and other Forecast Research Department members.

The author would like to thank Mr. Katsumasa Sumida and Mr. Takuya Yuasa, who help him in the early life in Kyoto. He also thanks others member of Meteorology Laboratory, Mr. Naoaki Saito, Mr. Hiroki Yamamoto, Mr. Kazuhiro Nishimura, Mr. Masashi Harada, Mr. Kenshi Hibino, Mr. Keiji Uematsu, Ms. Kayo Sakurai, Ms. Megumi Takeshita, Mr. Izumi Saito, Mr. Shunsuke Noguchi, Mr. Shinya Tsuchida, Mr. Toshiki Matsushima, and Mr. Naoki Matsumoto, who have been studied together in the Lab. The author has to be grateful to Ms. Fumiko Furutani and Ms. Yoko Uemoto for their assistance and guidance on the administrative works, including Dept. of Geophysics, Kyoto University office staff, Ms. Yumi Aoshima.

Special thanks go out to Dr. Tri Wahyu Hadi, who has had encouraged the author to pursue better higher education and has given his support. Dr. Apip provided hourly data from BMKG.

Finally, the author gratefully acknowledges the financial supports received from Directorate General of Higher Education (DIKTI), Department of National Education of

Republic of Indonesia, Japanese Ministry of Education, Culture, Sports, Science, and Technology (MEXT) Special Coordination Funds for Promoting Science and Technology for FY 2007–2009 “International Research for Prevention and Mitigation of Meteorological Disasters in Southeast Asia”, and Kyoto University Global COE Program 2009–2014 “Sustainability/Survivability Science for a Resilient Society Adaptable to Extreme Weather Conditions”. And of course the author is grateful to Prof. Kaoru Takara, the leader of GCOE-ARS.

Contents

List of Figures

List of Tables

Chapter 1

General Introduction

1.1 The Jakarta flood event in February 2007

Indonesia, which lies between the latitudes of 11°S and 6°N, and longitudes of 95°E and 141°E (Fig. 1.1a), is one of the most disaster-prone countries in the world due to multiple hazards, according to a fact World Bank report (Dilley et al. 2005). To cope with the situation, the Indonesian government established a national agency named "National Disaster Management Agency" (BNPB). The missions of the agency are to protect the nation from the threat of disasters through risk reduction, to build a reliable system of disaster management, and to conduct disaster management in a planned, integrated, coordinated, and comprehensive way (see `http://bnpb.go.id`). To achieve these missions, the agency is developing a web-based, conceptual and methodological tool for the construction of databases of loss, damage, or effects caused by emergencies or disasters. The compiled databases are expected to support BNPB by enhancing disaster management capabilities at both the national and local levels, supporting the fast and appropriate reporting of disasters, and providing complete and up-to-date information regarding all parties associated with disaster management in Indonesia and also foreign countries through global facilities.

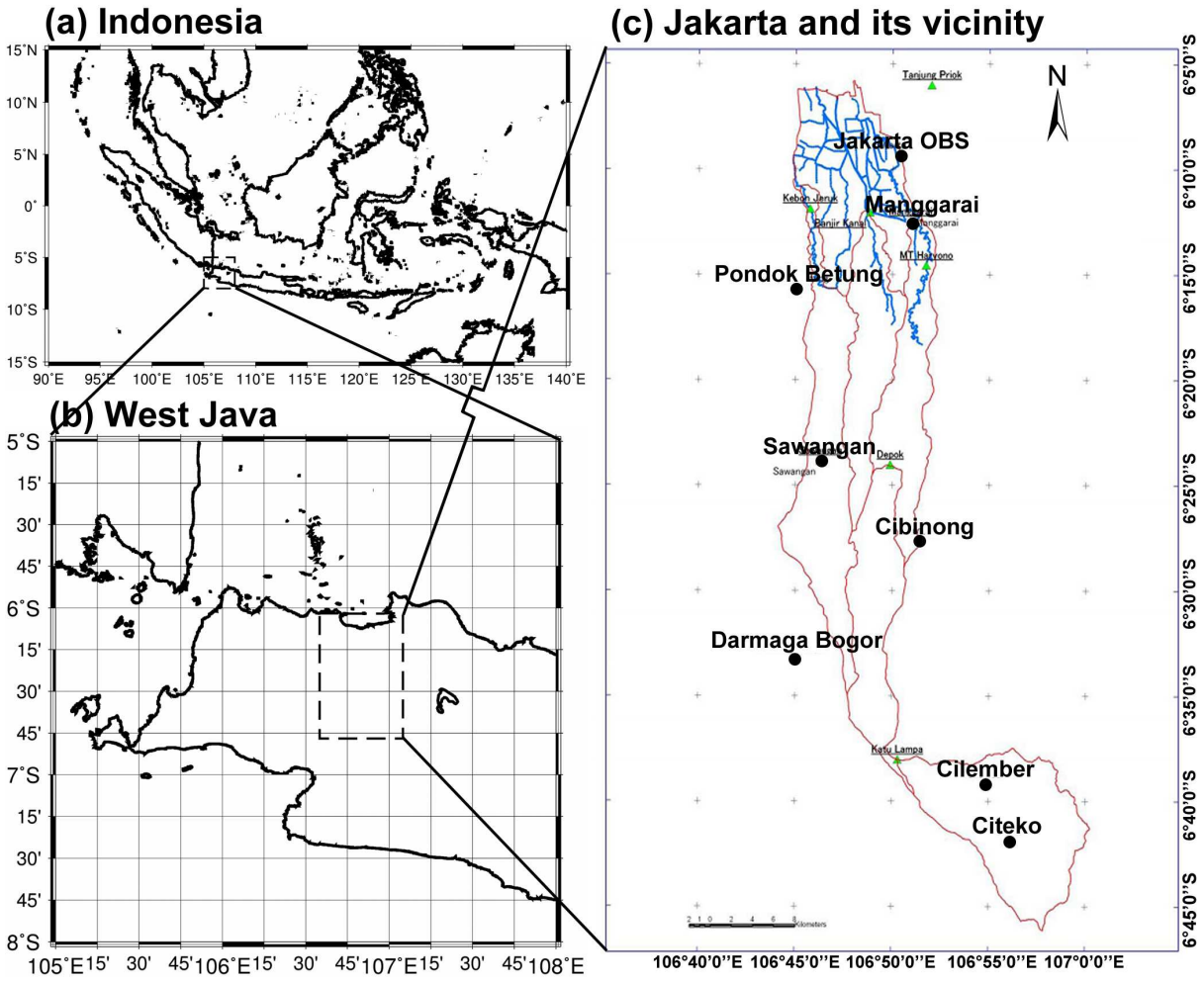

Figure 1.1: Map of (a) Indonesia, (b) West Java, and (c) river stream flow through Jakarta and its vicinity.

Among the multiple hazards affecting Indonesia, natural disasters related to severe weather events (e.g., floods and landslides caused by heavy rainfall) are one of the major causes of socio-economic losses and damages. The dates and places of several such severe disasters and their losses and damages are given in Table 1.1, as found in the Indonesian Disaster Data and Information (DiBi) database compiled by the BNPB (available online at `http://dibi.bnpb.go.id`) for the period from 1 January 2002 to 31 December 2008. From the table we see that the Jakarta flood event on 1 February 2007 was the largest in terms of the number of victims evacuated and houses damaged, although the number of the dead was smaller than those for other events. It is important to note that Jakarta, which is located in West Java (see Fig. 1.1b), is the capital city of Indonesia, where

Table 1.1: Numbers of affected people and damaged houses due to natural disasters associated with severe weather events in Indonesia for the period from 1 January 2002 to 31 December 2008. Data from the National Disaster Management Agency (BNPB) of Republic of Indonesia.

Event	Date	Province	Killed	Injured	Evacuated	Damaged Houses
Floods	2003/11/02	Sumatra Utara	160	50	2080	437
	2007/02/01	**DKI Jakarta**	**48**	**484**	**521389**	**24957**
Floods and Landslides	2002/12/11	Jawa Timur	32	11	-	-
	2003/01/28	Jawa Barat	59	74	1796	168
	2006/01/01	Jawa Timur	92	68	7644	397
	2006/06/01	Sulawesi Selatan	210	18	7858	972
	2007/01/12	Sulawesi Utara	32	14	5361	589
	2007/03/02	Nusa Tenggara Timur	43	32	5818	92
	2007/07/22	Sulawesi Tengah	76	2371	17078	240
	2007/12/26	Jawa Tengah	62	85	501	1590
Landslides	2004/03/26	Sulawesi Selatan	33	16	200	484
	2004/04/23	Sumatra Barat	43	14	-	-
	2005/02/21	Jawa Barat	137	-	315	80
	2006/01/04	Jawa Tengah	76	16	587	104
	2006/12/24	Sumatra Utara	34	12	3050	22

economic, cultural, and political activities of the country are centered. Thus, the losses and damages caused by a disaster should be greater than those in the other cities.

The Jakarta flood event in February 2007 was a major one, with a recurrence interval of 10–20 years. The previous such flood occurred in 1996, when 1190 km^2 of land were flooded (Brakenridge cited 2011). Figure 1.2 shows some photographs of the conditions in Jakarta and its vicinity during the event. As seen in Fig. 1.2, many people evacuated from their homes to temporary shelters such as schools and mosques. About 70% of the area in Jakarta was inundated by water, with the height of the water varying from 30 cm up to 4 m in parts of city (BAPPENAS 2007). Note that there is an annual flood in some parts of Jakarta, particularly in the northern part of the city due to the city's location at the mouth of the rivers flowing from the Puncak highlands and due to the elevation of land below sea level (see Fig. 1.1c).

Figure 1.2: Some photographs taken during the Jakarta Flood event in February 2007 (Photos credit: http://www.flickr.com/photos/indahs/379157723 and http://news.bbc.co.uk/2/hi/asia-pacific/6328873.stm).

The most significant reason for the Jakarta flood event in February 2007 was the high rate of precipitation. Figure 1.3 shows the time series of hourly precipitation (mm hr^{-1}) in Jakarta and its vicinity, with each weather station location shown in Fig. 1.1c. Heavy precipitation occurred for three days, from 31 January to 2 February 2007 in Jakarta Obs., Manggarai, and Pondok Betung. The heavy precipitation occurred twice a day: near the midnight and in the morning, with the heaviest (67 mm hr^{-1}) occurring at 2300

LT (LT denotes local time at Jakarta, UTC +7) on 31 January 2007 at the Pondok Betung Station (6.2°S, 106.6°E). Stations to the south of Jakarta experienced little precipitation during this 3-day period, except Cilember and Citeko, which saw heavy precipitation on 1 February and Sawangan on 1 and 2 February.

It is common to experience heavy precipitation in January–February, since it is the rainy season on Java Island, which includes the Jakarta area (e.g., Hamada et al. 2002; Aldrian and Susanto 2003). The peak of the rainy season in January coincides with the northwest monsoon across the Austral–Indonesian region (Hendon 2003). However, in such a case, the impact of the northwest monsoon is amplified by a synoptic-scale disturbance from the Northern Hemisphere, as previously reported by Wu et al. (2007) for the Jakarta flood event in February 2007. They have investigated the influence of the cross-equatorial monsoon flow on the formation of repeated torrential rains over the island using QuikSCAT sea surface winds, Geostationary Meteorological Satellite (GMS) infrared images, radar observation and balloon sounding data for the period from late January to early February 2007.

Figure 1.4 shows the time–latitude cross sections of sea surface meridional winds from QuikSCAT along 108°E for the period from 10 October 2006 to 1 April 2007 (Wu et al. 2007). A strong northerly wind (> 10 m s^{-1}) occurred 4 times over the South China Sea: in late October to early November, in the beginning and middle of December 2006, in mid-January, and in late January to early February 2007. In the last and strongest event, which started on 28 January 2007, the strong northerly monsoon blew across the equator and penetrated into the northern part of Java in the Southern Hemisphere. The strong cross-equatorial monsoon persisted for more than one week during the period from late January to early February 2007.

The short report by Wu et al. (2007) only focused on the behavior of meridional wind, whereas other parameters such as temperature and humidity were not considered. The vertical structure of the meridional winds, their temperature, and relative humidity during this period were also not well described.

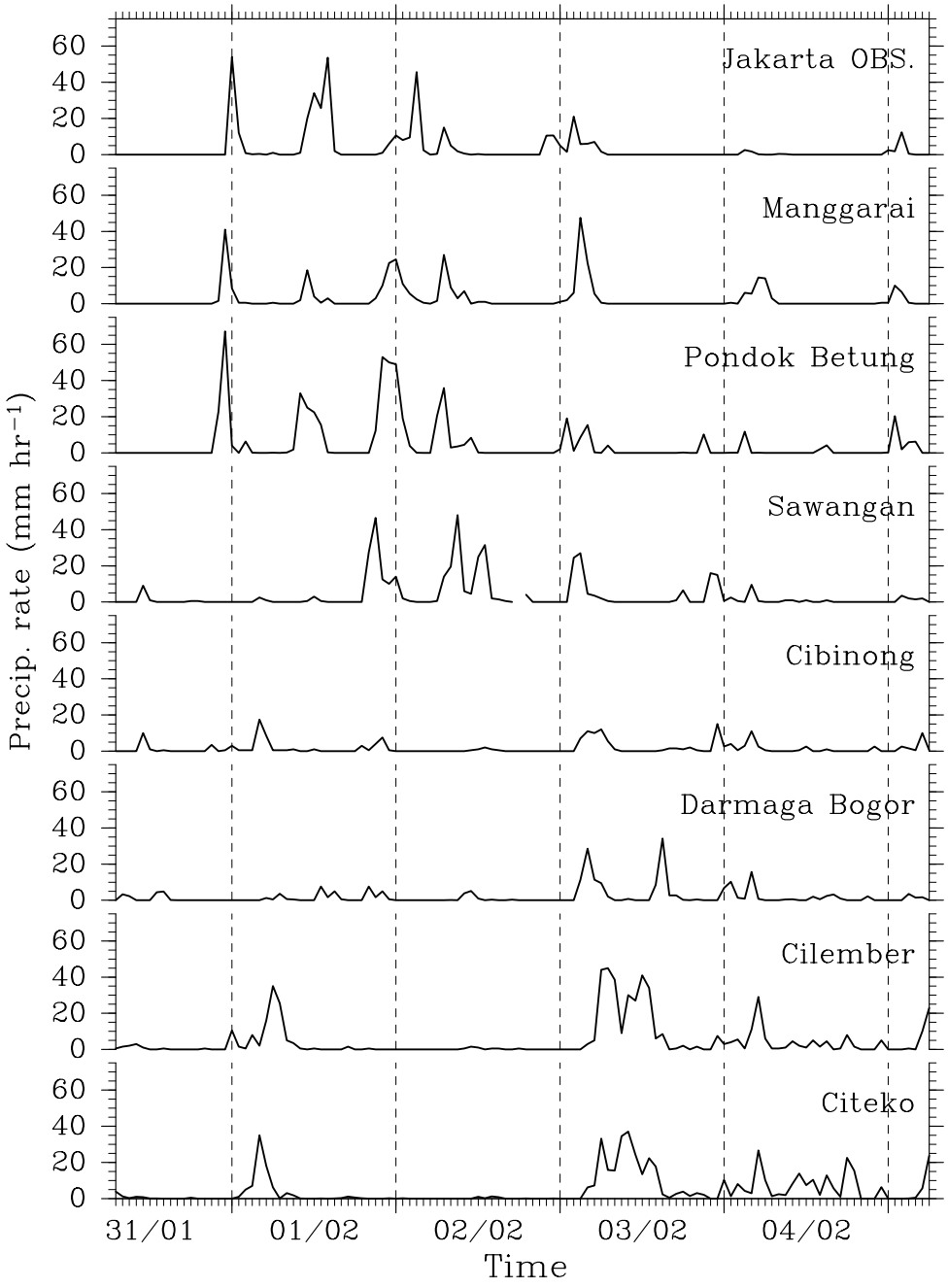

Figure 1.3: Time series of hourly precipitation from eight stations in Jakarta and its vicinity. The time is local time in Jakarta (UTC +7). The data are provided by Dr. Apip.

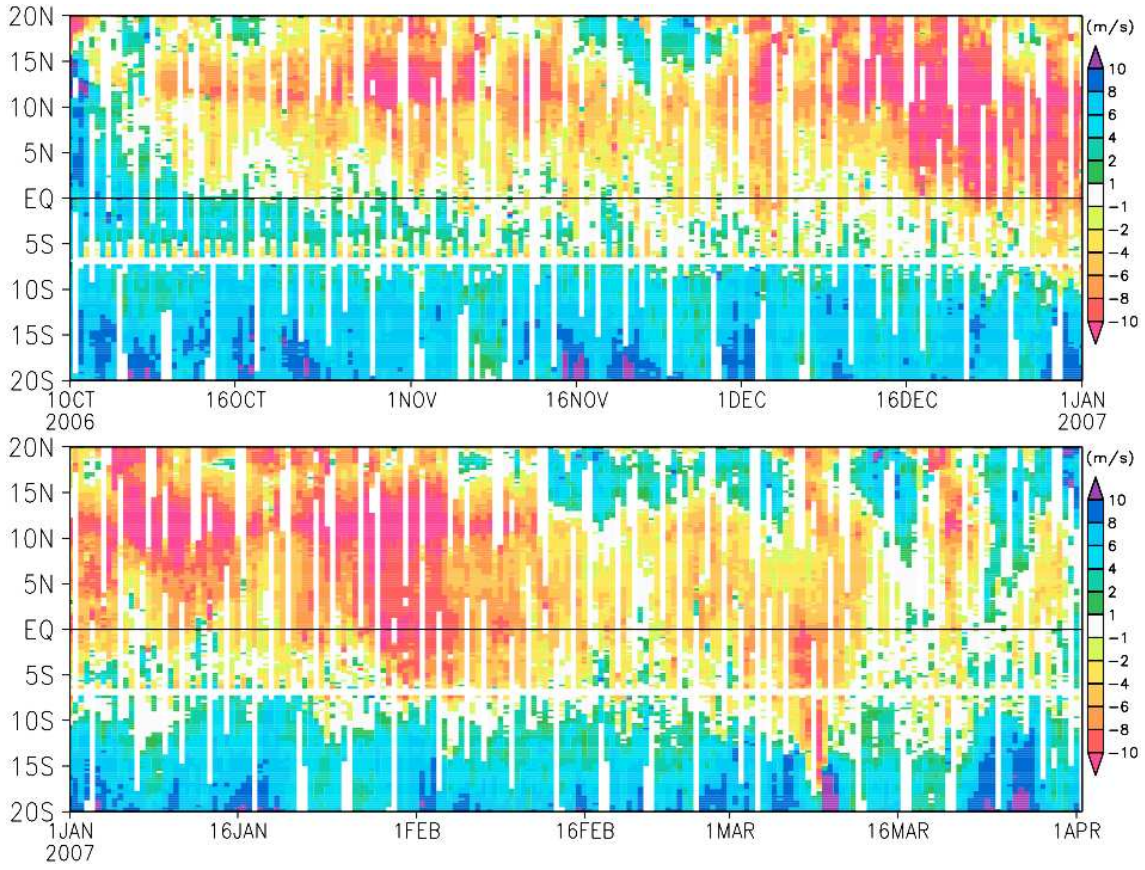

Figure 1.4: Time–latitude diagram showing the meridional winds from QuikSCAT sea surface winds along 108°E (from Wu et al. 2007).

1.2 Data analyses of heavy precipitation and synoptic conditions in the Southeast Asia

Most precipitation in Southeast Asian countries is brought by summer, winter, or both monsoons, where the annual amount exceeds 1500 mm with a very clear seasonal variation of precipitation (e.g., Matsumoto 1997; Wang and LinHo 2002). In many parts of Indonesia, the Malay Peninsula, and the Mekong River basin, massive floods often follow torrential monsoon rains. This situation gives rise to concern and interest among researchers in Southeast Asia to study the weather and climate in their respective regions. One of the examples is the Professor Tangang's group from the National University of Malaysia, which has done a considerable amount of research on weather system and interannual variability of heavy precipitation in Malaysia.

One of the works from the Tangang group relevant to the present study is the analysis of the extreme precipitation that resulted in floods in southern Peninsular Malaysia in the mid- and late December 2006 and mid-January 2007, before the Jakarta flood (Tangang et al., 2008). Figure 1.5 shows the accumulated rainfall for the first (Fig. 1.5a), second (Fig. 1.5b), and third extreme precipitation episodes (Fig. 1.5c) and the 925 hPa winds and divergence (shaded) during the beginning of each extreme episode: 0000 UTC 17 December 2006 (Fig. 1.5d), 0000 UTC 26 December 2006 (Fig. 1.5e), and 0000 UTC 11 January 2007 (Fig. 1.5f). The 925 hPa winds and divergence during 0000 UTC 30 December 2006 are also shown in Fig. 1.5g. The three extreme precipitation episodes occurred during a period of stronger northeasterly winds over the southern South China Sea (Figs. 1.5a–f). In all three episodes, there were strong easterly winds from the western Pacific. Only during the first episode the strongest equatorward spread of the cold surge from eastern Asia was evident. During the second and third episodes, the cold surge outflow was weak. They showed that the extreme precipitation events were associated with the strong northeast cold surge which interacted with other synoptic systems such as the Madden–Julian Oscillation (MJO) or the Borneo vortex (e.g., Cheang 1977, see Fig. 1.6 for the illustration). It is a cyclonic vortex with a horizontal scale of 1000 km around Borneo (Kalimantan), Indonesia.

A schematic diagram illustrating the typical geographical distribution of winter monsoon circulation systems and convection is presented in Fig. 1.6 (Johnson and Houze 1987). During the boreal winter monsoon, primary synoptic-scale circulation features include a cold surge, a cross-equatorial monsoon flow, and a Borneo vortex. These disturbances affect the cloudiness and rainfall in the South China Sea, and the Maritime Continent. Deep convection and heavy rainfall can occur throughout the entire tropical monsoon region; however, these phenomena are normally concentrated in areas where local and regional forcing is maximal.

Another example of a strong cold surge that had a role in a heavy rainfall event in Thailand was reported by Wangwongchai et al. (2005) for the case study of 20–23 November 2000. In that case, the cold surge blew southwestward over the South China

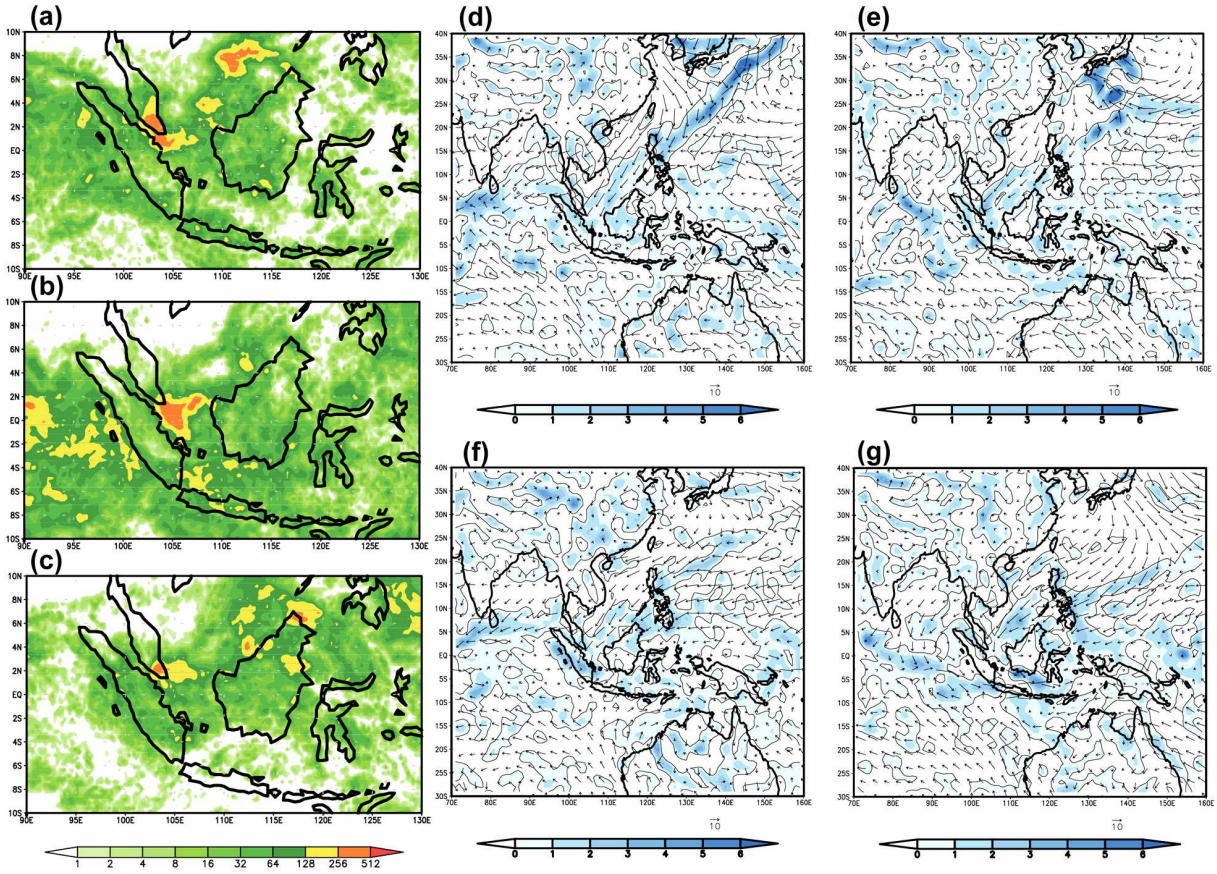

Figure 1.5: (a)–(c) Accumulated rainfall for first, second and third extreme precipitation episodes, respectively, the unit is mm. (d)–(g) The 925 hPa winds (m s^{-1}) and divergence (shaded, $10^{-5}s^{-1}$) during the beginning of each extreme episode (d) 0000 UTC 17 December 2006, (e) 0000 UTC 26 December 2006 and (f) 0000 UTC 11 January 2007. (g) The 925 hPa winds and divergence during 0000 UTC 30 December 2006, when there was no heavy precipitation over southern Peninsular Malaysia (from Tangang et al. 2008).

Sea, which turned into southeastward at 5°N, forming a cyclonic circulation over Malaysia and Sumatra. This circulation was associated with the maximum of the convergence of total moisture flux near South Thailand, which was favorable for the occurrence of the heavy rainfall.

In a recent work, Chang et al. (2005) documented the impact on deep convection due to the interactions among three different motion systems — the northeast cold surge, the synoptic-scale Borneo vortex, and the intraseasonal MJO. Figure 1.7 shows the impacts of the cold surge and the Borneo vortices on deep convection. When neither a surge nor a vortex is present (Figs. 1.7a,e), convection is reduced over the equatorial South China Sea

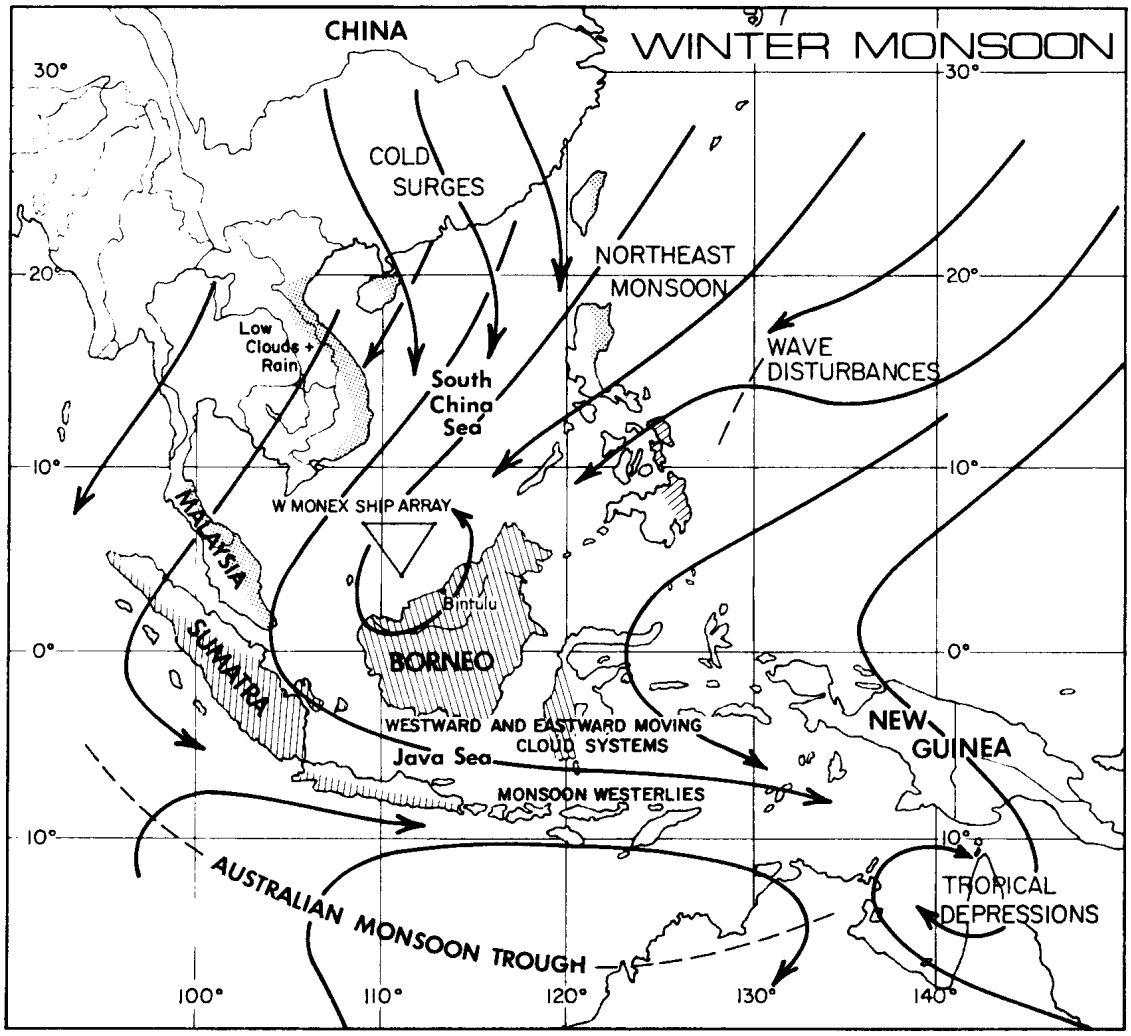

Figure 1.6: Primary synoptic-scale circulation features that affect cloudiness and precipitation in the region of the winter monsoon. Convection associated with land and sea breeze circulations exists throughout the maritime continent. Preferred coastal locations of enhanced low-level cloudiness and rainfall associated with the northeast monsoon and cold surges are indicated (stipples); cloudiness maxima over water are omitted. Hatching denotes 1 November to 30 April precipitation west of 130°E exceeding 150 cm (from Cobb and Coleby 1966). The winter MONEX ship array (6–28 December 1978; southernmost ship moved 1° south of indicated position after 17 December) is shown (from Johnson and Houze 1987).

and enhanced to its west, southwest, and south. The area of reduced convection is also an area of low-level divergence. This pattern is almost reversed when a vortex is present without a cold surge (Figs. 1.7b,f). It appears that the Borneo vortex acts to intercept transport of low-level moisture by the northeasterly monsoon flow, such that convection

over the Malay Peninsula–Java region is reduced. The presence of a cold surge basically enhances these two opposite patterns. Without a vortex (Figs. 1.7c,g), the surge acts to reduce deep convection over the equatorial South China Sea, where there is also low-level divergence, and increase convection and low-level convergence over the surrounding regions of the Malay Peninsula, Java, and surrounding equatorial regions. While the low-level divergence over the South China Sea is associated with increased northeasterly winds due to the cold surge, the increased low-level convergence and convection downstream over the Malay Peninsula results from the blocking of the surge winds by terrain. When both the surge and the vortex are present (Figs. 1.7d,h), convection over the southern South China Sea is strongest.

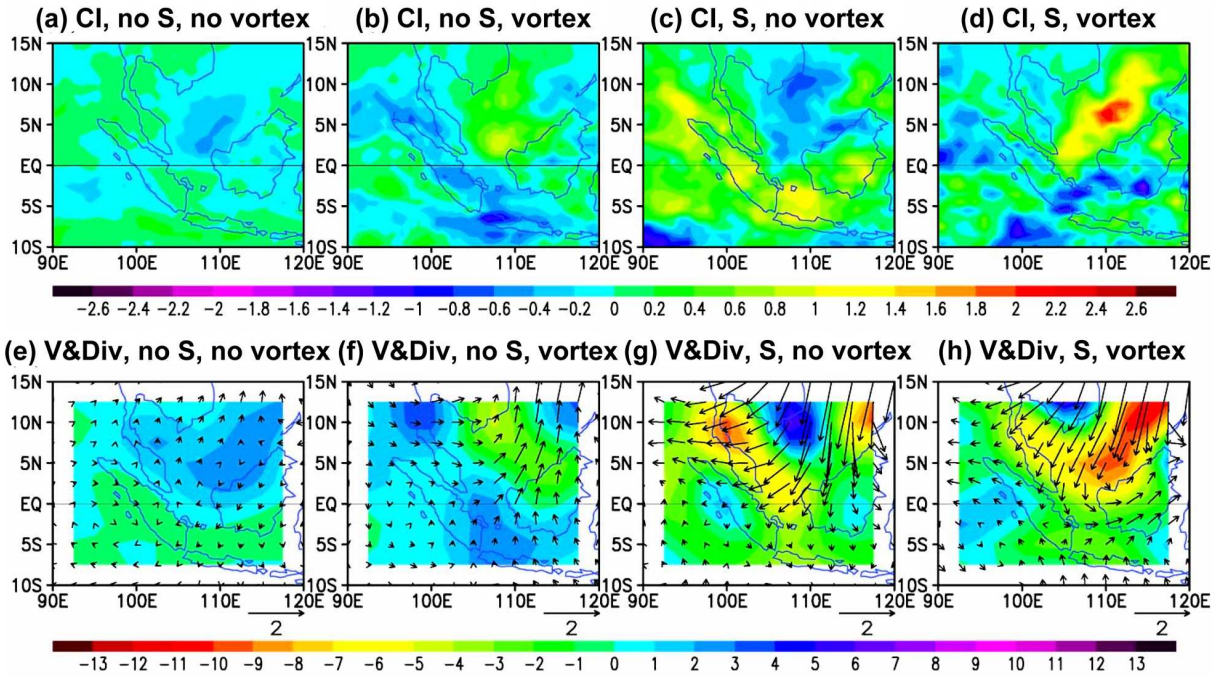

Figure 1.7: Composite maps of (top) convective index (CI) for (a) no-surge and no-vortex cases, (b) no-surge and vortex cases, (c) surge and no-vortex cases, and (d) surge and vortex cases, and (bottom) composite maps of 925-hPa winds (m s^{-1}) and divergence (shaded, 10^{-5} s^{-1}) for (e) no-surge and no-vortex cases, (f) no-surge and vortex cases, (g) surge and no-vortex cases, and (h) surge and vortex cases (from Chang et al. 2005).

During strong surge events, stronger winds occur over East Asia and the South China Sea. About five days after strong surge events over the South China Sea, cross-equatorial flows occur over the Indonesian region, which thereafter influence the circulation pattern

over Indonesia and northern Australia (Suppiah and Wu 1998). The extension of cold surges crossing the equator is primarily due to the strengthening of the northeasterly near the surface. The flow is restricted by topography such that it is channeled toward the equator (Chang et al. 2005); the layout of Indonesian islands enables cold surges to reach Java Island. Cold surges are typically dry, but as they pass over the South China Sea, they become moist (Johnson and Houze 1987). Such conditions are favorable for moist convections to develop. Furthermore, Hattori et al. (2011) provide convincing evidence from data analyses of 10 winters from December 2000 to March 2009 that the generation of the cross-equatorial northeasterly cold surge was an important environmental factor for inducing the wide positive precipitation anomaly compared to the climatological mean over the Maritime Continent, especially over the northern part of Java, east of the Philippines, and west of Borneo.

1.3 Numerical studies of heavy precipitation and topographic effects in the tropics

Numerical study is a powerful approach to understand the characteristics of meteorologically interesting events; it reveals physical processes of the events in detail and gives three-dimensional structures of the events and their time evolutions. However, the lack of a good observation network over the tropics, in particular Southeast Asia, has arguably hampered the understanding of regional weather (Koh and Teo 2009). Although satellite observations fill in much of the gaps in conventional data coverage, some limitations still exist, e.g. temporal resolution of less than 1 hour and spatial resolution less than 20 km are not available to our knowledge. In this situation, numerical methods are a feasible alternative for investigating the regional weather systems. Until now, however, only a few numerical studies addressed extreme precipitation events related to the monsoon in tropical Asia. One example of numerical studies of heavy precipitation and topographic effects in the tropics is Juneng et al. (2007), who studied an extreme rainfall event from 9 to 11 December 2004 over the east coast of Peninsular Malaysia. Using the fifth gener-

ation of the Penn State - National Center for Atmospheric Research (NCAR) Mesoscale Model (MM5), they succeeded in simulating the spatial pattern of the accumulated 72-hr (from 0000 UTC 9 to 0000 UTC 12 December 2004) rainfall during this episode correctly, with maxima located over the eastern coast of Peninsular Malaysia near 4°N (Fig. 1.8a). Although the spatial pattern of the rainfall is similar to that of the Tropical Rainfall Measuring Mission (TRMM) data, the 72-hour accumulated rainfall in the model of 455 mm is about 70% of that observed. The band of moderate rainfall over the east coast of northern Sumatra was also well simulated by the model, despite a slight excess compared to the TRMM data. Their study revealed an important role of local topography in providing the forcing for moist air lifting, and another role of latent heat release crucial for supporting the vertical motion associated with the rainfall, as shown in Fig. 1.8b.

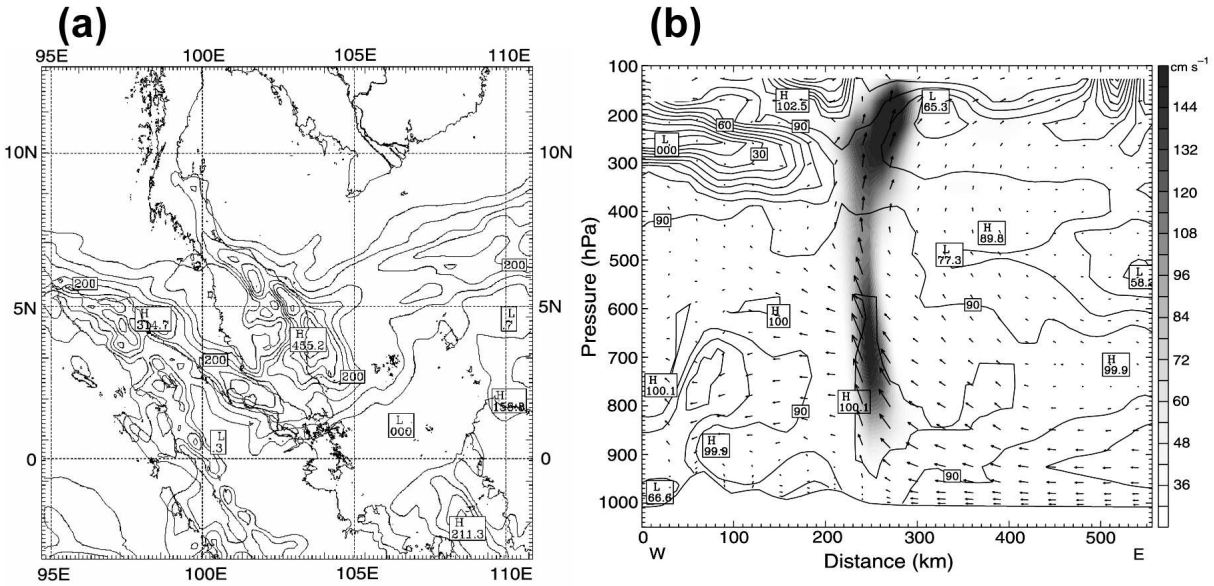

Figure 1.8: (a) 72-hour accumulated rainfall simulated by the CTRL model run. (b) Vertical cross section of wind vectors and the relative humidity (contours). The value of vertical velocity is shaded in (b) (from Juneng et al. 2007).

Seko et al. (2008) documented another example of the simulation of a heavy rainfall system in tropical Asia. An intense rainfall system that developed in Mumbai, India, on 26 July 2005 was successfully simulated with horizontal resolution of 5 km (Fig. 1.9a). The detailed structure of the rainfall system at the intense rain stage, investigated with horizontal resolution of 1 km, revealed a good agreement of the simulated position and the

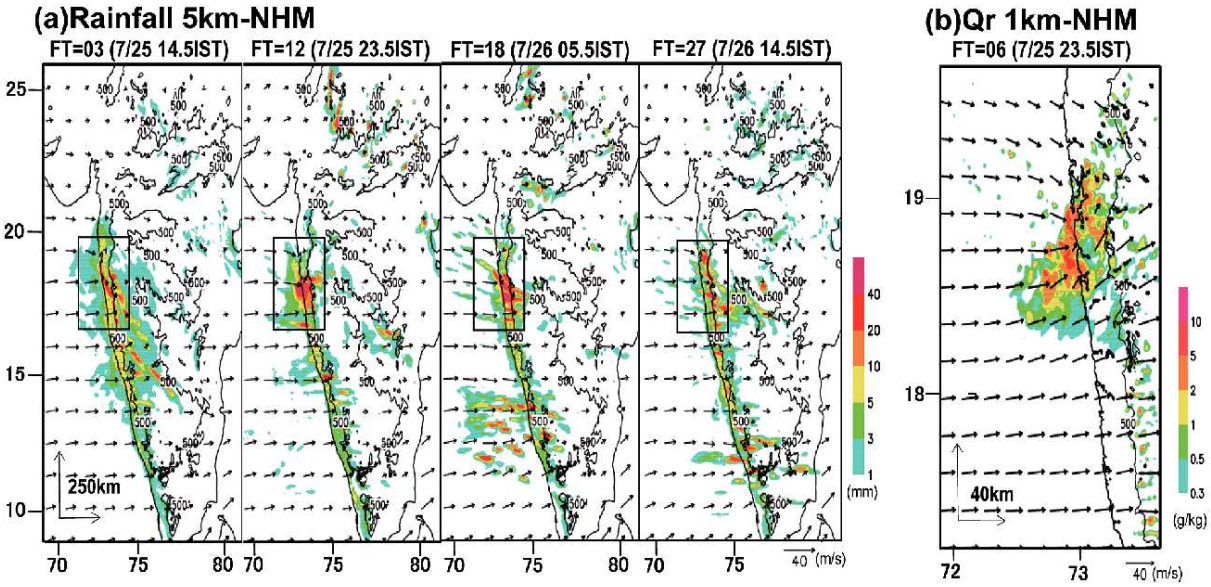

Figure 1.9: (a) Rainfall distributions from FT = 3 to 27 hours by 5-km-NHM and (b) horizontal wind and rainwater mixing ratio (Qr) at z = 0.53 km at FT = 6 hours by 1-km-NHM. Rectangles in (a) indicate the domain of (b). Large arrows in (a) and (b) indicate the horizontal scale of 250 km and 40 km, respectively (from Seko et al. 2008).

horizontal scale with observation, indicating that the resolution effectively reproduced the regional heavy rainfall (Fig. 1.9b). Increase of the horizontal resolution was a key factor for the reproduction of heavy rainfall, because the local topography with steep gradients around Mumbai was important for this occurrence.

1.4 Observational studies on the diurnal cycle of precipitation in the tropics

The diurnal cycle in tropical cloudiness and precipitation has been extensively studied for these several decades, but because of the scarcity of observational data, especially over the tropical oceans, these studies have used different data sources and have mostly been confined to limited regions (Yang and Slingo 2001). The earlier studies primarily used surface observations (e.g., Gray and Jacobson 1977; McGarry and Reed 1978; Albright et al. 1981), while later studies used various forms of satellite or radar-derived cloudiness and precipitation (e.g., Albright et al. 1985; Hendon and Woodberry 1993;

Chen and Houze 1997; Liu et al. 2007). Most of these studies showed that the convective or precipitation maximum tended to occur in the early morning over the open oceans and in the late afternoon or early evening over land.

Figure 1.10 shows regional variation of annual mean difference between morning rain (0000–1100 LT) and evening rain (1200–2300 LT) over the area observed by TRMM precipitation radar (PR) (Mori et al. 2004). It shows more rainfall in the evening than in the morning over the land region of relatively large islands, for example Sumatra, Java, and Borneo, but more rainfall in the morning than in the evening over the coastal sea regions surrounding the islands. The southwestern coastline of Sumatra, the Straight of Malacca, and surrounding coastline of Borneo, especially, show strong contrast between the evening rain over land regions and the morning rain over coastal sea regions. The amplitude of these contrasts decreases with the distance from each coastline.

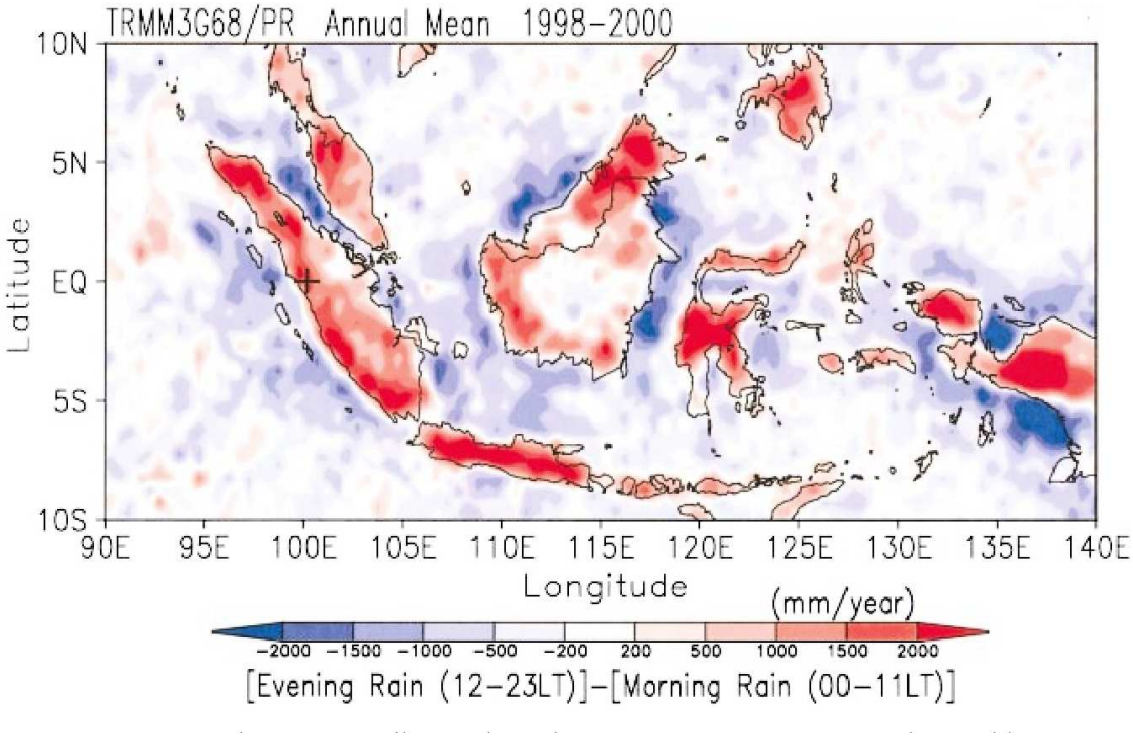

Figure 1.10: Regional variation of annual mean difference between morning rain (0000–1100 LT) and evening rain (1200–2300 LT) over the area observed by TRMM PR. Positive value indicates more rainfall observed from 1200 to 2300 LT than from 0000 to 1100 LT. The black cross (+) indicates the Kototabang GAW station (from Mori et al. 2004).

The recognized importance of the diurnal cycle in tropical precipitation distribution

was the primary reason that the TRMM satellite was designed to have a precessing rather than a sun-synchronous orbit (Simpson et al. 1996). By utilizing TRMM PR, many previous studies have shown the important role of sea and land breeze and mountain and valley breeze circulations on the diurnal cycle (Mapes et al. 2003; Nesbitt and Zipser 2003; Barros et al. 2004; Mori et al. 2004; Hirose and Nakamura 2005; Houze et al. 2007; Cifelli et al. 2008; Hirose et al. 2008; Romatschke et al. 2010). Many of these studies focused on the time of the largest diurnal peak (e.g., Hirose et al. 2008; Cifelli et al. 2008) or used large regions to resolve the detailed structure of the diurnal cycle (e.g., Nesbitt and Zipser 2003; Romatschke et al. 2010). Although in the present study we also focus on the time of the largest diurnal peak, we highlight the diurnal variation of the heavy precipitation occurrence, which is important to analyze the extreme rainfall events.

1.5 Purposes and contents of the thesis

The purpose of the present study is to describe the temporal modulation of heavy precipitation over West Java and related three-dimensional structures due to cross-equatorial monsoon surges around Southeast Asia on the time scales from less than one day to two months in January–February 2007. We investigate the interaction of synoptic-scale disturbances — a cold surge, a cross-equatorial monsoon flow, and a Borneo vortex — and their impact on precipitation over West Java. This interaction includes the vertical structure of these disturbances. In contrast with the aforementioned examples of numerical studies, we do not attempt to reproduce a heavy rainfall event quantitatively. This work aims to study the heavy rainfall event associated with mesoscale convective systems, which include random processes in space and time, by utilizing probabilistic information. In this study, we also demonstrate the usefulness of cumulative distribution functions (CDFs) as a method of statistical analysis of heavy precipitation.

After performing the simulations for the two-month period, we want to focus in the shorter period in order to obtain further understanding of heavy precipitation during the Jakarta flood event. We also investigate the reproducibility of the heavy precipitation

in the model with different horizontal resolutions. This purpose includes further understanding of the statistical nature of the precipitation.

In Chapter 2, we describe the data and methodology used in this thesis. In Chapter 3, we present an investigation of the temporal modulation of three-dimensional synoptic fields and precipitation in the periods before, during, and after the heavy precipitation in Jakarta in 2007. The features of interest of the synoptic field are the cold surge, the cross-equatorial flow near the surface, and the appearance of the Borneo vortex. We also present the investigation of the statistical modulation of precipitation. We present further investigation on the heavy precipitation during the Jakarta flood event in February 2007 by performing numerical downscaling simulations with horizontal resolution of 2, 4, 5, and 20 km in Chapter 4. CDFs of precipitation rate for different regions and diurnal variations of statistical values are also investigated. In Chapter 5, we discuss the findings of the present study, and present our conclusions in Chapter 6.

Chapter 2

Data and Methodology

2.1 Data

In this section, we describe the data used in the present study. We use precipitation, infrared radiation, sea surface wind, the National Centers for Environmental Prediction (NCEP) Global Tropospheric Analyses (final analyses), and MJO phase data. The detailed description of each set of data follows below.

Precipitation

In the present study, we use hourly precipitation data from eight observational stations in Jakarta and its vicinity — Jakarta Observation Station, Manggarai, Pondok Betung, Sawangan, Cibinong, Darmaga Bogor, Cilember, and Citeko. See Fig. 1.1c for the locations of these stations. The data were obtained from the Meteorology, Climatology, and Geophysics Agency of Indonesia (BMKG). The temporal coverage of the data used is from 0000 UTC 31 January to 2300 UTC 4 February 2007.

We also use precipitation data from the TRMM 3B42 (Huffman et al. 2007), which include estimated rainfall for $0.25^\circ \times 0.25^\circ$ grid boxes at 3 hours intervals. The data is avail-

able from January 1998 to the present. The spatial coverage of the data is 50.0°N–50.0°S, 0.0°–357.5°E. The 3B42 estimates are produced in four stages: (1) 2A-12, Special Sensor Microwave Imager (SSM/I), Advanced Microwave Scanning Radiometer (AMSR), and Advanced Microwave Sounding Unit (AMSU), which are microwave estimates of precipitation, (referred to as "high quality (HQ)") are inter-calibrated (to 2B31) and combined, (2) infrared precipitation estimates are created using the calibrated HQ, (3) the HQ and IR estimates are combined, and (4) rescaled to monthly data. Each precipitation field is best interpreted as the precipitation rate effective at the nominal observation time. Data were downloaded from `ftp://disc2.nascom.nasa.gov/ftp/data/s4pa/TRMM_L3/TRMM_3B42`.

Infrared radiation

We use the Multi-functional Transport Satellite Infrared Channel 1 (MTSAT IR1) data, which is a measurement in the wavelength range of 10.3–11.3 μm (JMA cited 2011). The temporal coverage of the data is from June 1995 to present, with an interval of 1 hour. The spatial coverage of the data is 70°N–20°S, 70°–160°E with a horizontal resolution of $0.05° \times 0.05°$ or 1800×1800 pixels. The data is in a Portable Gray Map (PGM) format, which requires a calibration table to convert the pixel values into brightness temperature. The conversion result is the cloud-top temperature in units of K. We have obtained the data from `http://weather.is.kochi-u.ac.jp/`.

We also use daily-averaged outgoing longwave radiation (OLR) from the National Oceanic and Atmospheric Administration (NOAA) from a series of polar-orbiting satellites (Liebmann and Smith 1996). The data are continuous in time (after some interpolation for missing data) from June 1974 to 16 March 1978, and from 1 January 1979 to the present. The data cover the area of 90.0°N–90.0°S, 0.0°–357.5°E with a horizontal resolution of $2.5° \times 2.5°$ latitude–longitude grid. Interpolated OLR data are provided by the NOAA/OAR/ESRL PSD, Boulder, Colorado, USA, on their Web site at `http://www.esrl.noaa.gov/psd/`.

Sea surface wind

We also use the daily sea surface wind from the Quick Scatterometer (QuikSCAT) L3 product, which provides gridded winds at 10 m above the sea surface with a spatial resolution of $0.25° \times 0.25°$ distributed by National Aeronautics and Space Administration (e.g., Freilich and Dunbar 1999; Chelton and Freilich 2005). The data is available from June 1999 to November 2009. The spatial coverage of the data is 90.0°N–90.0°S, 0.0°–357.5°E. Gridded wind vector fields are provided twice daily according to the timing of the ascending and descending satellite swath coverage; where multiple swaths from a particular ascending or descending sample period intersect a given point, the data from the most recent swath coverage over-writes the data from the earlier (adjacent) swath. Quality flags are provided for each wind vector cell to assist in identifying potential rain contamination and whether the data from both inner and outer beams are available. The wind vectors are null (set to missing values) when within 30 km of land–ice boundaries or where there are no wind vector retrievals available. Gridded wind vector fields are processed directly from the QuikSCAT Level 2B swath data, which use the QSCAT-1 geophysical model function. No additional processing is performed on the wind vector data. We downloaded the data from `http://podaac.jpl.nasa.gov/dataset/QSCAT_LEVEL_3`

NCEP final analyses

We use NCEP final analyses (FNL), which are on $1.0° \times 1.0°$ grids prepared operationally every 6 hours (see online at `http://dss.ucar.edu/datasets/ds083.2/`). The NCEP FNL is available from 1800 UTC 30 July 1999 to 1800 UTC 6 November 2011. The spatial coverage of the data is 90°N–90°S, 0°–360°E. The analyses are available on the surface, at 26 mandatory (and other pressure) levels from 1000 to 10 hPa, in the surface boundary layer and at some sigma layers, the tropopause and a few others. The parameters include surface pressure, sea level pressure, geopotential height, temperature, sea surface temperature, soil values, ice cover, relative humidity, u- and v-winds, vertical motion, vorticity, and ozone. This product is from the Global Data Assimilation System

(GDAS), which continuously collects observational data from the Global Telecommunications System (GTS) and other sources, for various analyses. The FNLs are made with the same model as the one used by NCEP in the Global Forecast System (GFS), but the FNLs are prepared about an hour or so after the GFS is initialized. The FNLs are delayed so that more observational data can be used. The GFS is run earlier in support of time critical forecast needs, and uses the FNL from the previous 6 hours cycle as part of its initialization. The data were downloaded from the Research Data Archive (RDA), which is maintained by the Computational and Information Systems Laboratory (CISL) at the NCAR. The original data are available from the RDA Web site (`http://dss.ucar.edu`) in dataset number ds083.2.

MJO Index

Wheeler and Hendon (2004) computed MJO index based on the first two Empirical Orthogonal Functions (EOFs) of the combined fields of near-equatorially-averaged 850-hPa zonal wind, 200-hPa zonal wind, and satellite-observed OLR data. Projection of the daily observed data onto such multiple-variable EOFs, with the annual cycle and components of interannual variability removed, yields principal component (PC) time series that vary mostly on the intraseasonal time scale of the MJO only. This projection thus serves as an effective filter for the MJO without the need for time filtering, making the PC time series an effective index for real time use. The two PC time series that form the index are called as the Real-time Multivariate MJO series 1 and 2 (RMM1 and RMM2). For the input data of the MJO index, they use the OLR data that measured by the NOAA polar-orbitting satellites, while for the winds they use the NCEP/NCAR Reanalyses and the NCEP Operational analyses. The index is usually available in near real time about 12 hours after the end of each Greenwich day (i.e. at about 1200 UTC). The index is available for public from the following Web site: `http://www.cawcr.gov.au/staff/mwheeler/maproom/RMM/index.htm`.

2.2 Methodology

2.2.1 Brief description of the numerical model

In the present study, we use Japan Meteorological Agency Nonhydrostatic Model (JMA-NHM; Saito et al. 2006, 2007). The JMA-NHM is a community model for both operational forecasting and atmospheric research. The original root is a nonhydrostatic model developed at the Forecast Research Department of the Meteorological Research Institute (MRI; Ikawa and Saito 1991). Their model was initially developed as a research tool, and then modified to a nesting model (Saito 1994) to simulate mesoscale phenomena realistically. In 1999, a cooperative effort to develop a community model for numerical weather prediction (NWP) and research started between the Numerical Prediction Division (NPD) of JMA and MRI. A unified model, MRI/NPD-NHM, was completed in 2000, and a comprehensive description was published as a technical report from MRI (Saito et al. 2001a). In the later development of the model, several modifications have been made to enhance computational efficiency, robustness, and accuracy to create an operational NWP model with a horizontal resolution of 10 km.

Basic equations of the JMA-NHM are fully compressible with a map factor, on the terrain-following vertical coordinate (Saito et al. 2006). For the Southern Hemisphere, the model only supports the Mercator projection, whereas Lambert conformal and Polar stereo projections are available for the Northern Hemisphere in addition to the Mercator. The model grid structure is the Arakawa C type in the horizontal direction and the Lorenz type in the vertical direction. The fourth-order scheme with advection correction and time splitting is chosen for the horizontal advection, considering the computational cost and matching with the advection correction scheme. The model implements a split explicit scheme [horizontally explicit-vertically implicit (HE-VI)], in light of the computational efficiency in the parallel computing architecture.

For cloud microphysics, the model employs a bulk-type scheme with an ice phase (Lin et al. 1983), which includes a box-Lagrangian particle fall scheme. The box-Lagrangian

scheme (Kato 1995) is applied not only to computation of fallout of rain, but also to graupel to keep computational stability. One of the bulk-type schemes employed by NHM is 6-class bulk microphysics scheme.

Cumulus parameterization is one of the key issues in determining model performance in NWP models and general circulation model (GCM). NHM employs the Kain–Fritsch scheme that was revised by Ohmori and Yamada (2004) in addition to the modifications described in Kain (2004) to improve its performance with a 10-km resolution for prediction of heavy rainfall events in Japan, where a moist and unstable maritime air mass prevails in the summer. In addition to the modified Kain–Fritsch scheme, JMA-NHM is equipped with the Grell, the Arakawa–Schubert, and the moist convective adjustment scheme, among which the latter two schemes were originally developed for GCMs, under the assumption that the horizontal grid space is much larger than the cloud scale.

For radiation processes, NHM employs the Global Spectral Model 0412 (GSM0412) scheme. In this scheme, cloud and clear sky radiation follow the Kitagawa (2000) and Yabu et al. (2005) schemes, respectively. Optional choices are the GSM0103 and the atmospheric radiation scheme based on Sugi et al. (1990).

For planetary boundary layer (PBL) processes, NHM employs an improved Mellor–Yamada level 3 scheme (Nakanishi and Niino 2004, 2006). JMA-NHM also supports Mellor–Yamada level 2 and improved Mellor–Yamada level 2.5 as an alternative for PBL parameterization scheme.

For land surface processes, NHM employs a prognostic scheme with 4-layer soil temperature. The values of scalar roughness lengths for heat and moisture were reduced to about 1/7.4 of the momentum roughness length, following Garratt and Francey (1978). Furthermore, the computation of bulk coefficients for surface fluxes over land follows Louis et al. (1982). For sea surface temperature (SST), NHM can take the data from initial and boundary conditions. The SST data is linearly interpolated in space into the grids of the NHM at each model time step.

2.2.2 Specification of JMA-NHM for 20 km experiments

In Chapters 3 and 4, we set up the same computational domain with a 20-km horizontal resolution. The domain has 103 × 115 grid points centered at 5°S, 110°E and covers about 14°S–4°N, 100°–120°E on a Mercator projection. Figure 2.1 shows the computational domain and surface elevation of the 20 km experiments, which covers an area of 2060 km × 2300 km. In this figure, we can see three main islands in Indonesia from the largest to the smallest, namely Borneo (Kalimantan), Sumatra, and Java. Borneo, which is the third largest island in the world, has a high elevation mostly in the northern part of the island. Sumatra, which measures approximately 1500 km by 400 km, has a significant mountain range along its southwestern coastline, with an average height of 2000 m. Java, which is the region of interest, is zonally elongated, and slightly tilted in the northwest–southeast direction, with a central mountain range that runs the length of the island. The central mountain range comprises a series of quasi-circular small volcanoes, except over West Java where the mountains are more continuously connected. In general, the central mountain range is closer to the south coast than to the northern one, except over Central Java.

As for the vertical discretization of the NHM, we use 40 levels with variable grid intervals of $\Delta z = 40$ to 1180 m are employed. The model top and the lowest level are located at 22100 and 20 m above the ground, respectively.

Initial conditions of horizontal wind, temperature, water vapor, and surface pressure are given by the NCEP FNL. Lateral boundary conditions are also supplies by the NCEP FNL. NCEP FNL provide the SST data for the model.

The subgrid-scale parameterization schemes and parameter settings that we employed are basically the same as those of Hayashi et al. (2008) with their recommended values tuned for the 20-km horizontal resolution. The cloud microphysics scheme is a 6-class bulk microphysics. The cumulus parameterization scheme is a modified Kain–Fritsch. The GSM0412 radiation scheme (Kitagawa 2000; Yabu et al. 2005) and an improved Mellor–Yamada Level 3 planetary boundary layer scheme (Nakanishi and Niino 2004,

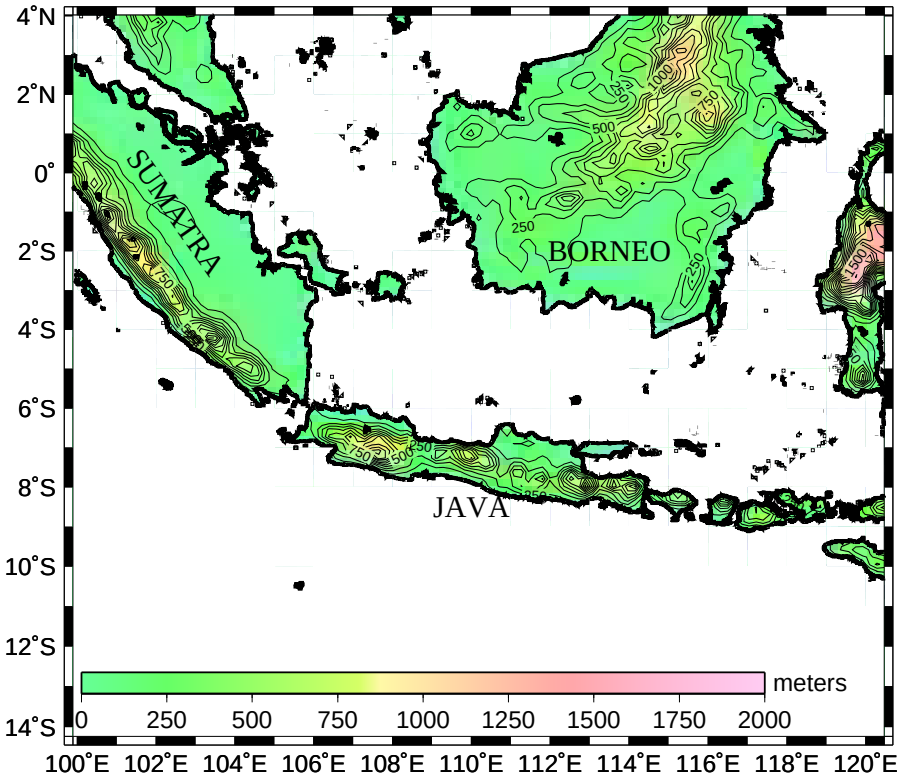

Figure 2.1: The model domain for computation of a 20-km resolution. Shading and contours show topography (m) of the domain.

2006) are used.

A summary of the specifications of JMA-NHM with a 20-km horizontal resolution used in Chapters 3 and 4 is given in the Table 2.1. The specific parameter settings and configurations of the model for 2-, 4-, and 5-km resolutions are described in Chapter 4.

2.2.3 Time-lagged ensemble technique

In order to use information present in past observations and simultaneously to take advantage of the benefits of stochastic dynamic prediction, Hoffman and Kalnay (1983) proposed a new ensemble forecast method which they called the "lagged average forecast (LAF) method." They tested the LAF method with a highly simplified atmospheric model, which was a two-layer low order spectral model on a doubly periodic f-plane forced by asymmetric Newtonian heating of the lower layer. The LAF method provided

Table 2.1: Specifications of JMA-NHM with a 20-km horizontal resolution used in the present study.

Category	Specification
Horizontal mesh (resolution)	103×115 (20 km)
Mapping	Mercator
Levels	40 terrain-following
Model top	22100 m
Horizontal discretization	Arakawa C
Horizontal advection	Flux form 4th order with advection correction and time splitting
Gravity waves	Time splitting
Sound waves	HE-VI
Forecast period	72 hours
Initial time	00, 06, 12, or 18 UTC
Initial conditions	NCEP-FNL
Prognostic variables	$U, V, W, P, \theta, q_v, q_c, q_i, q_r, q_s, q_g, TKE, \theta_l'^2, q_w'^2, \theta_l' q_w'$
Cloud microphysics	6-class bulk microphysics
Cumulus parameterization	Kain–Fritsch scheme
Radiation	GSM0412 scheme
Planetary boundary layer	Improved Mellor–Yamada Lv. 3
Soil temperature	Prognostic scheme with 4-layer soil temperature
Lateral boundary	Rayleigh damping

a priori estimates of forecast skill, because there was a strong correlation between the dispersion of the ensemble members and the loss of predictability.

Branković et al. (1990) applied the LAF method to the T63 version of the European Centre for Medium Range Weather Forecasts (ECMWF) operational spectral global model and introduced the terminology of time-lagged ensemble forecast to the LAF method. Their results showed that in practice, about a third of the ensemble-mean forecasts, at forecast days 11–20, were more skillful than both persistence and climate, and, in addition, were more skillful than the latest member of the ensemble.

In a more recent study by Mittermaier (2007), time-lagged ensembles were used as a means of testing temporal evolution and general behavioral aspects of a high-resolution operational model, and establishing whether the identified behavior could somehow be exploited to improve forecast skill. The operational model used in that study was the

Met Office Unified Model with a 4-km horizontal resolution, which runs every 6 hours to $t + 36$ hours. The study established that the time-lagged ensembles had sufficient skill at the grid scale to suggest that the method was at least equivalent to, and possibly superior to, spatial upscaling of an individual forecast, because more of the skillful (potentially high-impact) grid-scale detail could be retained.

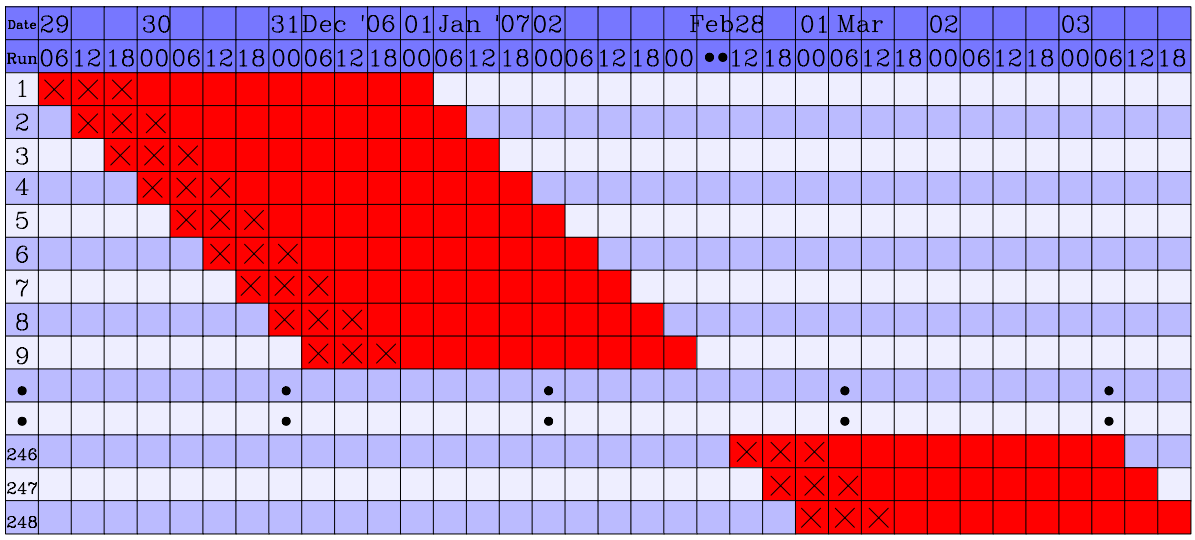

Figure 2.2: Schematic diagram of the time-lagged ensemble simulations. See text for details.

In the present study, we employed the time-lagged ensemble technique for hindcast experiments. To run the time-lagged ensemble simulation, we followed the procedure and method used by Mittermaier (2007), except for the length of individual simulation (72 hours instead of 36 hours). The time-lagged ensemble is created from a series of successive simulations. The initial conditions, although not perturbed, are generated from different initializations, which represent the atmospheric state in a flow-dependent and time-evolving manner.

Figure 2.2 gives an illustration of the time-lagged ensemble simulations. The first and second rows denote the date and hour of simulations, respectively. Each box with a label "00", "06", "12", or "18" represents 6 hours of data; for example, the label "00" means the data for 00–05 hours. The third to bottom row denotes the number of the run (there are 248 runs in this case). We perform 72-hour simulations for each run. The simulation

is performed every 6 hours with the initial time of 00, 06, 12, and 18 UTC. We exclude the initial 18 hours, denoted by "×", from analyses to avoid the effect of unrealistic convections in the spinup processes. By employing this scheme, a nine-member ensemble can be created for a 6-hour window.

In these analyses, the ensemble mean is computed as a simple arithmetic average from all members. There is no weighting of individual simulation results. The model output is sampled every 1 hour.

Figure 2.3 shows examples of time series of model-simulated precipitation rate of 20-km horizontal resolution. The top time series is initialized at 1900 LT 1 February 2007. The time series is an area average over the land region of West Java (5.5°–8°S, 105.5°–108.5 °E). This figure shows the dependence of precipitation on the local time of the initial conditions. Four colors show four different local times. The diurnal cycle is reproduced, where the precipitation peak occurs in the early morning. For the initial local time of 13 and 19 LT, the precipitation tends to reach its peak early soon after the initial condition. However, for the initial local time of 01 LT and 07 LT, the precipitation reaches its peak slowly.

Figure 2.4 shows composite time series of model-simulated precipitation rate of 20-km horizontal resolution averaged over the land region of West Java. Each line shows the composite time series of precipitation as a function of forecast time. Black line show the composite starting at 07 LT, red — starting at 13 LT, green — at 19 LT, and blue — at 01 LT. All the runs for the two-month period are used for the composites. This figure shows the large dependency of precipitation rate for different local times of initial conditions (07, 13, 19, and 01 LT) in the evolution of the diurnal cycle for the first 18 hours. For example, on the one hand, the time series of the precipitation rate for the initial time of 13 LT shows a fast increase of precipitation as a function of forecast time. On the other hand, the time series of the initial time of 01 LT exhibits a slow increase of precipitation. This fact shows the existence of spinup processes. Even after the first 18 hours, a local time dependence of the choice of initial time is still exist. The figure shows large variation of precipitation intensity in its peak time.

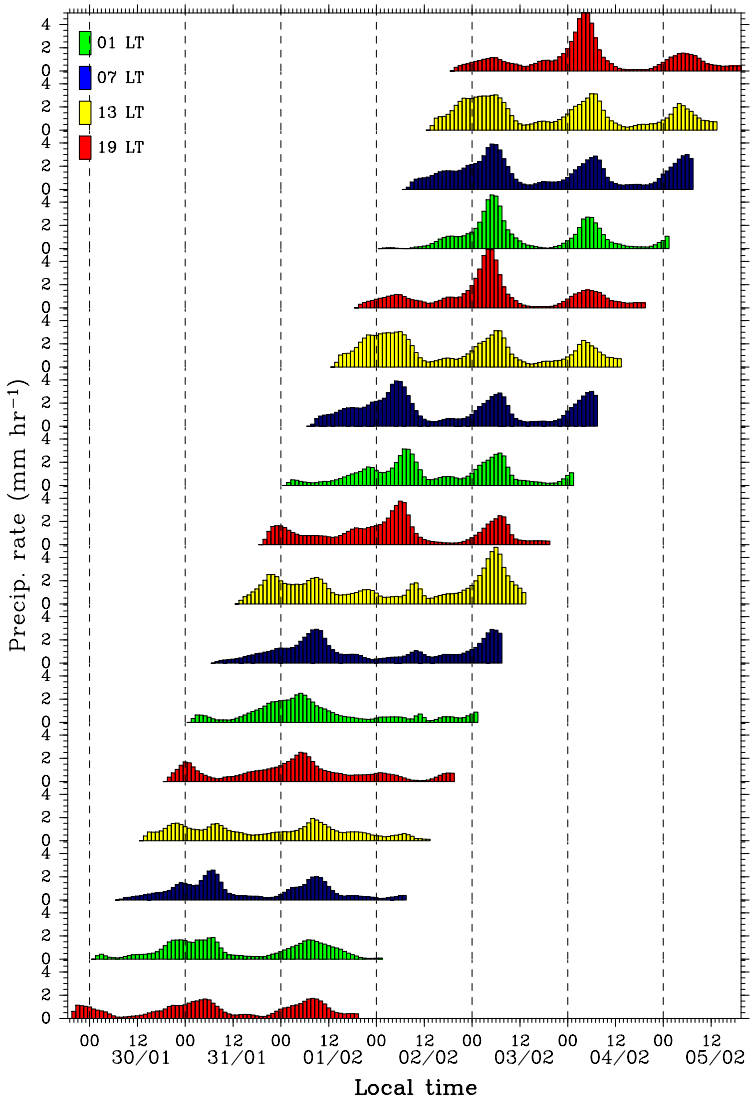

Figure 2.3: Time series of model-simulated precipitation rate of 20-km horizontal resolution averaged over the land region of West Java (5.5°–8°S, 105.5°–108.5°E). The bottom series is initialized at 1200 UTC 29 January 2007, and the top one at 1200 UTC 1 February 2007.

The fact that the spinup processes exist implies that ensemble simulations in the tropics may have biases on the diurnal precipitation cycle, if all the ensemble members start from a single local time. By employing the time-lagged ensemble technique, we can avoid such a diurnal cycle problem in ensemble simulations. This is one of the advantages of employing this method. Based on Fig. 2.4, we discard the first 18 hours in the analyses. Because some differences remain after 18 hours, we combine model runs with different local time of initial conditions to remove this bias.

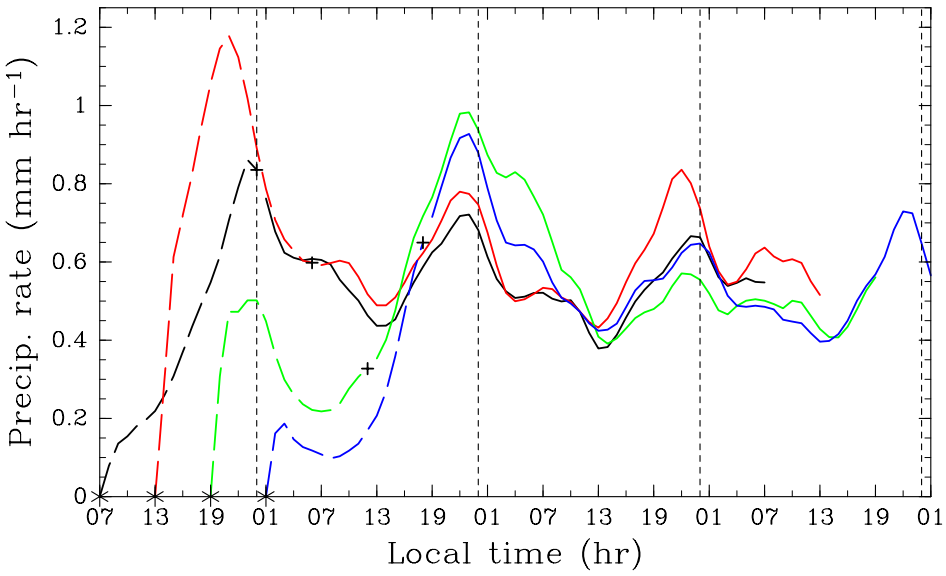

Figure 2.4: Composite time series of model-simulated precipitation of 20-km horizontal resolution as a function of forecast time. The series is composite over 2-month period and averaged over the land region of West Java. Black, red, green, and blue lines show the composites starting at 07, 13, 19, and 01 LT, respectively. The vertical dashed lines denote local midnight. See text for details.

Chapter 3

Modulation of precipitation in January–February 2007

3.1 Introduction

Natural disasters related to severe weather events (e.g., flood and landslide caused by heavy rainfall) often occur in Indonesia and have great impacts on human life. One example is the Jakarta flood event in February 2007, which was a devastating disaster and is considered the worst in the last three decades; 48 people were killed, 521 389 people were evacuated, and 24 957 houses were damaged, as shown in Table 1.1. As we review in Chapter 1, the disaster occurred mainly because of heavy rainfall for several times from 31 January to 2 February. Wu et al. (2007) showed that the heavy rainfall coincided with a strong and persistent cross-equatorial monsoon flow from the Northern Hemisphere, as shown in Fig. 1.4.

As stated in Section 1.2, heavy precipitation in Southeast Asia is closely related to synoptic disturbances such as cold surge and Borneo vortex. Although statistical analyses on the relationship have been conducted by previous studies, detailed case studies are limited. Moreover, only a few of numerical studies addressed extreme precipitation events

related to the monsoon in tropical Asia.

In this chapter, an ensemble simulation is performed with a relatively coarse-resolution model with cumulus parameterizations, event though heavy precipitation induced by local topography might be underestimated. Because mesoscale convective systems include random processes in space and time, probabilistic information would be useful to study heavy precipitation events associated with them. Furthermore, ensemble numerical weather prediction with a global model became a standard technique to obtain probabilistic information in the 1990s at operational weather forecast centers, while that with a regional mesoscale model is still an interesting and greatly challenging subject (e.g., Yoden 2007).

In the tropics, precipitation has large amplitudes in its diurnal cycle, which highly depends on geographical location and local time (e.g., Mori et al. 2004; Hirose and Nakamura 2005). Because of the existence of spinup processes, ensemble simulations in the tropics may have biases on local precipitation if all the ensemble members are started from one initial time in a day as shown by Fig. 2.4. To avoid such a diurnal cycle problem in ensemble simulations, a time-lagged ensemble technique as described in Section 2.2.2 is used in this study. A regional model that consists of a single domain with a relatively coarse resolution is used to perform ensemble simulations for the two-month period including the Jakarta flood event.

Based on the ensemble simulation data, we investigate the temporal modulation of three-dimensional synoptic fields and precipitation in the periods before, during, and after the heavy rainfall in Jakarta in 2007. Key features of the synoptic field are cold surge, cross-equatorial flow near the surface, and the appearance of the Borneo vortex. We also investigate frequency distribution functions in pentad time scales to characterize the statistical feature of heavy rainfall. This chapter is organized as follows. Section 3.2 explains the experimental design. Section 3.3 presents the results of the analysis of the ensemble simulation data. Section 3.4 provides a discussion and conclusions are drawn in section 3.5.

3.2 Experimental design

The numerical model used in this study is the Japan Meteorological Agency Non-hydrostatic Model (JMA-NHM; Saito et al. 2006, 2007) as described in Chapter 2. The subgrid-scale parameterization schemes used in this chapter are summarized in Table 2.1. To run the time-lagged ensemble simulation, we follow the same procedure and method used by Mittermaier (2007), but for the length of individual simulation (see Fig. 2.2 for the schematic diagram of the time-lagged ensemble simulation).

To validate the numerical results, we use the TRMM 3B42 product (Huffman et al. 2007). The TRMM data show the correlation coefficient of 0.56 with the rain gauge data at Soekarno-Hatta near Jakarta for the 2-month period. We also use the daily sea surface wind of the NASA QuikSCAT L3 product to validate the model-simulated surface winds.

3.3 Results

3.3.1 Comparison of precipitation between the TRMM data and the model output

Figure 3.2 shows the time series of the TRMM estimated rainfall (Fig. 3.2a), the superimposed time series of the model-simulated precipitation rate of the 9 ensemble members (Fig. 3.2b), and the time series of the ensemble mean (Fig. 3.2c) in mm hr^{-1} at the nearest grid point to the Pondok Betung Station for the two-month period. The location of Pondok Betung is denoted by the open circle in the inset map of Fig. 3.1. The characteristic time scale of precipitation is generally small (less than 1 day) suggesting a convective origin, as shown by the TRMM data (Fig. 3.2a). The model-simulated precipitation (Fig. 3.2b) shows a similar time scale, which is determined by that of mesoscale convective systems. Some ensemble members show heavy precipitation (> 10 mm hr^{-1}) during or just after the period of the Jakarta flood event. Such enhancement of precipitation is also discernible in the ensemble average (Fig. 3.2c), although the magnitude is

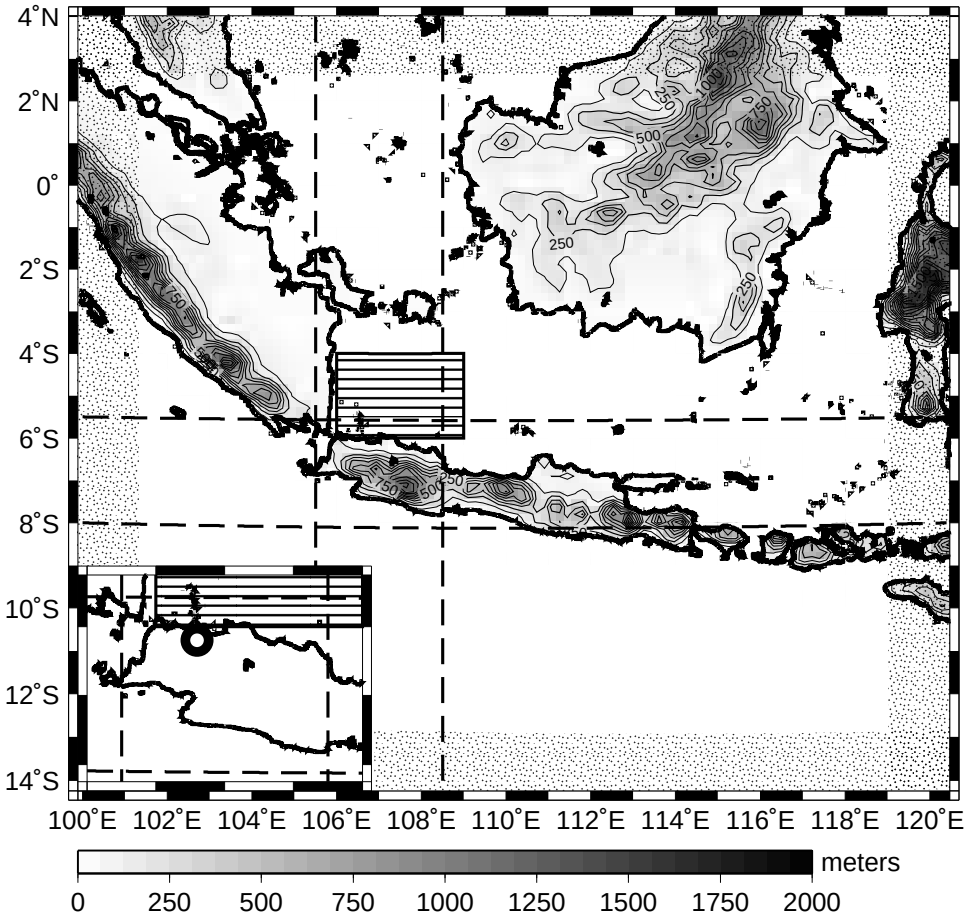

Figure 3.1: The model domain of computation. Shading and contours show topography (m) of the domain. The two horizontal dashed lines denote the latitudes of 5.5°and 8°S. The zonal belt is used for cross-section analyses in Fig. 3.3. The two vertical dashed lines denote the longitudes of 105.5°and 108.5°E. The meridional belt is used for cross-section analyses in Figs. 3.4, 3.5, and 3.9. The dotted region near the side boundaries is not used in the analyses. The box with a horizontal hatch pattern that covers the area between 4°–6°S and 106°–109°E is used for Fig. 3.14. The inset map shows West Java. The circle in the inset map denotes the location of Pondok Betung Station. The hatched area in the inset map is used for Figs. 3.13 and 3.14.

much smaller. Both the TRMM data and the model results show modulation of precipitation rate in the two-month period. There is little rainfall observed during the first half of January, whereas rainfall occurs frequently afterward.

Figure 3.3 shows the time–longitude cross sections of the TRMM estimated rainfall data (Fig. 3.3a) and the ensemble mean of the model-simulated precipitation rate (Fig. 3.3b) averaged between 5.5°and 8°S (denoted by the two horizontal dashed lines in Fig. 3.1). The vertical lines in Figs. 3.3a,b denote the longitude of 106.6°E, which is the

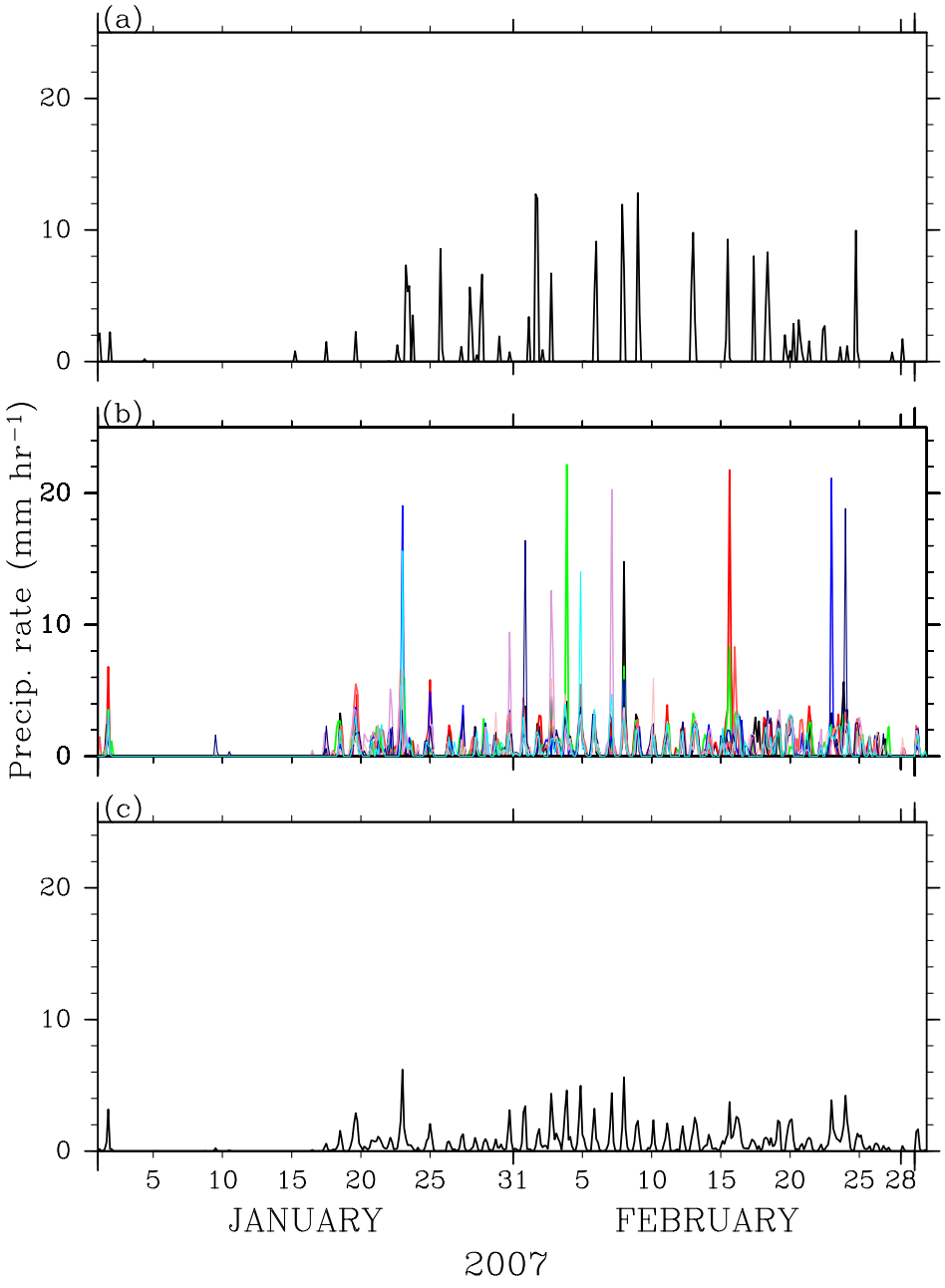

Figure 3.2: (a) Time series of the TRMM estimated rainfall, (b) superimposed time series of the model-simulated precipitation rate of the 9 ensemble members, and (c) time series of the ensemble mean in the unit of mm hr^{-1} at the nearest grid point to the Pondok Betung Station for the 2-month period from 0000 UTC 1 Jan to 2300 UTC 1 Mar 2007. The location of Pondok Betung Station is denoted by the open circle in the inset map of Fig. 3.1.

longitude of Pondok Betung Station. There is little rain in the first half of January in the plotted region in Fig. 3.3a. The dry region has a wider longitudinal extent from 60°E to

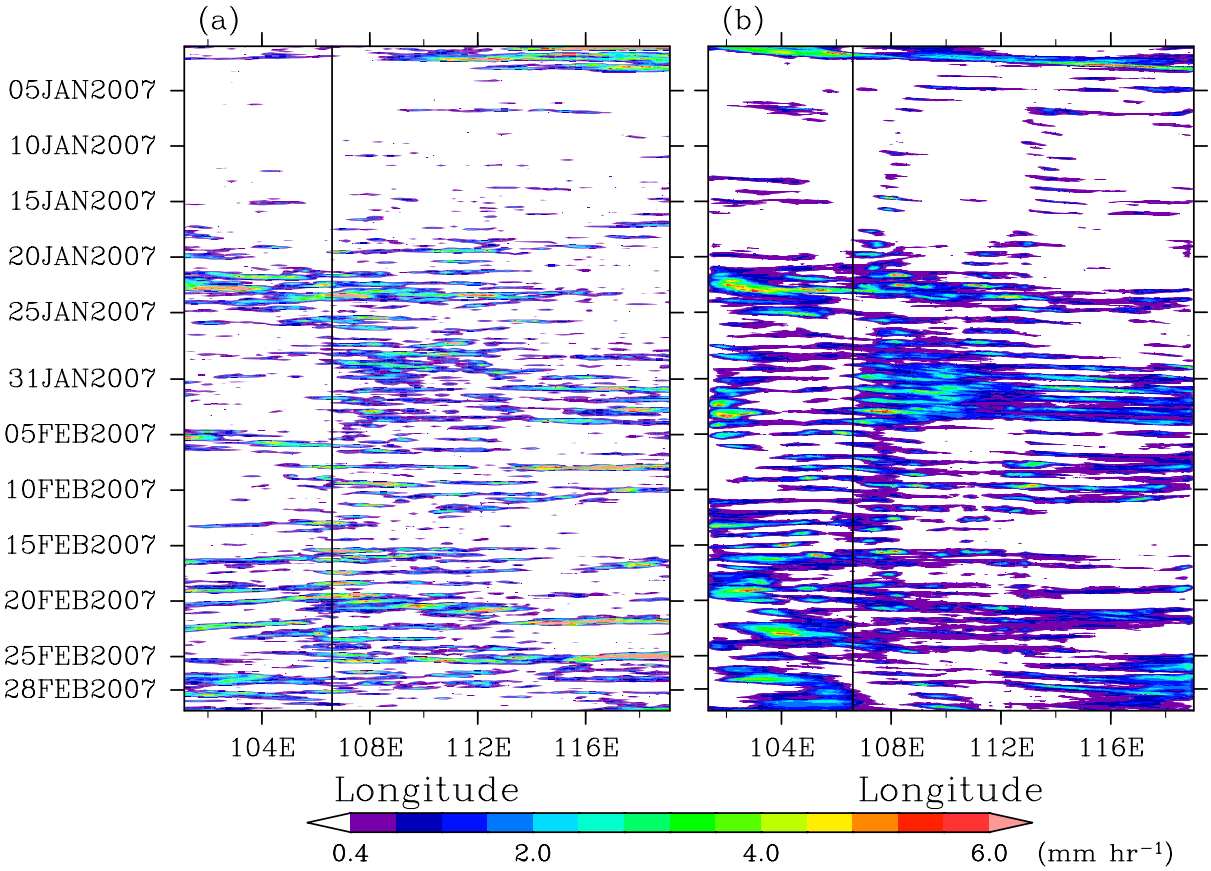

Figure 3.3: Time–longitude cross sections of (a) the TRMM data and (b) the ensemble mean of the model-simulated precipitation rate averaged between 5.5°and 8°S (denoted by two horizontal dashed lines in Fig. 3.1). The vertical lines in (a) and (b) denote the longitude of 106.6°E, which is the longitude of Pondok Betung Station.

140°E (see Appendix A). After 15 January or so, rainfall increases from the western part of the domain. An enhancement of precipitation between 106°and 113°E is observed in the period of the Jakarta flood event. During the period, Jakarta is at the west end of the enhanced precipitation region and an area to the west of Jakarta remains clear. About 1 week before the flood event, the precipitation region extends from the west end of the domain to 115°E in longitude, which is wider than that in the period of the flood event. In the first half of February, precipitation is relatively limited in the plotted domain, whereas in the second half of February, precipitation increases with large longitudinal extent. It should be noted that a signal of MJO is weak for the two-month period.

The ensemble mean of the model-simulated precipitation rates (Fig. 3.3b) shows a

good agreement with the TRMM data. The modulation of precipitation through the two-month period is well reproduced by the ensemble mean. A similar longitudinal extent of precipitation is captured in the period of the Jakarta flood event, although the model tends to show the increase of the area of weak precipitation (denoted with purple color). The model is also able to reproduce the wide area of dry condition in the first half of January and the modulation of longitudinal extent of precipitation in February.

Figure 3.4 shows the time–latitude cross sections of the TRMM estimated rainfall data (Fig. 3.4a) and the ensemble mean of the model-simulated precipitation rate (Fig. 3.4b) averaged between 105.5°and 108.5°E (denoted by the two vertical dashed lines in Fig. 3.1). The horizontal lines in Figs. 3.4a,b denote the latitude of 6.2°S, which is the latitude of Pondok Betung Station in the northern part of Java. The TRMM data (Fig. 3.4a) shows that in the first half of January, continual precipitation exists between 2°S and 5°S, whereas intermittent rainfall with an interval of about 1 week exists to the north of 2°S. There is little rain to the south of 5°S during the period. The meridional extent of heavy rainfall occurrence varies after around 17 January. Before the Jakarta flood event, a signal of heavy rainfall propagates from 2.5°N around 25 January to 6°S around 30 January. After the signal reaches the northern part of Java, it does not propagate any farther. The meridional extent of rainfall concentrates in the latitude between 5°S and 8°S from around 30 January to 15 February. Right after 15 February, it becomes larger with a higher rain rate to the south of 6°S.

The ensemble mean of the model-simulated precipitation rates (Fig. 3.4b) again resembles that of the TRMM data. The north–south contrast of precipitation before around 17 January is reproduced well in the model. The propagation of a signal of heavy rainfall just before the Jakarta flood event is also well reproduced. The meridional extent of precipitation is somewhat larger in the ensemble mean from 31 January to 8 February. The modulation of intermittent precipitation to the south of 6°S in the second half of February is also well reproduced.

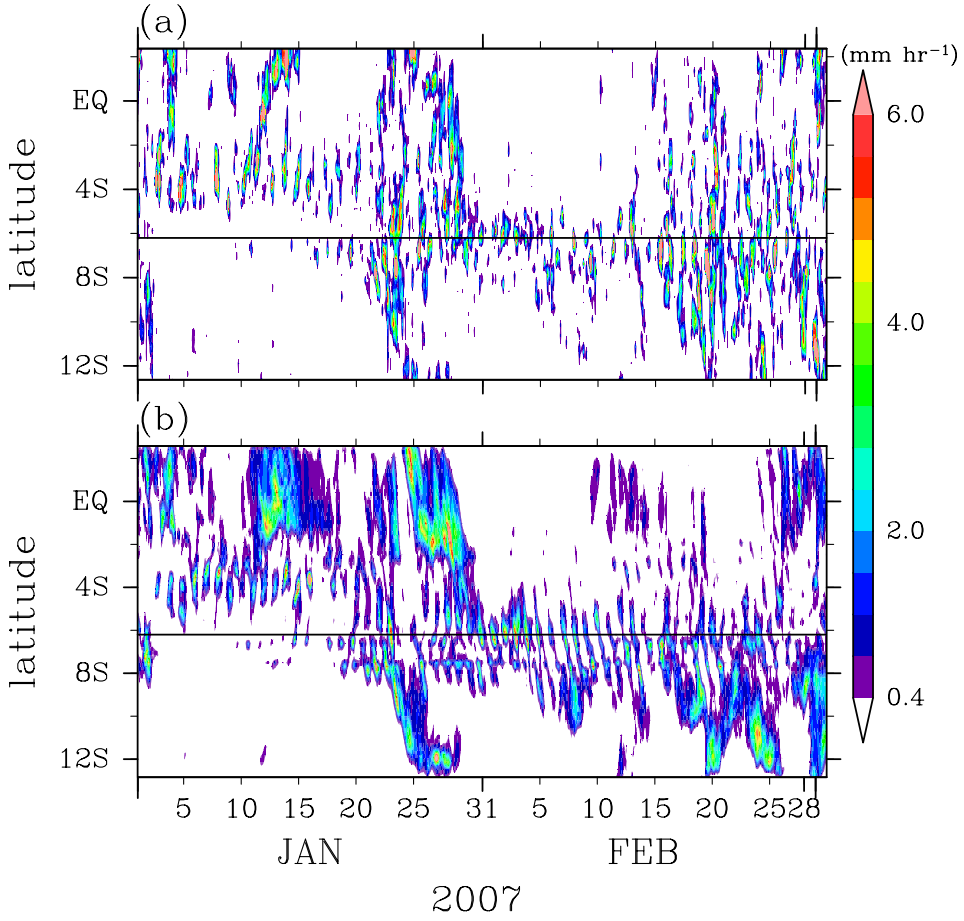

Figure 3.4: Time–latitude cross sections of (a) the TRMM data and (b) the ensemble mean of the model-simulated precipitation rate averaged between 105.5°E and 108.5°E (denoted by two vertical dashed lines in Fig. 3.1). The horizontal lines in (a) and (b) denote the latitude of 6.2°S which is the latitude of Pondok Betung Station.

3.3.2 Modulation of synoptic fields

We analyze three-dimensional synoptic fields that are considered to be associated with the modulation of precipitation in the two-month period, by using the ensemble mean of the three-dimensional JMA-NHM model output. Figure 3.5 shows the time–latitude cross sections of the ensemble mean of the model-simulated meridional wind anomaly (Fig. 3.5a, m s^{-1}), temperature anomaly (Fig. 3.5b, °C), relative humidity (Fig. 3.5c, %), and mixing ratio of water vapor (Fig. 3.5d, kg/kg) at 850-hPa averaged between 105.5° and 108.5°E, which are the same as those used in Fig. 3.4. Here, we define an anomaly as a deviation from the two-month average.

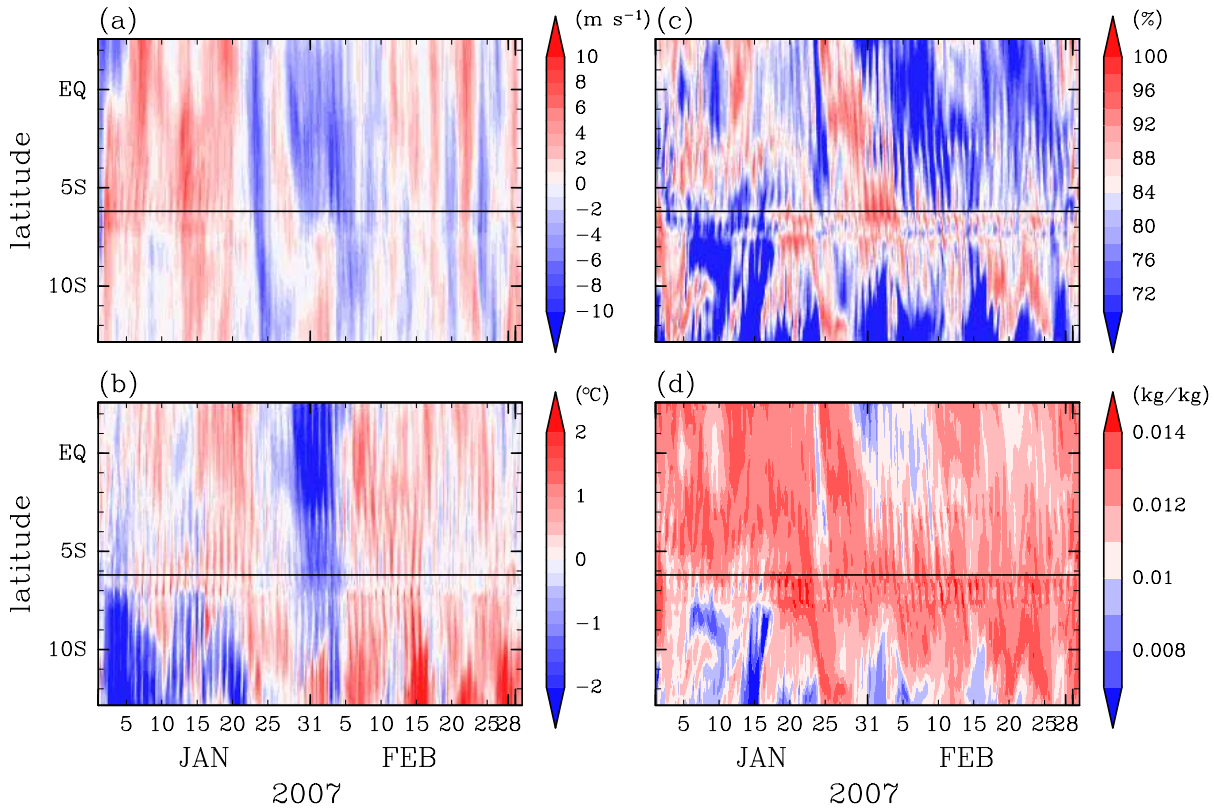

Figure 3.5: As in Fig. 3.4, but for the ensemble mean of the model-simulated (a) meridional wind anomaly (m s^{-1}), (b) temperature anomaly (°C), (c) relative humidity (%), and (d) mixing ratio of water vapor (kg/kg) at 850 hPa. We define an anomaly as a deviation from the two-month average.

Figure 3.5a shows that there is positive (northward) wind anomaly in most of the latitudes in the first 20 days of January. The propagation of a signal of negative anomaly of the meridional winds is evident from 2.5°N on 27 January to 6°S on 29 January, which corresponds to the propagation of a signal of precipitation in Fig. 3.4. The negative anomaly of meridional winds continues about one week at 6°S during and after the Jakarta flood event. Another event of the propagation of negative meridional wind anomaly is seen from 2.5°N on 22 January to 13°S on 24 January with some correspondence to the enhancement of precipitation shown in Fig. 3.4b.

A cold anomaly persists from 29 January to 4 February during and after the Jakarta flood event around 6°S (Fig. 3.5b). It is related to the propagation of cold anomaly, which is associated with the propagation of negative anomaly of meridional wind from 27 to 29

January, as described above. The association of the cold anomaly with the northerly anomaly is indicative of a cold surge event. Continuation of the cold surge reaches 12°S on 29 January and the south end of the computational domain on 3 February. Note that there is no evidence of the cold anomaly around 22 January that corresponds to the strong negative meridional wind anomaly. This is a surge event, but not a cold surge event. Larger variability of temperature anomaly exists to the south of Java for the two-month period, in which cold (warm) anomaly dominates during January (February).

Time–latitude variations of relative humidity (Fig. 3.5c) shows similar pattern with those of the precipitation shown in Fig. 3.4b. The period of late January to early February is also marked by a moist condition near the surface (at 850 hPa) with value of relative humidity exceeding 96% over the northern part of Java. Along the horizontal line in Fig. 3.5 that shows the latitude of Jakarta, the temperature anomaly and relative humidity show anticorrelation, which indicates that the high humidity over Jakarta during this period is due to low temperature. Mixing ratio of water vapor along the horizontal line during the period is not much reduce compared to other periods (Fig. 3.5d). However, the plot of mixing ratio shows the airmass transformation of the cold surge that is associated with the Jakarta flood event. The air mass is dry in the Northern Hemisphere, but it gets moistened over the ocean, which is consistent with the description by Johnson and Houze (1987).

To see the vertical extents of the time variations described above, the time–height cross sections of the ensemble mean of the model-simulated quantities averaged over the region of West Java (5.5°–8°S, 105.5°–108.5°E) are shown in Fig. 3.6 for meridional wind anomaly (Fig. 3.6a), temperature anomaly (Fig. 3.6b), and relative humidity (Fig. 3.6c). The negative meridional wind anomaly is seen below 800 hPa from 29 January to 10 February, whereas the positive anomaly above that exists until 3 February, which constitutes the low-level vertical shear of winds as pointed out by Wu et al. (2007). During the cold anomaly period after the reach of the cold surge (29 January–4 February), the top of the cold anomaly varies from 700 to 500 hPa over West Java, whereas the top of the moist layer in which the value of relative humidity exceeds 85% varies from 600 to 800

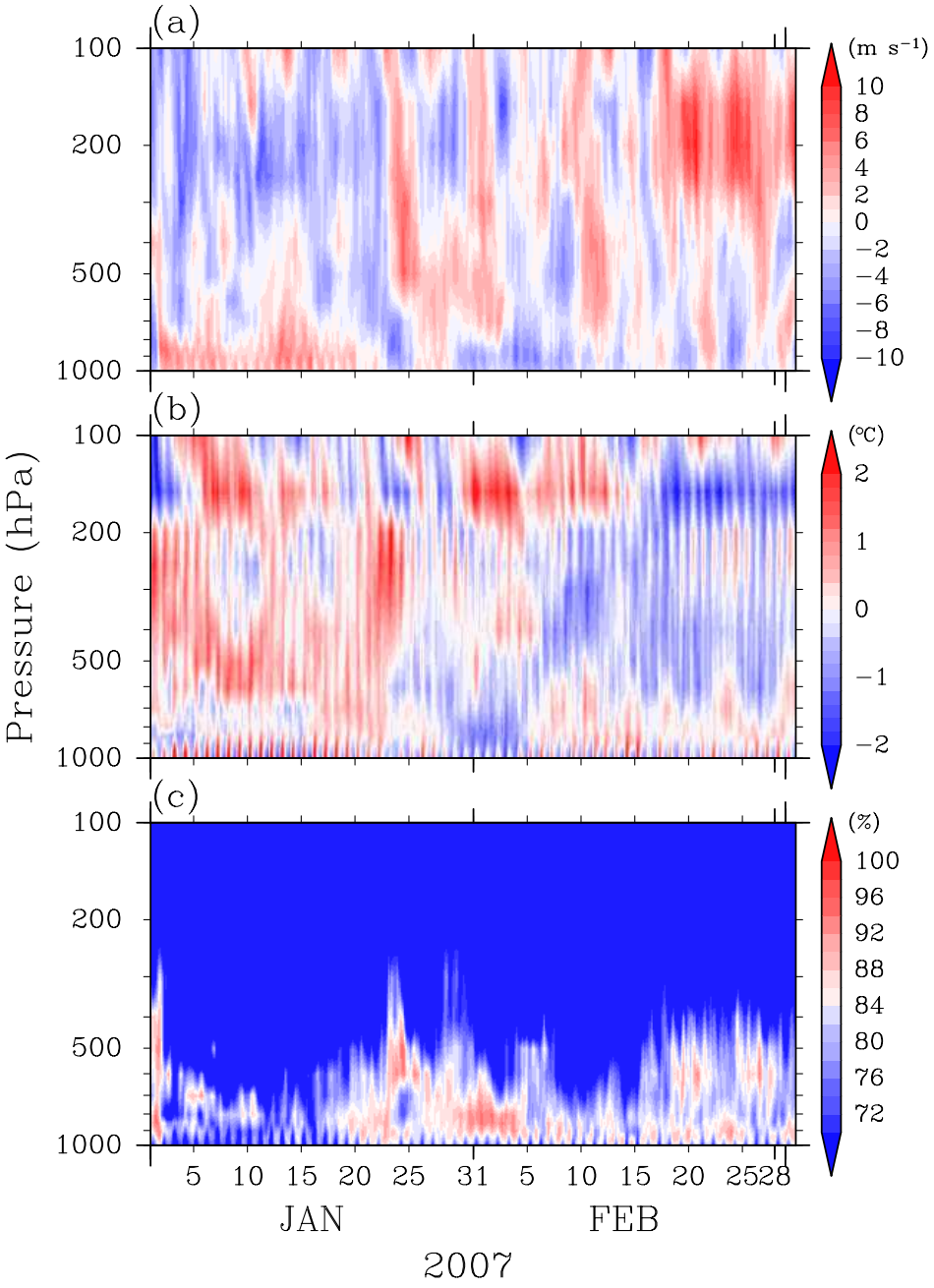

Figure 3.6: Time–height cross sections of the ensemble mean of the model-simulated (a) meridional wind anomaly (m s^{-1}), (b) temperature anomaly (°C), and (c) relative humidity (%) averaged over the region of West Java (5.5°–8°S, 105.5°–108.5°E).

hPa. We also note a large warm anomaly near the tropopause (above 200 hPa) during this period.

The modulation of the meridional wind anomaly near the surface shown in Fig. 3.5a

is observed through the 2-month period, and the top of the anomaly varies from 800 to 400 hPa. Such a modulation is also observed in the temperature anomaly, and the layer of warm anomaly near the surface becomes deeper from 17 to 20 January with the top above 200 hPa. The warm anomaly extends from the surface to 200 hPa for the following 3 days or so. During the first half of January, there is not clear moist layer near the surface. After that period, a moist layer appears near the surface, the height of which varies from about 800 to 400 hPa.

The diurnal cycle is clearly seen in the temperature anomaly through the troposphere as shown in Fig. 3.6b. Particularly it is strong near the surface. The diurnal cycle of relative humidity is also evident near the surface through the two-month period.

Figure 3.7 shows the horizontal distributions of the ensemble mean of the model-simulated precipitation rate (color in mm hr^{-1}) and horizontal winds at 850 hPa (arrows in m s^{-1}) averaged for each pentad. Here, we only show 6 pentads, pentads 3–8, including pentad 7 (31 January–4 February) in which the heavy rainfall event occurred in Jakarta. In pentad 7, a zonally elongated rainband is formed around 5°–6°S, 106°–119°E. In that period, Jakarta is located at the western edge of the rainband as already noticed in Fig. 3.3. There is small amount of rainfall to the north and south of the rainband.

A cold surge is captured through pentads 5–7. In pentad 5, a typical Borneo vortex appears; the northeasterly winds over the South China Sea change their direction to southeastward over and around Sumatra, and the wind is roughly eastward over West Java. In pentad 6, eastern part of the vortex disappears, and further deformation of the vortex continues. In pentad 7, the winds over the South China Sea become almost northerly. The wind speed increases near West Java and the northerly component increases from pentad 6 to pentad 7. The northerly component of the surface wind intensifies upward motion on the northern slope of the mountain range in West Java. The surge event terminates in pentad 8.

In association with the modulation of horizontal wind field, the horizontal distribution of heavy precipitation changes from pentad to pentad. In pentad 5, weak precipitation

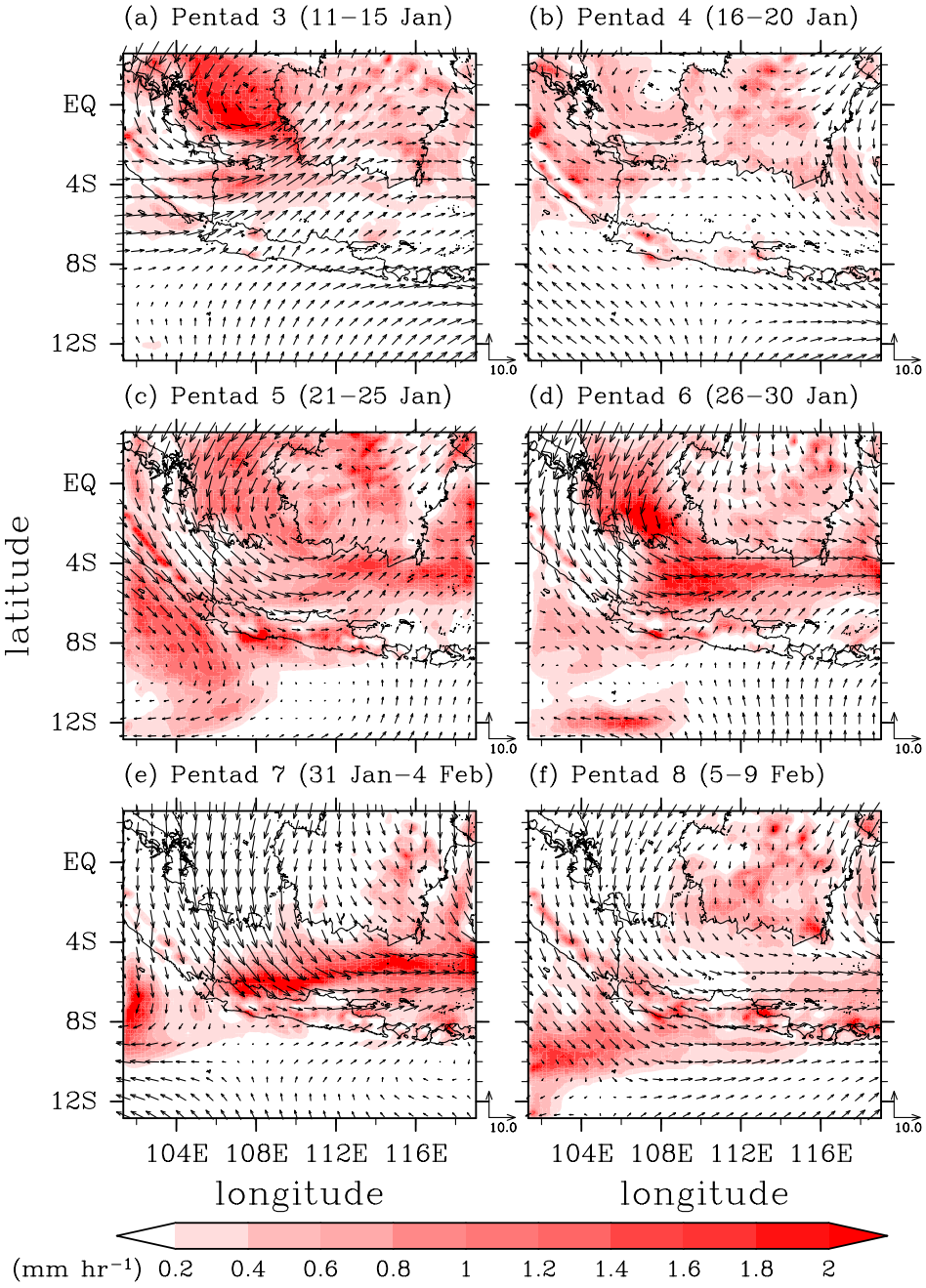

Figure 3.7: Horizontal distributions of the ensemble mean of the model-simulated precipitation rate (color in mm hr^{-1}) and horizontal winds (arrows in m s^{-1}) at 850 hPa averaged for each pentad. Unit vectors (10 m s^{-1}, 10 m s^{-1}) are shown on the bottom-right corner in each plot.

less than 1 mm hr^{-1} covers middle and northern parts of the computational domain with some intensification over the South China Sea. In pentad 6, heavy precipitation areas appear over the South China Sea and the Java Sea. In pentad 7, the heavy precipitation

area over the South China Sea disappears while that over the Java Sea moves southward to form the zonally elongated rainband. The rainband disappears in pentad 8.

Figure 3.8 shows the horizontal distributions of the ensemble mean of the model-simulated divergence of horizontal winds at 850 hPa (color in $\times 10e^{-5}$ s^{-1}) and horizontal winds at the surface (arrows in m s^{-1}) averaged for each pentad. The rainband in pentad 7 is consistent with the increase of convergence of horizontal winds at 850 hPa as shown in Fig. 3.8e. The convergence of horizontal winds (denoted with blue color) corresponds with the occurrence of precipitation, particularly it is clear over the ocean, as shown in Fig. 3.7. In the land region, a convergence-divergence pattern is obviously observed, which indicates a topographic effect of mountainous regions, for an example as seen along the southwestern coastline of Sumatra. The surface wind vectors show similar direction to those of the 850-hPa winds. However, the magnitude of the winds at the surface is reduced particularly over the islands.

3.3.3 Three-dimensional structures of the Borneo vortex and the cold surge

Figure 3.9 shows the latitude–height cross sections of the ensemble mean of the model-simulated temperature anomaly from the two-month average (color in °C), and meridional and vertical winds (arrows in m s^{-1}) averaged between 105.5°and 108.5°E for each pentad. In pentad 7 (Fig. 3.9e), in which heavy rainfall occurred at Jakarta, southward flow covers to the north of 7°S below the 800-hPa level. Large upward motion can be seen from the surface to 250 hPa over the convergence region of horizontal winds around 6°S near the front of the southward flow. The southward flow is associated with a cold anomaly as previously shown in Figs. 3.5b and 3.6b, which is clearer below the 850-hPa level. The large warm anomaly near the tropopause noted in Fig. 3.6b has the maximum just above the area of the large upward motion with a meridional extent of about 5°. In pentad 5 (Fig. 3.9c), on the other hand, the southward flow below the 700-hPa level is mostly warm. Near the center of the Borneo vortex (2°S), upward motion

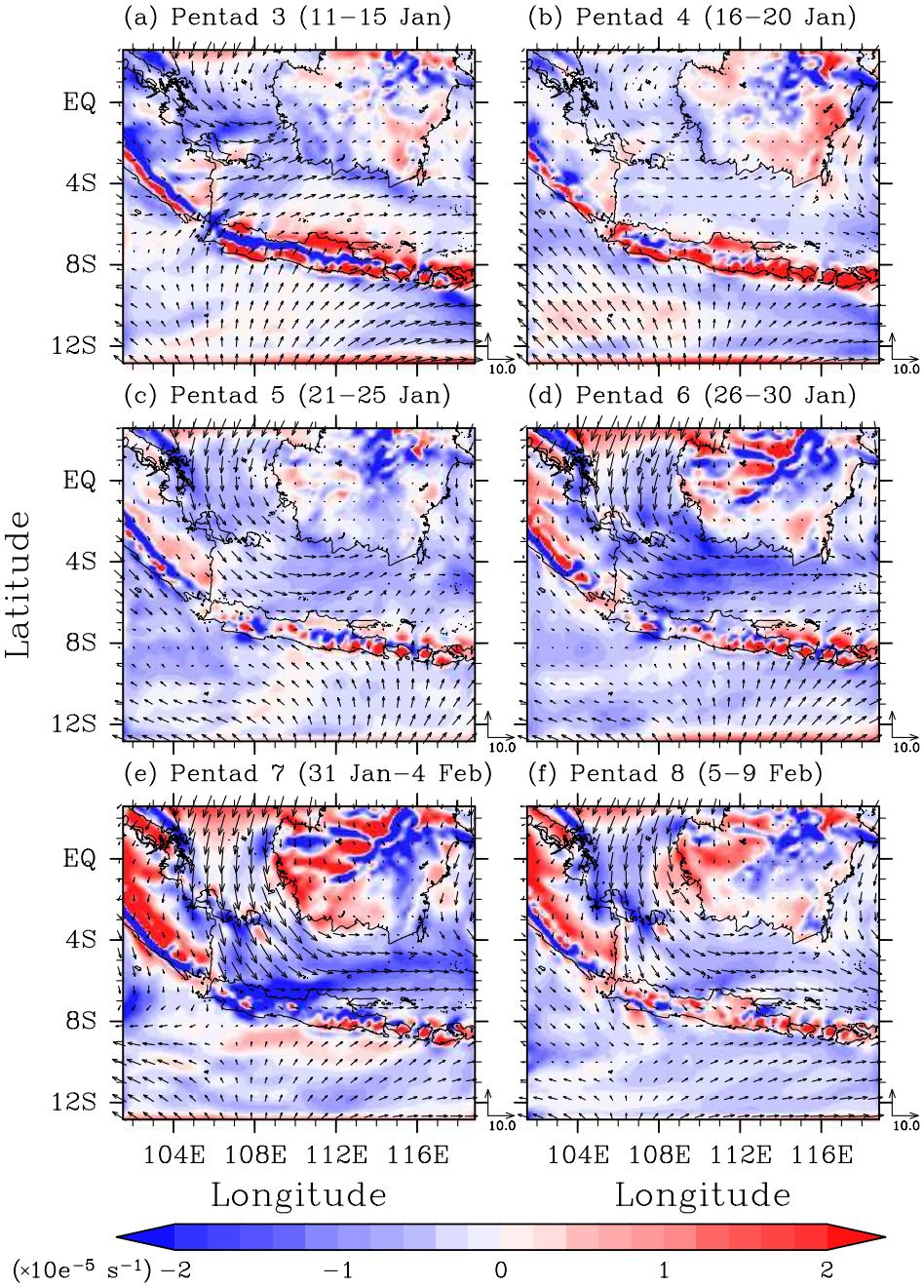

Figure 3.8: As in Fig. 3.7, but for the ensemble mean of the model-simulated divergence of horizontal winds at 850 hPa (color in $\times 10e^{-5}$ s^{-1}) and horizontal winds at the surface (arrows in m s^{-1}).

dominates throughout the troposphere with a warm anomaly centered at around 250 hPa. In pentad 3 (Fig. 3.9a), a similar upward motion with a warm anomaly at around 250 hPa is also observed near the center of the Borneo vortex (equator). From pentads 5–7, the

southward flow near the surface becomes colder and shallower; in pentad 5, the top of the southward flow is at 600 hPa, whereas in pentads 6 and 7, the top of the southward flow becomes 800 hPa. Note that in every pentad the upward motion exists at 7.5°S, which corresponds to the southern coast of Java.

Figure 3.10 shows the horizontal distributions of the ensemble mean of the model-simulated vertical winds (color in m s^{-1}) and horizontal winds (arrows in m s^{-1}) for pentad 5 (21–25 January) at (Fig. 3.10a) 300, (Fig. 3.10b) 500, (Fig. 3.10c) 700, and (Fig. 3.10d) 925 hPa, as well as (Fig. 3.10e) the ensemble mean of the model-simulated precipitation rate (color in mm hr^{-1}) and horizontal winds (arrows in m s^{-1}) at the surface, and (Fig. 3.10f) the TRMM precipitation rate (color in mm hr^{-1}) and QuikSCAT sea surface winds (arrows in m s^{-1}). The Borneo vortex is clearly identified from the surface to 700 hPa, whereas its appearance is not noticeable at 500 hPa. At 300 hPa, the wind direction is almost westward over the vortex. From the surface to 700 hPa, the center of the Borneo vortex shifts to the southwestward with height toward the southern South China Sea: (0°, 112°E) at 925 hPa (Fig. 3.10d), (1°S, 111°E) at 850 hPa (Fig. 3.7c), and (2°S, 110°E) at 700 hPa (Fig. 3.10c). Upward motion is dominant over the central part of Borneo and the areas to the west and south of the island from 925 hPa up to 300 hPa (Figs. 3.10a–d; see also Fig. 3.9c for the meridional cross section). The areas of large upward motion, including those to the south of Sumatra and Java, correspond well to the areas where precipitation in the model becomes large (Fig. 3.10e). The horizontal distribution of vertical winds shows the similar pattern through the troposphere with larger magnitude in the upper troposphere. Note that the small-scale pattern of the vertical winds over the islands seems to represent stationary gravity waves over mountainous regions.

The surface winds from QuikSCAT (Fig. 3.10f) show a good agreement with the model-simulated surface winds (Fig. 3.10e). Southward winds blow over the South China Sea, and turn to eastward over the Java Sea. On the other hand, northward winds blow to the south of Java. The distribution of precipitation in the model (Fig. 3.10e) is also in good agreement with that of the TRMM observation (Fig. 3.10f); precipitation is higher in the areas to the west and south of Borneo, and to the south of Sumatra and Java.

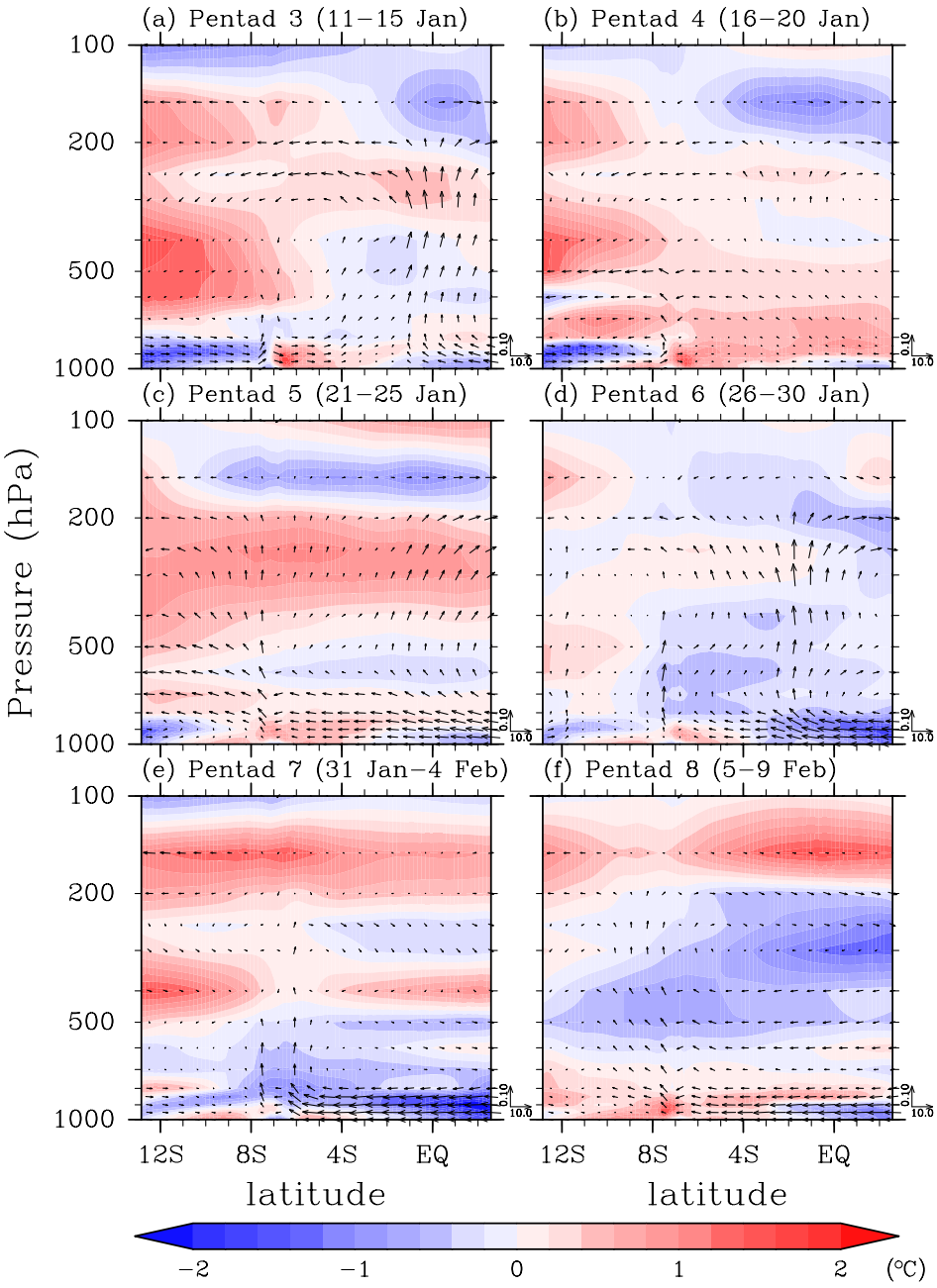

Figure 3.9: Latitude–height cross sections of the ensemble mean of the model-simulated temperature anomaly from the two-month average (color in °C), and meridional and vertical winds (arrows in m s^{-1}) averaged between 105.5°and 108.5°E for each pentad. Unit vectors (10 m s^{-1}, 0.1 m s^{-1}) are shown on the bottom-right corner in each plot.

Note that the pattern of precipitation in the observation (Fig. 3.10f) shows aggregates of spots, whereas that of the model simulation (Fig. 3.10e) shows a smooth distribution as a result of the ensemble mean. The ensemble mean pattern represents a probability of

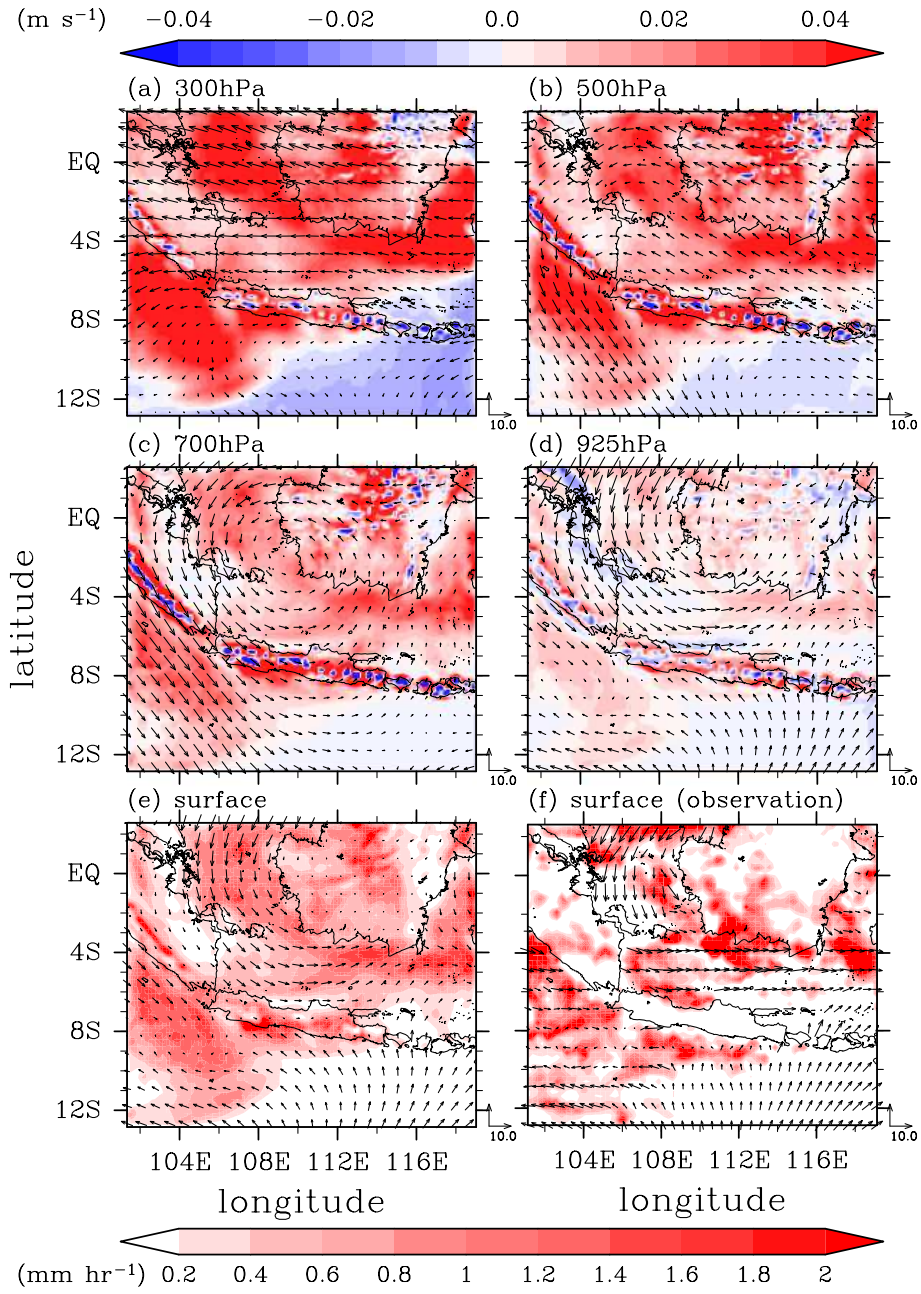

Figure 3.10: Horizontal distributions of the ensemble mean of the model-simulated vertical winds (color) and horizontal winds (arrows) for pentad 5 (21–25 January) at (a) 300, (b) 500, (c) 700, and (d) 925 hPa. Horizontal distributions of (e) the ensemble mean of the model-simulated precipitation rate and horizontal winds at the surface, and (f) the TRMM precipitation rate and QuikSCAT sea surface wind. The top color bar in the unit of m s^{-1} is for (a)–(d) and the bottom one in the unit of mm hr^{-1} is for (e),(f). Unit vectors (10 m s^{-1}, 10 m s^{-1}) are shown on the bottom-right corner in each plot.

the occurrence of precipitation, whereas each member of the ensembles shows aggregates of spots due to the distribution of rather isolated convective systems.

Figure 3.11 shows the same horizontal distributions as Fig. 3.10 but for pentad 7. Strong southward flow of the cold surge as shown in Fig. 3.9e is clearly seen from the surface (Fig. 3.11e) to 850 hPa (Fig. 3.7e), but it disappears at 700 hPa (Fig. 3.11c). Convergence of the horizontal winds associated with the cold surge and its continuation over the Java Sea produces large upward motions along the zonal band to the north of Java around 5°S–6°S and 106°–119°E through the troposphere (Figs. 3.11a–d). At 500 and 300 hPa, horizontal winds show divergence over the zonal band that corresponds to the band of heavy precipitation (Fig. 3.11e). Downward motion prevails outside the zonal band through the troposphere and little precipitation is observed there. The comparison of the surface winds between the model output and QuikSCAT also shows a good agreement in pentad 7.

3.3.4 Modulation of the statistics on precipitation rate

We use frequency distribution functions of ensemble simulation data to investigate the modulation of the statistics on the precipitation rate on the time scale of pentads. To give an illustration on the frequency distribution functions, Fig. 3.12 shows an example of probability distribution functions (Fig. 3.12a) and cumulative probability distribution functions or cumulative distribution functions (CDFs, Fig. 3.12b) for a waiting time $x+k$ years for Cayuga Lake to freeze k times, using a Negative Binomial distribution. The vertical axes in Fig. 3.12b show cumulative distribution function, which can be expressed as

$$\Pr\{\mathrm{X} \leq \mathrm{x}\} = \sum_{\mathrm{X} \leq \mathrm{x}} \Pr\{\mathrm{X}{=}\mathrm{x}\} \tag{3.1}$$

The figure and equation are taken from Wilks (2006). The uppercase letter X represents a generic random variable, or "an arbitrary or random future" value. The lowercase x represents a specific value of the random quantity. In the cumulative probability distribution, these specific values are plotted on the horizontal axis.

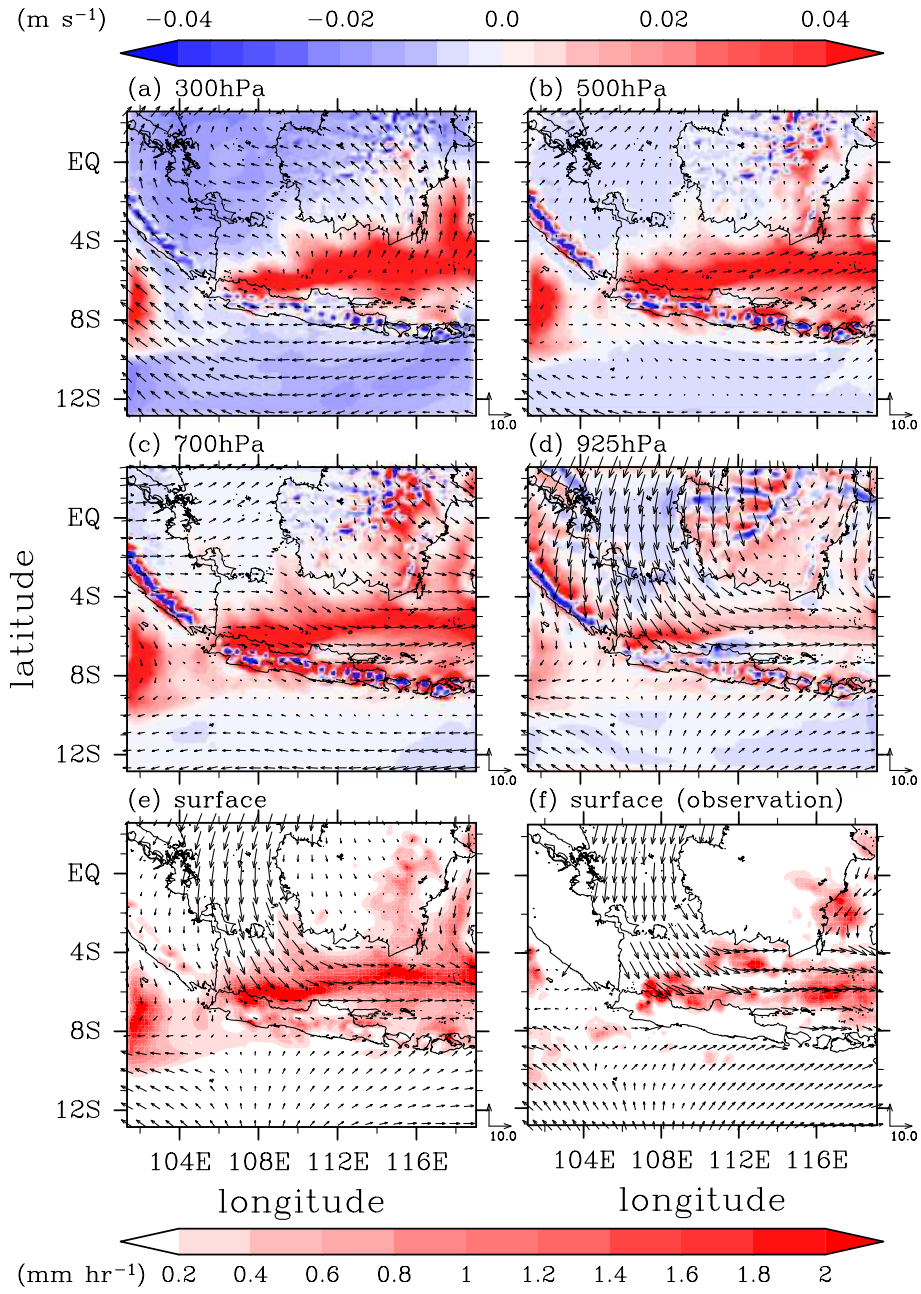

Figure 3.11: As in Fig. 3.10, but for pentad 7 (31 Jan–4 Feb 2007).

In the present study, the CDF of the model-simulated precipitation rate for each pentad is computed using grids in the land region of West Java (the hatched area in the inset map in Fig. 3.1) in the course of 5 days for the 9 ensemble members. When computing the CDF, we exclude grids without precipitation to avoid high probabilities for the bin of no precipitation in the histograms. Figure 3.13 shows the CDF only for

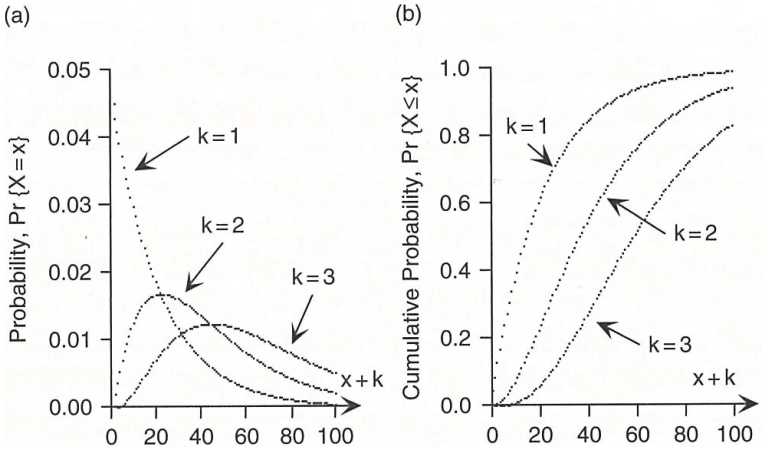

Figure 3.12: (a) Probability distribution functions and (b) cumulative probability distribution functions, for a waiting time $x + k$ years for Cayuga Lake to freeze k times, using a Negative Binomial distribution (from Wilks 2006).

the upper tail of the distribution (94%–100%) for each pentad as we focus on the heavy rainfall part. The fraction of grids with precipitation is also included in each panel, which is defined for each pentad as follows:

$$\text{fr} = \frac{\text{non-zero precipitation sample size}}{\text{total sample size}} \times 100\%. \tag{3.2}$$

For the first 3 pentads, the value of fr is less than 16%, whereas the highest value is about 48% for pentad 7 and the second highest value is about 38% for pentad 11.

The probabilistic modulation of precipitation is apparent in the CDFs. In the first three pentads, the fraction of heavy rainfall is smaller than that for the whole period denoted by the dashed curve, whereas in pentads 5, 7, and 10, the fraction of heavy rainfall is greater than that for the whole period. To quantify the modulation, we introduce a threshold value of 10 mm hr^{-1} for the heavy rainfall events (the vertical dashed line in each panel). In pentad 1–3, the contribution of the heavy rainfall is less than 1.2%, whereas those in pentads 5, 7, and 10 are 4.0%, 3.3%, and 3%, respectively. These numbers are about factor 3 or more compared to the minimum value during the 2-month period.

To find out local time dependence of the heavy rainfalls, Fig. 3.14 shows the diurnal variation of heavy rainfall occurrence over the land region of West Java (solid lines) and over the Java Sea (dashed lines; the box with a horizontal hatch pattern in Fig. 3.1) in

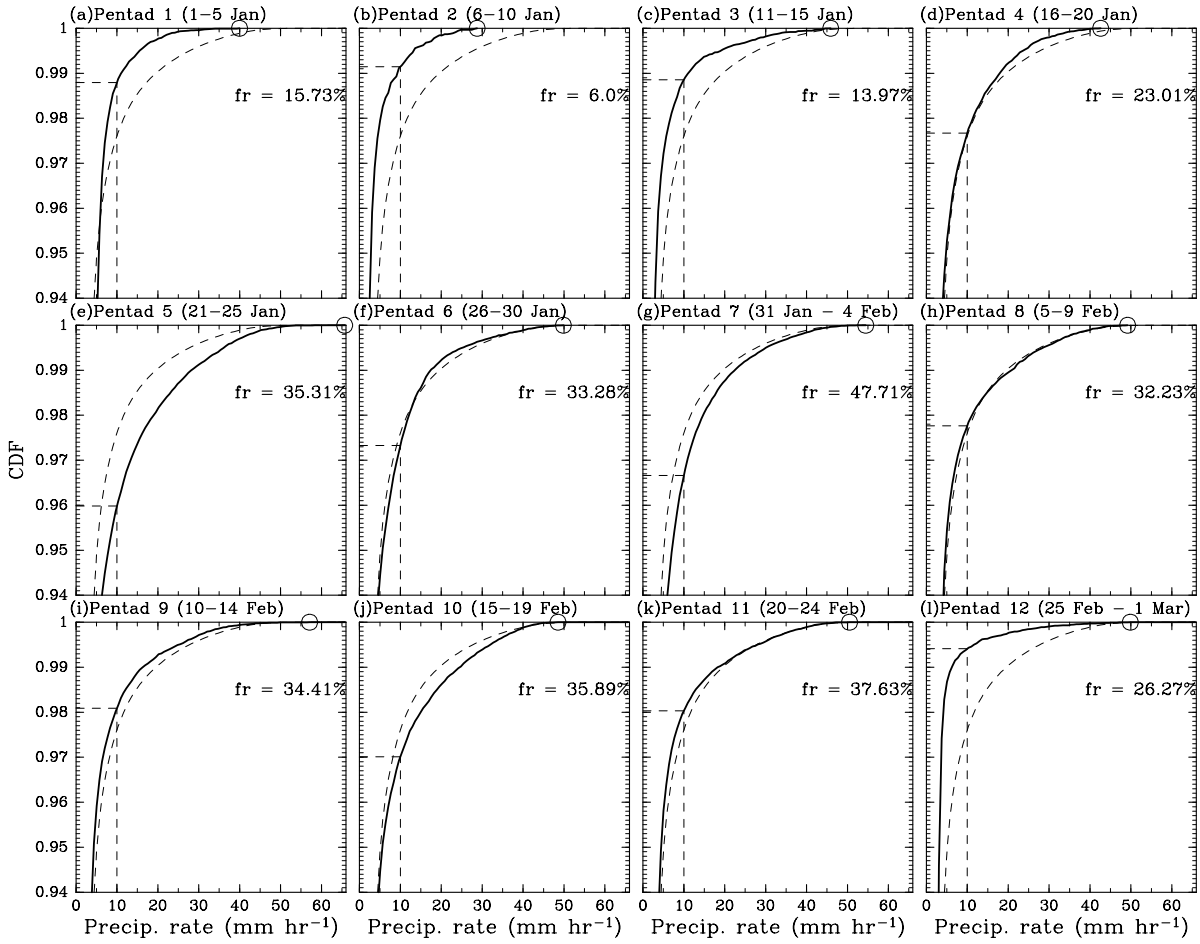

Figure 3.13: Cumulative distribution function of the model-simulated precipitation rate for (top left to bottom right) pentads 1–12 computed from all the ensemble members for grids in the land region of West Java. The dashed curve is the CDF for the two-month period. The circle denotes the highest value of rain rate in each pentad. The vertical and horizontal dashed line show the intersection point of the 10 mm hr^{-1} rain rate and its cumulative probability value. The value fr is defined by Eq. (3.2).

each pentad. Three different values of rain rate, 10, 20, and 30 mm hr^{-1}, are selected as a threshold value to define a heavy rainfall event, but we obtain a robust result that is not sensitive to the choice of the threshold value. As already seen in Fig. 3.13, heavy rainfall events over the land are frequently identified in pentads 5, 7, and 10, during which semidiurnal variations are dominant. That is, two peaks of the occurrence are clearly seen in these pentads. In pentad 7, the largest peak appears at 0500–0600 LT and the second peak appears at 2200 LT. In pentad 5, there are 2 peaks in the morning and in the evening with similar numbers of grids, while the largest peak appears in the late evening and the

second peak in the morning in pentad 10.

The maximum of heavy rainfall occurrence over the ocean appears in the morning in all pentads (dashed lines). Unlike over the land, the largest peak over the ocean appears in pentad 6, which is consistent with the southward movement of the rainband from pentads 6–7 as shown in Figs. 3.7d–e. The second largest peak over the ocean appears in pentad 3, which is the period of a Borneo vortex event. In pentad 7, during which the Jakarta flood event occurred, there are three peaks: 0200, 0700, and 1400 LT.

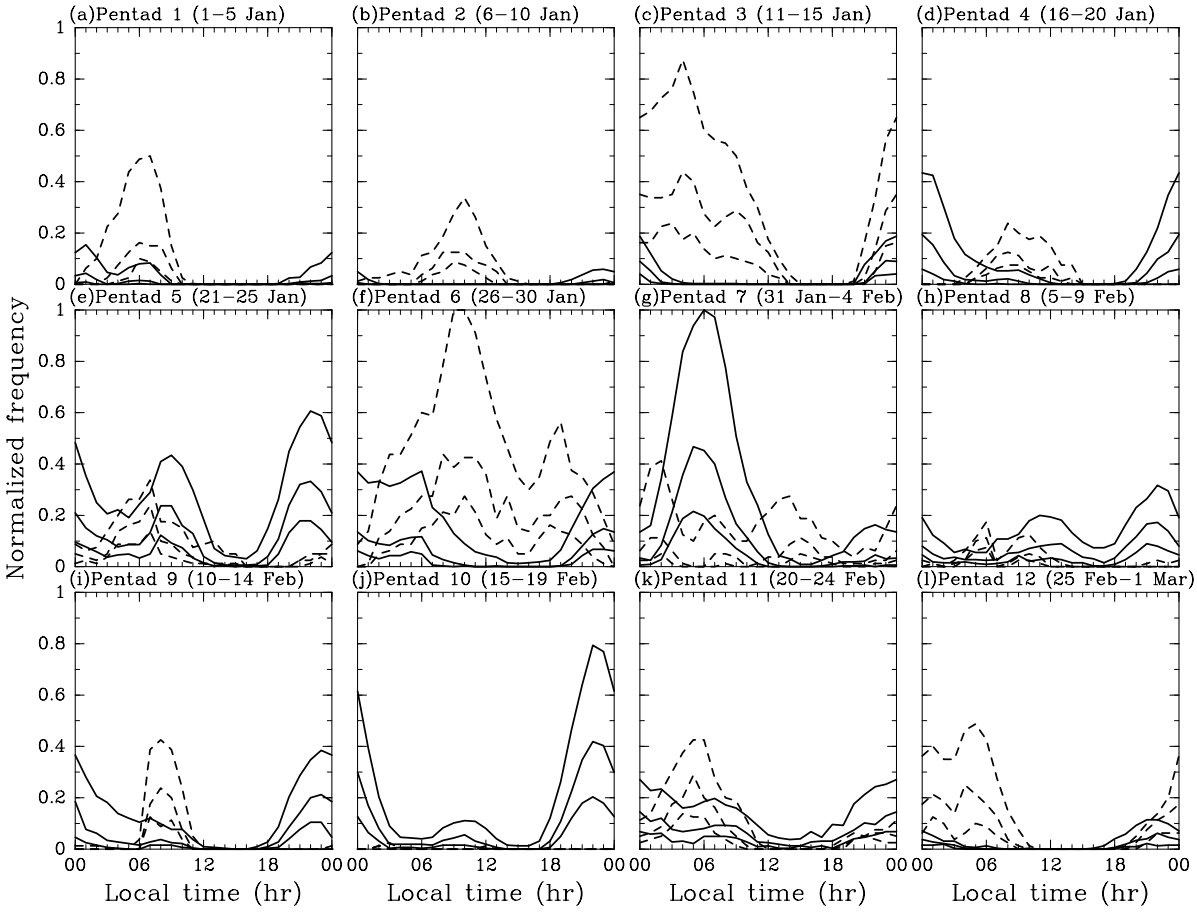

Figure 3.14: Diurnal variation of heavy rainfall occurrence in (top left to bottom right) pentads 1–12 over the land region of West Java (solid lines) and over the Java Sea (dashed lines) as illustrated in Fig. 3.1. The top, middle, and bottom lines for each region denote the normalized frequency of rain rate exceeding 10, 20, and 30 mm hr^{-1}, respectively. The frequency is normalized by the maximum value for 10 mm hr^{-1} for each region (325 grids in pentad 7 out of 6300 grids for land and 80 grids in pentad 6 out of 8145 grids for ocean).

3.4 Discussion

Cold surges have been studied for decades. Previous studies focused on large-scale features on time scales of submonthly to seasonal (e.g., Compo et al. 1999; Chang et al. 2005), or small-scale features on time scales of several days, including case studies (e.g., Wu et al. 2007; Tangang et al. 2008) and composite analyses (e.g., Compo et al. 1999). In contrast, this chapter investigates the modulation of heavy precipitation and related three-dimensional structures due to cross-equatorial monsoon surges around Southeast Asia on the time scales from less than one day to two months. It is confirmed that changes in the vertical profiles of moist thermodynamic conditions during the Jakarta flood event obtained by radiosonde observations (Wu et al. 2007) are associated with the three-dimensional synoptic field related to the cross-equatorial cold surge event that reached Java. Our model output gives the top of cold northerly as 1.5 km, or equivalently 850 hPa. This cold surge event is preceded by the Borneo vortex event as shown in Figs. 3.7c, 3.9c, and 3.10.

The Borneo vortex is centered at (1°S, 111°E) at 850 hPa in pentad 5, in which precipitation over West Java is relatively weak. Another Borneo vortex event is also captured by the model in pentad 3 (11–15 January, Fig. 3.7a), when the heavy precipitation occurred in the southern tip of Malay Peninsula, which faces the South China Sea, as reported by Tangang et al. (2008). Strong convergence associated with a northeasterly cold surge exists over a tip of Malay Peninsula during the event. Although Tangang et al. (2008) argued that this was not a vortex event based on reanalysis data with the 2.5° × 2.5° resolution, our model output with the 20-km resolution shows the existence of the vortex.

The shift of the center of the Borneo vortex with height as seen in Fig. 3.10 has a horizontal displacement of about 100 km, whereas the horizontal scale of the vortex is about 1000 km. This kind of slantwise structure with a similar geometry in the tropics is also reported by Otsuka and Yoden (2005), although they focused on a displacement of not a vortex center but a saddle point between two synoptic-scale vortices. Weakness of

geostrophic constraint near the equator may allow these slantwise structures within thin layers.

On the other hand, the vortex disappears in pentad 7, during which the heavy rainfall occurred at Jakarta. This is consistent with the fact reported by Chang et al. (2005) that the regions to the south of the South China Sea (viz., the Java Sea) experience enhanced convection when the Borneo vortex is absent.

We notice that signal of MJO is weak during the two-month period as shown in Fig. 3.3. To support this argument, Fig. 3.15a shows the time–longitude cross section of OLR (W m^{-2}) averaged between 5°N and 5°S. Propagation signal of a convective system (inferred from OLR $\leq$ 180 W m^{-2}) is captured from 106°E on 1 January to 180°E on 20 January. In other words, the signal has propagation speed of $\approx$4.7 m s^{-1}, which is comparable to the typical phase speed of MJO. To analyze the MJO cycle further, Fig. 3.15b shows (RMM1, RMM2) phase space points for the two-month period from 1 January to 28 February 2007. The points representing sequential days are joined by a line. In many cases, the sequential days trace anticlockwise circles around the origin, which signifies systematic eastward propagation of the MJO. Large-amplitude circles signify strong cycles of the MJO. However, the circle in Fig. 3.15b appears as a rather random motion near the origin, particularly during the second half of January to the first half of February. This indicates a weak MJO activity.

In pentad 7, more frequent occurrence of heavy precipitation is observed compared to other periods in the time series of precipitation for nine ensemble members as shown in Fig. 3.2b. For this ensemble experiment, well-sampled probability distributions are obtained by using the grids in the land region of West Java in the course of 5 days for all the ensemble members as shown in Fig. 3.13. The ensemble experiment with a relatively low-resolution model with a cumulus parameterization allowed us to capture the enhancement of localized heavy precipitation in pentad 7 compared to other pentads. On the other hand, a high-resolution experiment for the same period with only one member would be hard to obtain such statistics with the same computational resources; this is a trade-off. Note that the CDFs in Fig. 3.13 are normalized by the number of the grids

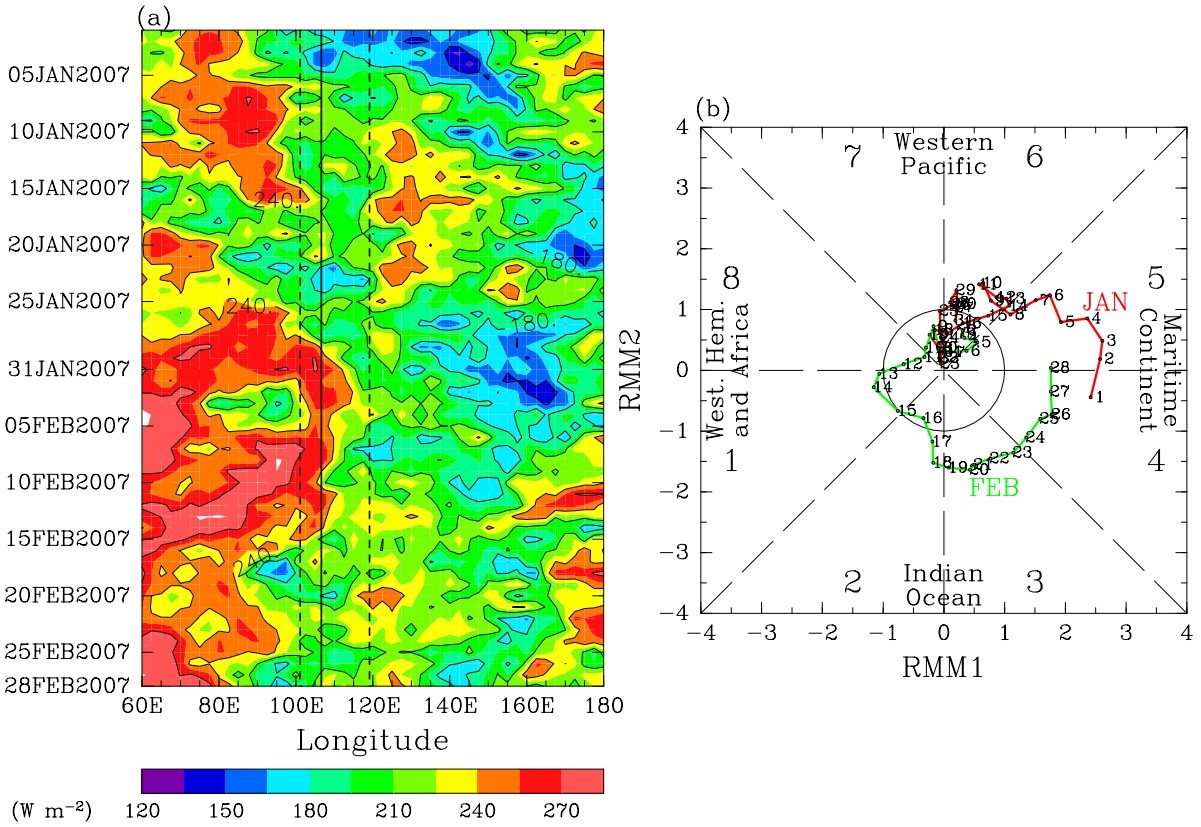

Figure 3.15: (a) Time–longitude cross section of Outgoing Longwave Radiation averaged between 5°N and 5°S. The vertical solid line denotes the longitude of 106.6°E which is the longitude of Pondok Betung Station. The vertical dashed lines denote the longitudinal boundary of Fig. 3.3. (b) (RMM1, RMM2) phase space points for two-month period from 1 January to 28 February 2007. Eight defined region of the phase space are labeled, as is the region considered to signify weak MJO activity. Also labeled are the approximate locations of the enhanced convective signal of the MJO for the location of the phase space, e.g., the "Indian Ocean" for phase 2 and 3.

with precipitation, so that the actual number of the grids with heavy precipitation is proportional to the value of fr times the value of the corresponding CDF.

As shown in Fig. 3.14, diurnal variation of heavy precipitation over the land usually has a peak in the late evening, whereas that over the ocean has a peak in the morning, which is consistent with the geographical distribution of the diurnal variation of precipitation estimated from satellite observations (e.g., Mori et al. 2004; Hirose and Nakamura 2005). Semidiurnal variation of heavy precipitation in some pentads implies that the coastal region of West Java is affected by convective systems of both over the land and

ocean. In pentad 7 (Fig. 3.14g), the highest peak of the occurrence of heavy rainfall over the ocean appears at 0200 LT, whereas that over the land appears around 0500–0600 LT. This time lag suggests that the convective systems are initiated over the ocean, move southward, and intensify over the land region. A similar time lag of the morning rain can also be seen in pentads 5 and 8, in which the semidiurnal variation is seen over the land. In such pentads, the morning rain over the ocean plays an important role to produce the semidiurnal variation over the land.

3.5 Conclusions

A time-lagged ensemble simulation using a regional numerical model is employed to investigate the modulation of precipitation over West Java in the two-month period of January–February 2007. Comparison between the numerical results and the TRMM 3B42 data shows a fundamental agreement on the temporal modulation of the spatial distributions of precipitation as shown in Figs. 3.2, 3.3, and 3.4 including the enhancement of precipitation on the time scale of pentads during the period of heavy rainfall, from 31 January to 4 February, during the Jakarta flood event. Comparison between the surface winds in the model and those of QuikSCAT also shows good agreement as shown in Figs. 3.10e,f and 3.11e,f.

In addition to the modulation of meridional winds reported by Wu et al. (2007), modulation of temperature and relative humidity is also investigated with the time–latitude cross sections (Fig. 3.5) and the time–height cross sections (Fig. 3.6). During the two-month period, several monsoon surges are observed, among which only the surge event during the Jakarta flood event is associated with the cold anomaly. The event is preceded by the Borneo vortex event in pentad 5 shown in Figs. 3.7c and 3.10. We have investigated the pentad-to-pentad modulation of synoptic fields and precipitation, and found that only pentad 7, which includes the Jakarta flood event, has the zonal band of heavy precipitation to the north of Java (Figs. 3.7e and 3.11e).

Further investigation on the vertical distributions of meridional and vertical winds and temperature anomaly (Fig. 3.9) indicates that the southward flow near the surface is getting colder and shallower from the period of Borneo vortex event (pentad 5) to the period of the cold surge event (pentads 6 and 7). The top of the cold northerly during the Jakarta flood event is about 1.5 km (850 hPa). The Borneo vortex in pentad 5 is clear from the surface to 700 hPa as shown in Figs. 3.9c and 3.10c. The vortex has a slantwise structure within such a thin layer under weak constraint of geostrophy near the equator.

A statistical analysis with a cumulative distribution function is employed to investigate the modulation of the probability of rainfall rate based on the samples over the land region of West Java with all ensemble members for each pentad. It is found that in pentad 7 the fraction of rain is highest for the two-month period as shown in Fig. 3.13g. Pentad 7 also marks one of the highest values for the contribution of heavy precipitation, which is about 3 times larger than the minimum value during the 2-month period. This is indicative of possibility of using this kind of quantity for the potential forecast of heavy precipitation in future as a product of ensemble forecasts. The diurnal cycle of occurrence of heavy rainfall is also modulated during the two-month period; in pentad 7, semidiurnal variation becomes dominant, and the largest peak appears in the early morning.

Chapter 4

Dependence of model-simulated heavy precipitation on the horizontal resolution

4.1 Introduction

In Chapter 1, we have reviewed the Jakarta flood event in February 2007 and showed that it was a tremendous event caused by heavy rainfall lasting several days — from late January to early February 2007 — in Jakarta and its vicinity. The heavy rainfall coincided with a strong and persistent trans-equatorial monsoon flow from the Northern Hemisphere (Wu et al. 2007). In Chapter 3, we investigated spatiotemporal modulation of precipitation and showed that the event associated with a cold surge was preceded by a Borneo vortex event. We also suggested that the convective systems initiated over the ocean, moved southward, and intensified over land, based on the time lag of the heavy precipitation between land and ocean during this period. This time lag is consistent with previous studies of diurnal cycle of precipitation, i.e. the diurnal variations in the tropics have their peaks in the late evening over land and in the early morning over adjacent sea regions (e.g., Houze et al. 1981; Mori et al. 2004).

The horizontal resolution of 20 km used in Chapter 3 was insufficient to reproduce the amount of heavy precipitation during the Jakarta flood event quantitatively. However, Seko et al. (2008) reported successfully reproducing the intense rainfall system that developed in Mumbai, India, on 26 July 2005 with a multinesting system with horizontal resolutions of 5 and 1 km. Increase of the horizontal resolution was a key factor for the reproduction of heavy rainfall, because the local topography with steep gradients around Mumbai was important for the occurrence.

Although many previous studies conducted high-resolution numerical experiments in the tropics, it is difficult to reproduce the exact location and timing of isolated convections which are generated almost randomly. Probabilistic information from ensemble simulations can be powerful in such a case. The case of the mesoscale convections in the tropics on the time scale of less than a day is not yet well understood.

The diurnal cycle of rainfall is widely known as a prominent feature in the tropical convective systems. To simulate this cycle realistically, it is necessary to resolve local circulations in association with the land-sea contrast and topographic complexity (e.g., Saito et al. 2001b). Because of the existence of spinup processes, ensemble simulations in the tropics may have biases on the diurnal precipitation cycle if all the ensemble members start from a single local time, as explained in Chapter 3. To avoid such a problem, we use a time-lagged ensemble technique in the present chapter.

The purpose of this chapter is to obtain further understanding of heavy precipitation during the Jakarta flood event and its reproducibility in the model, including the statistical nature of the precipitation. To achieve this goal, we perform ensemble numerical simulations with different horizontal resolutions. We also discuss the effects of cumulus parameterizations and local topography. In order to utilize probabilistic information, we compute cumulative distribution functions of hourly precipitation for different regions. In addition, we investigate diurnal variations of statistical values.

Table 4.1: Model subgrid-scale parameterization scheme for the 5-day period of simulations with 2-, 4-, 5-, and 20-km horizontal resolutions.

Process	Scheme			
	2km	4km	5km	20km
Cloud microphysics	6-class bulk microphysics			
Cumulus parameterization	Without cumulus parameterization		Kain-Fritsch scheme	
Radiation	GSM0412 scheme			
Boundary layer	Improved Mellor–Yamada Lv. 3			
Soil temperature	prognostic scheme (4-layer)			

4.2 Experimental design

In Chapter 4, we use JMA-NHM, the same regional mesoscale model as in Chapter 3, with a time-lagged ensemble technique to perform ensemble hindcast experiments from 0000 UTC 31 January to 2300 UTC 4 February 2007. The outer computational domain is the same as in Chapters 2 and 3, shown in Fig. 4.1. Hereafter, the experiment with this domain is referred to as EXP20km. The subgrid-scale parameterizations and their parameters in EXP20km follow Hayashi et al. (2008) and Chapter 3. We employ a modified Kain–Fritsch scheme as the cumulus parameterization. We set up three inner domains with one-way self-nesting: 250 $\times$ 250 grids with a grid spacing of 2 km (DOMAIN 2' as shown in Fig. 4.1), 150 $\times$ 150 grids with a grid spacing of 4 km, and 120 $\times$ 120 grids with a grid spacing of 5 km, centered in northwestern Java. Hereafter, the experiments with these domains are referred to as EXP2km, EXP4km, and EXP5km, respectively. EXP2km and EXP4km do not use cumulus parameterizations, whereas EXP5km uses the modified Kain–Fritsch scheme. Cloud microphysics, radiation, boundary layer, land surface, and lateral and upper boundary parameterizations employ the same schemes for all resolutions. To avoid the undesirable overestimation of the amount of upper-level clouds due to the third-order nonlinear numerical damping, the equivalent 1/e-folding time for the nonlinear numerical damping was increased by 4 times to weaken the nonlinear diffusion following Hayashi (2011). The subgrid-scale parameterization scheme is summarized in Table 4.1.

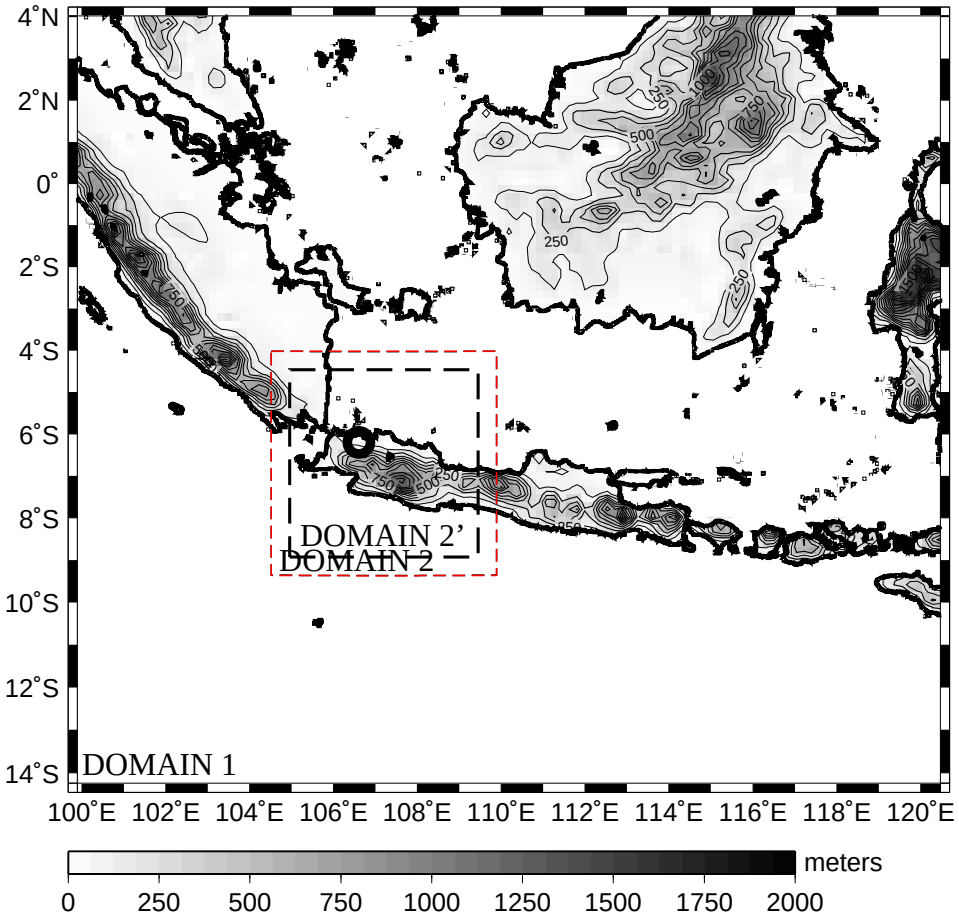

Figure 4.1: The model domains of 20- (DOMAIN 1), 4- and 5- (DOMAIN 2, the box with red dashed-line), and 2-km resolution (DOMAIN 2', the box with black dashed-line). Shading and contours show topography of 20-km resolution (m). The circle denotes location of the Pondok Betung Station.

Figure 4.2 shows the schematic diagram of the time-lagged ensemble used in Chapter 4. The initial and boundary conditions of the EXP20km are NCEP FNL, which are identical to those in Chapter 3. The outputs of EXP20km provide both initial and boundary conditions of EXP2km, EXP4km, and EXP5km. The initial data of EXP2km are given by the output of EXP20km at forecast time of 12 hours, and for EXP4km and EXP5km — by forecast time of 6 hours. To run the time-lagged ensemble simulation, we follow the procedure used in Chapters 2 and 3. Forecast lengths of EXP2km, EXP4km, EXP5km, and EXP20km for each simulation are 60, 66, 66, and 72 hours, respectively. Hourly model outputs are analyzed.

To justify the exclusion of the spinup data of the model results from the analysis,

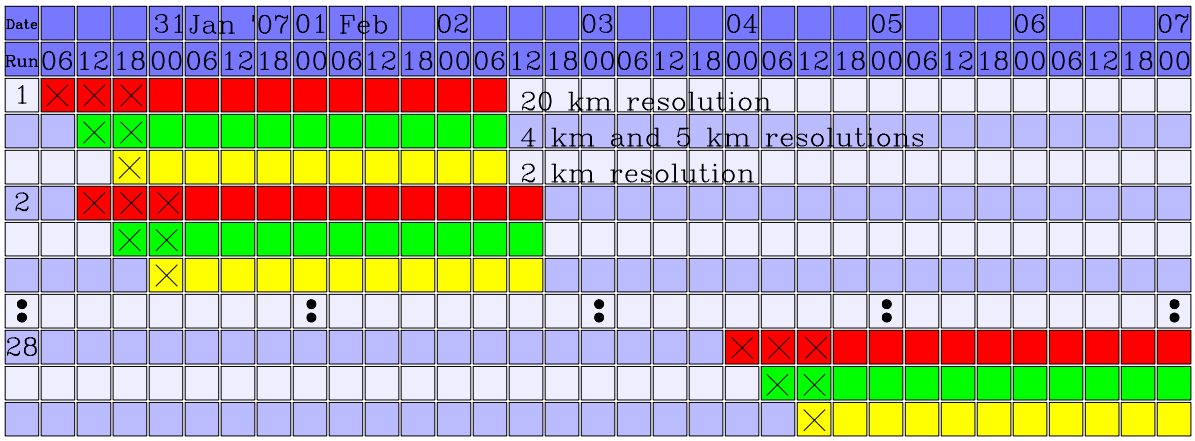

Figure 4.2: A schematic of time-lagged ensemble simulations. The "×" denotes the model output excluded from analysis.

Fig. 4.3 shows the composite time series of model-simulated precipitation as a function of forecast time for all resolutions. If we compute composite time series of precipitation rates for different local times of initial conditions (00, 06, 12, and 18 UTC), these time series show different evolution of diurnal precipitation for the first 6–18 hours, and that is why we discard the first 6–18 hours in the analyses. Some differences remain even after the first 18 hours. We therefore combined model runs with different local times of initial conditions to remove the biases in diurnal cycle shown in Fig. 4.3. By applying this procedure, the number of ensemble members becomes nine for all resolutions.

To validate the numerical results, we use the MTSAT IR1 data, which is cloud top temperature data for 0.05° × 0.05° grid boxes in every 1 hour, and the TRMM 3B42 product (Huffman et al. 2007), which is estimated rainfall data for 0.25° × 0.25° grid boxes in every 3 hours. The analyzed period is 5 days long, from 0000 UTC 31 January to 2300 UTC 4 February 2007.

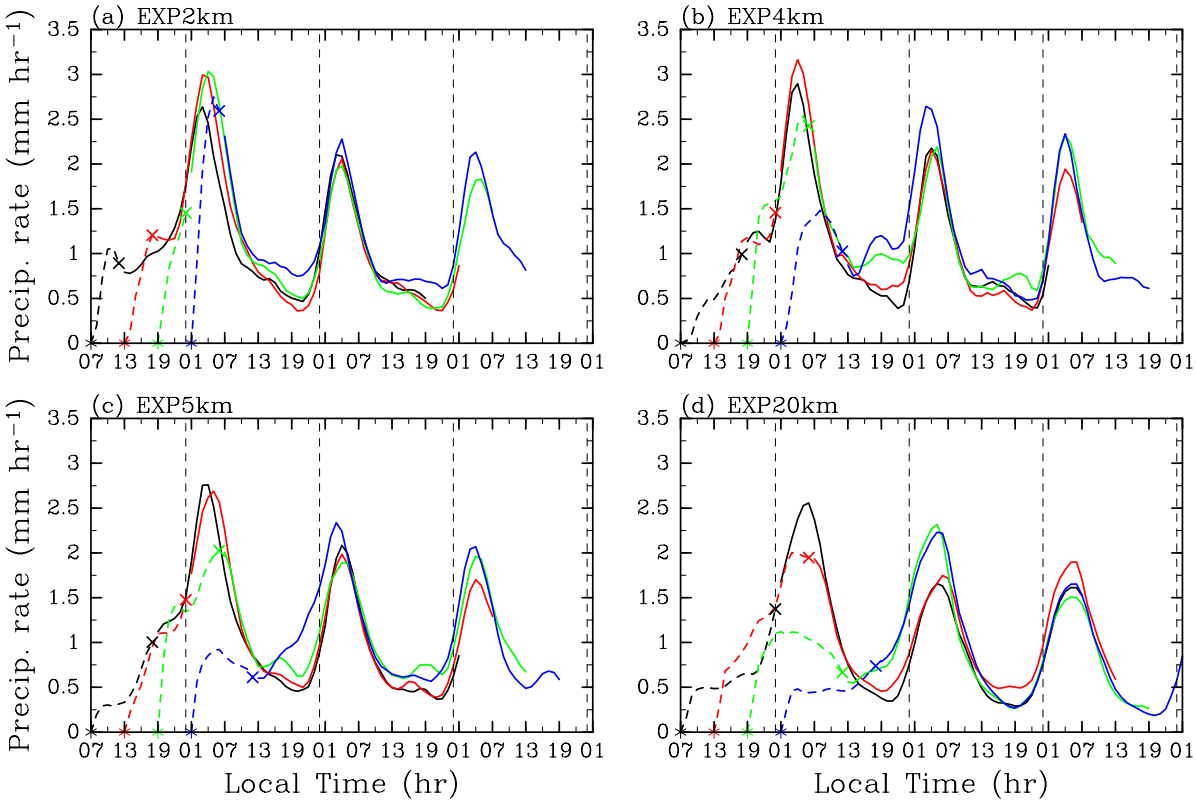

Figure 4.3: As in Fig. 2.4, but for (a) EXP2km, (b) EXP4km, (c) EXP5km, and (d) EXP20km, using all runs for the 5-day period.

4.3 Results

4.3.1 Comparison of precipitation and cloud top temperature between observational data and the model's outputs

Figure 4.4 shows (Fig. 4.4a) the time series of hourly precipitation rate of the Pondok Betung Observation data, and Figs. 4.4b–e — the superimposed time series of the model-simulated precipitation rate of the 9 ensemble members, which are represented by different color, of EXP2km (Fig. 4.4b), EXP4km (Fig. 4.4c), EXP5km (Fig. 4.4d), and EXP20km (Fig. 4.4e) at the nearest grid point to the Pondok Betung Station for the 5-day period from 0000 UTC 31 January to 2300 UTC 4 February 2007. In the observational data (Fig. 4.4a), heavy precipitation ($\geq$ 10 mm hr^{-1}) occurred in the first two days (1 and 2

February). The precipitation occurred twice a day, at midnight and before noon, while in the rest of the day in period, the precipitation intensity was low.

In the model's results, there is an improvement in terms of precipitation intensity from 20-km resolution to 2-, 4-, and 5-km resolutions (Figs. 4.4b–e). In particular, one of the ensemble members of EXP2km shows heavy precipitation at 2200 LT 1 February 2007, which corresponds to the observational data at the time. All the model's results reproduce nighttime (2100–0300 LT) precipitation, which is seen in the observational data, although there is a large bias in precipitation intensity in the EXP2km, EXP4km, and EXP5km results, particularly in the last 3 days of simulation period.

The three columns from top left to bottom right in Fig. 4.5 show horizontal distributions of EXP2km precipitation rate (color) and horizontal winds (arrows) for all the ensemble members. The rightmost column shows (top to bottom) TRMM 3B42 estimated precipitation rate, ensemble mean and ensemble standard deviation of the model-simulated precipitation rate. The valid time of the figure is 0300 LT 1 February 2007. All nine ensemble members simulate high precipitation in the northern coast of Java between 6°–6.2°S and 106°–109°E, despite the difference in the exact location. The area of high precipitation is consistent with the convergence of the winds. Member number 3 simulates the smallest region of high precipitation, located around 6°S and 106°–107°E.

TRMM 3B42 shows the region of high precipitation more eastward until the end of domain between 6°–6.5°S and 107.5°–109.5°E. The value of high precipitation is smaller than those of the model-simulated. The region of high precipitation is clearly seen in the ensemble mean. However, variation of precipitation is also large in this region, as seen in its ensemble standard deviation.

Five ensemble members (i.e. numbers 4–8) simulate another region of precipitation on the southern coast of Java. This signal of precipitation is observed by TRMM 3B42 around 8°S and 108.5°E. The signal still remains in the ensemble mean in the region between 8°S and 107°–109°E. In this region, variation of precipitation is large.

Figure 4.6 shows the horizontal distributions of cloud top temperature in K of MT-

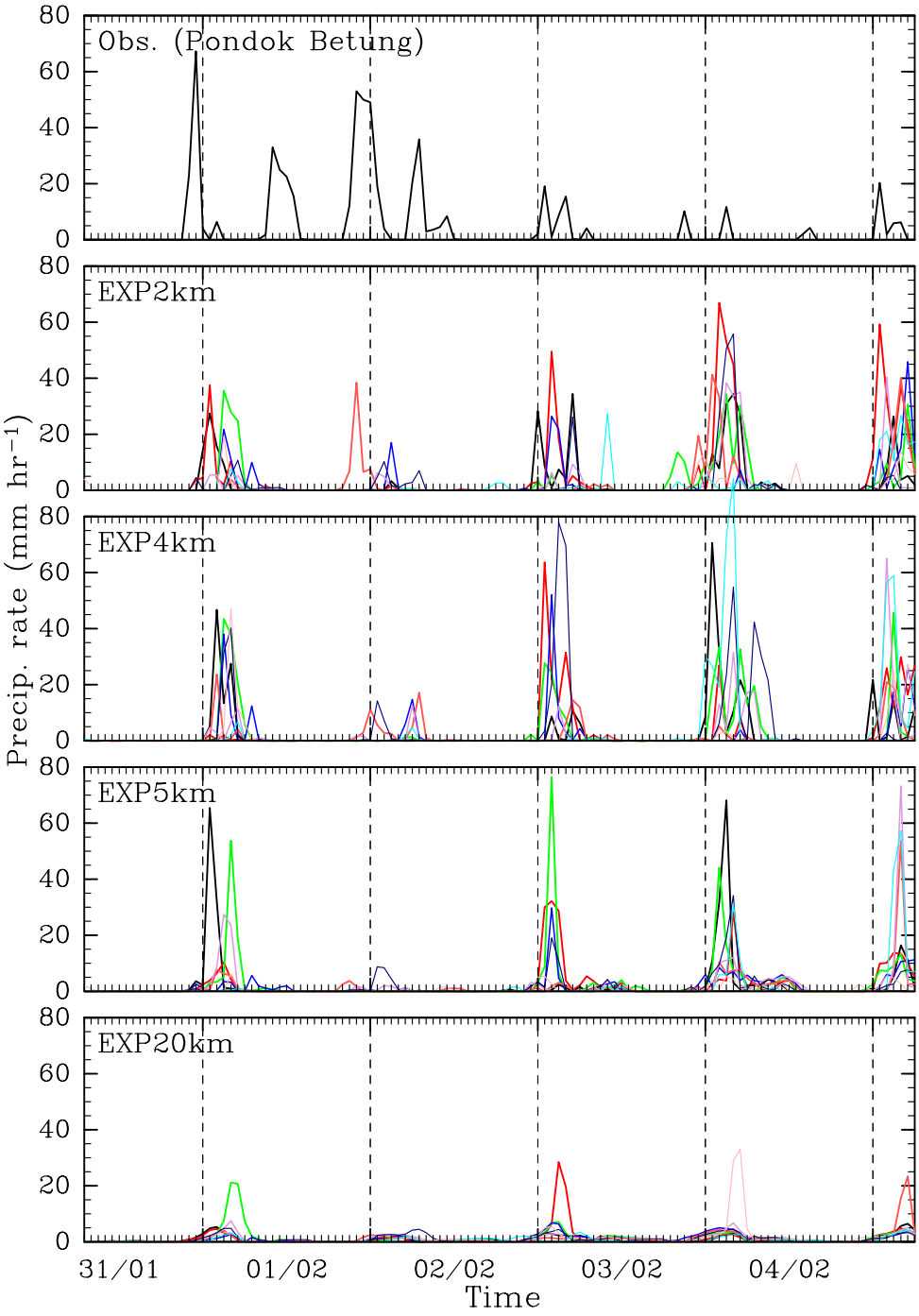

Figure 4.4: (top to bottom) Time series of hourly precipitation rate of the Pondok Betung Observation data and superimposed time series of the model-simulated precipitation rate for the 9 ensemble members of EXP2km, EXP4km, EXP5km, and EXP20km. Each color represents an ensemble member. The vertical dashed lines denote local midnight.

SAT IR1 data (Fig. 4.6a) and a particular ensemble member of EXP2km (Fig. 4.6b), EXP4km (Fig. 4.6c), EXP5km (Fig. 4.6d), and EXP20km (Fig. 4.6e) at 0300 LT 1

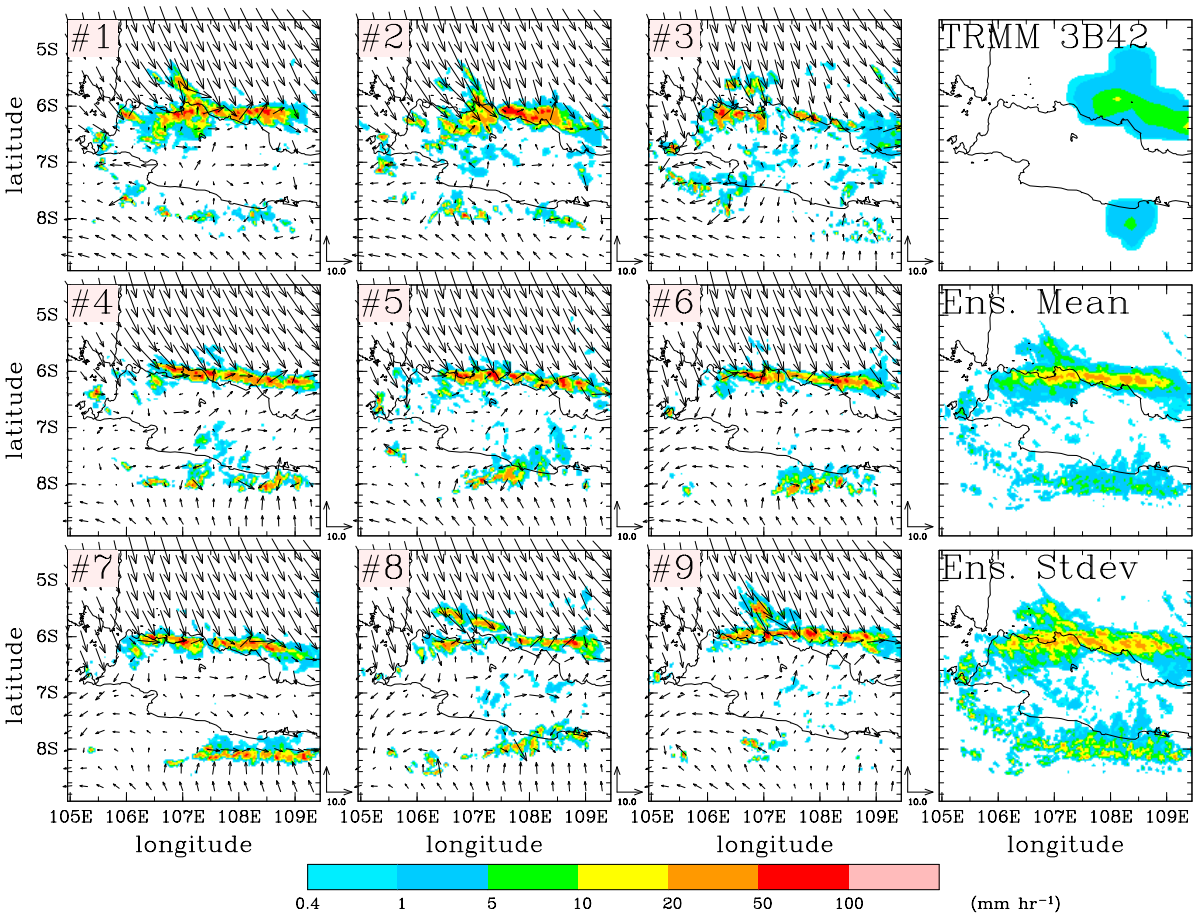

Figure 4.5: Horizontal distributions of (from top left to bottom right) EXP2km precipitation rate (color) and horizontal winds (arrows) for all the members of the ensemble, and (rightmost column from top to bottom) TRMM estimated rainfall, ensemble mean and ensemble standard deviation of the model-simulated precipitation rate at 0300 LT 1 February 2007.

February 2007. In Fig. 4.6a, a zonally elongated strong convective system is observed around 5.6°–7°S, 107°–109.5°E. Another region of convective activity is observed around the southern part of Java between 7.2°–9°S and 107.2°–108.4°E. Low clouds indicated by temperatures of 260–270 K cover half of the ocean to the north of Java and the inland area, and less than 15% of the ocean to the south of Java.

In the model (Figs. 4.6b–e), the strong convective system observed in Fig. 4.6a is reproduced well, regardless of the horizontal resolution and cumulus parameterization schemes. The characteristic horizontal scale of deep convection identified by low black-

body temperature (less than 230 K) of EXP2km is smaller than that of MTSAT IR1, whereas EXP4km and EXP5km show a scale comparable with that of MTSAT IR1. EXP5km and EXP20km produce a false convective cell to the west of Java, over the Sunda Strait (6.2°S, 105.5°E). On the contrary, EXP2km and EXP4km do not show the appearance of the convective cell over the Sunda Strait. All of the model results also reproduce the convective activity around the southern part of Java, although their reproducibility is not as good as in the northern part. The indication of low clouds is identified in all of the model results, even though the results with different resolutions show a different organization of the convective cells. EXP2km reproduces the low clouds in the inland area between 6.0°–7.8°S and 106.4°–108.6°E better than the others.

Figure 4.6 also shows the surface winds in the models. All the models show a convergence of surface horizontal winds along the northern coast of Java (Figs. 4.6b–e). A relatively weak convergence is also discernible to the south of the island, except for EXP20km (Figs. 4.6b–d). These convergence zones correspond to the convective activities to the north and south of the island.

As indicated by dashed lines in Fig. 4.6, four boxes are introduced to study the contrast of the distribution of precipitation in each region. From north to south, the boxes represent the Java Sea, the northern coast of Java, the mountainous region of Java, and the southern coast of Java (hereafter referred to as the ocean, the northern coast, the mountains, and the southern coast, respectively).

Figure 4.7 shows the horizontal distributions of TRMM 3B42 estimated precipitation (Fig. 4.7a), and a particular ensemble member of precipitation rate of EXP2km (Fig. 4.7b), EXP4km (Fig. 4.7c), EXP5km (Fig. 4.7d), and EXP20km (Fig. 4.7e) at 0300 LT 1 February 2007. In the TRMM 3B42 data, a zonally elongated rainband is observed around 5.6°–6.4°S, 107°–109.5°E. The rainband is associated with the strong convective system as shown in Fig. 4.6a. Another precipitation areas is located in the southern part of Java, around 7.8°–8.6°S, 108°–108.8°E. All the models also indicate the formation of a zonally elongated rainband to the north of Java. However, the zonal extent of the rainband is wider in all of the models compared to the TRMM 3B42 data. The structure

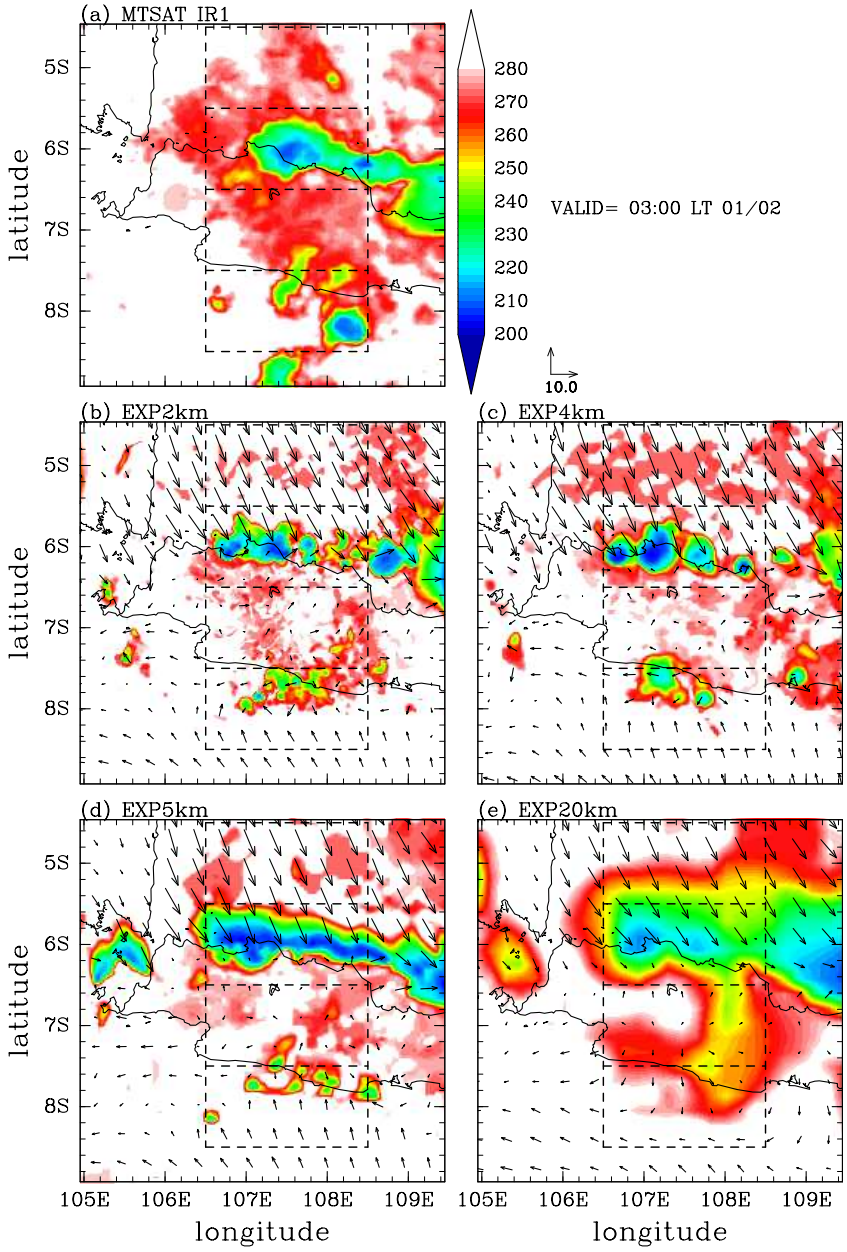

Figure 4.6: Horizontal distributions of cloud top temperature (K) of (a) MTSAT IR1 data and a particular ensemble member of (b) EXP2km, (c) EXP4km, (d) EXP5km, and (e) EXP20km at 0300 LT 1 February 2007. The initial time of simulation is at 1900 LT 29 January 2007. Arrows show surface horizontal winds in the models. Unit vectors of 10 m s^{-1} are shown above the panel "(c)". The four boxes in each plot represent, from north to south, the ocean, the northern coast, the mountains, and the southern coast. Each box covers an area of 1° × 2° in latitude and longitude.

of the rainband varies based on the model's resolution, and in EXP2km and EXP4km the rainband consists of a cluster of separate cells, whereas in EXP5km and EXP20km they form a single cell. The structures of the rainbands are similar to those of the strong

convective system shown in Figs. 4.6b–e. All the models also simulate the precipitation area in the southern part of Java as observed in TRMM 3B42. EXP5km and EXP20km produce precipitation over the Sunda Strait, whereas EXP2km and EXP4km tend to suppress it. This fact is consistent with the horizontal distribution of cloud top temperature as shown in Figs. 4.6b–e.

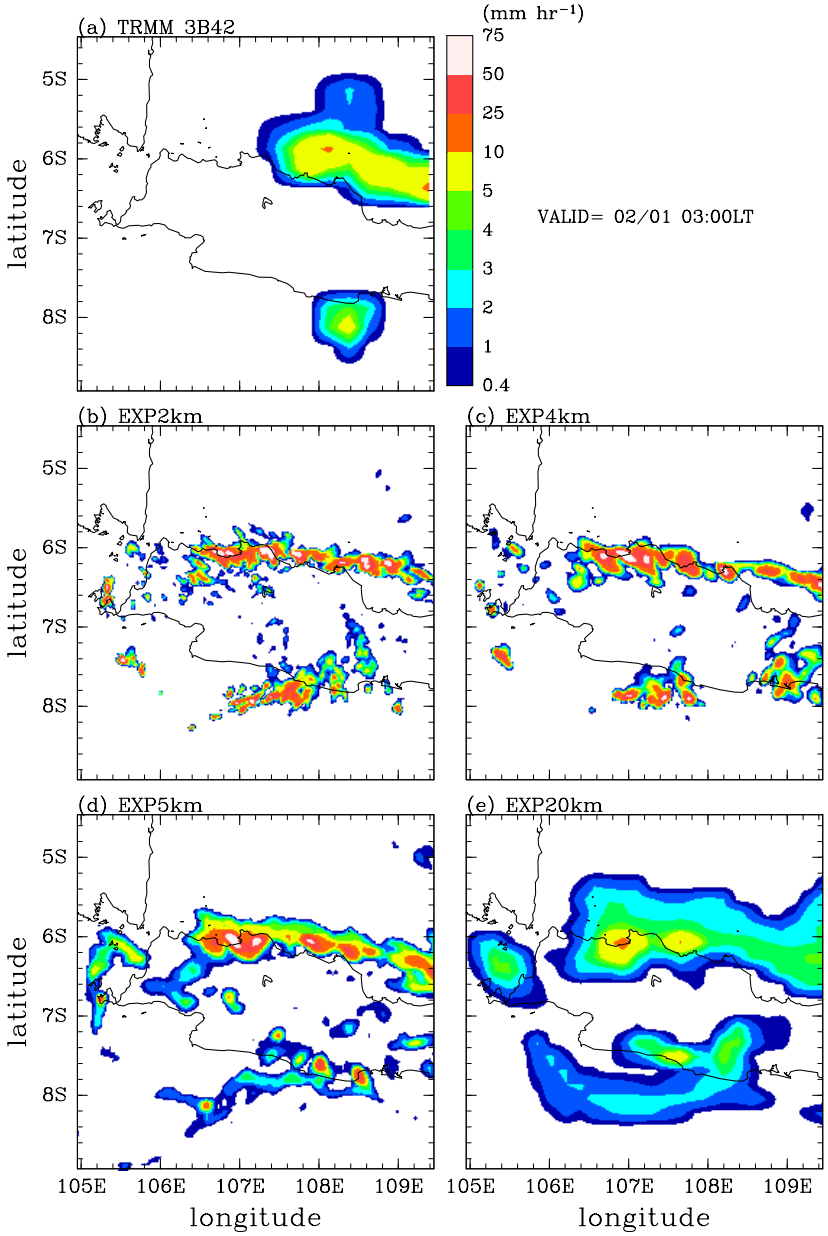

Figure 4.7: As in Fig. 4.6, but for precipitation rate (mm hr^{-1}).

4.3.2 Diurnal cycles of precipitation and cloud top temperature

Figure 4.8 shows diurnal variation of horizontal distributions of cloud top temperature of MTSAT IR1 data (Fig. 4.8a) and the ensemble mean of EXP2km (Fig. 4.8b), EXP4km (Fig. 4.8c), EXP5km (Fig. 4.8d), and EXP20km (Fig. 4.8e) averaged for the 5-day period. The figure shows 0100, 0400, 0700, 1000, 1300, 1600, 1900, and 2200 LT as indicated in the captions above the panels. In MTSAT IR1 (Fig. 4.8a), a zonally elongated strong convective system is observed over the northern coast of Java at 0400 LT. The strong convective system widens toward the ocean at 0700 LT, but as the day progresses, it starts to weaken and diminish. At 1900 LT, there is a remnant of the strong convective system over the ocean. However, another strong convective system exists over the land region between 6.5°–7.5°S and 108°–109°E. A strong convective system is observed over the northern coast of Java around 6°S and 106.2°E, which is near the Pondok Betung Station, at 0100 LT. A region to the south of 8°S is mostly clear from 0700 to 1600 LT. Convective activity over the region is observed in the evening to early morning hours (1900–0400 LT).

All the models (Figs. 4.8b–e) show typical diurnal cycles similar to that of MTSAT IR1 data, although we there are differences among them in terms of width and location of the region of convective activity. EXP2km and EXP4km share a similar pattern of convective activity over the northern coast region at 0100 LT with MTSAT IR1 data, whereas EXP5km and EXP20km show positive bias, i.e. more convective activity simulated in this region. The convective systems in EXP2km, EXP4km, and EXP5km are comparable in scale to that of MTSAT IR1, to some extent, whereas in EXP20km, the system is larger. This is consistent with Fig. 4.6b–e, which show a particular ensemble member at a given time, except for smoothing performed on EXP2km. All the models show a weak convective system to the south of 8°S. However, we note that EXP20km shows clearer hints of the convective system than the other resolutions in this region, particularly at 0100 and 0400 LT. Note that the plots shown in Fig. 4.8 are result from average over time and members. The result might shows spurious temperature distributions that do not exist in the real world.

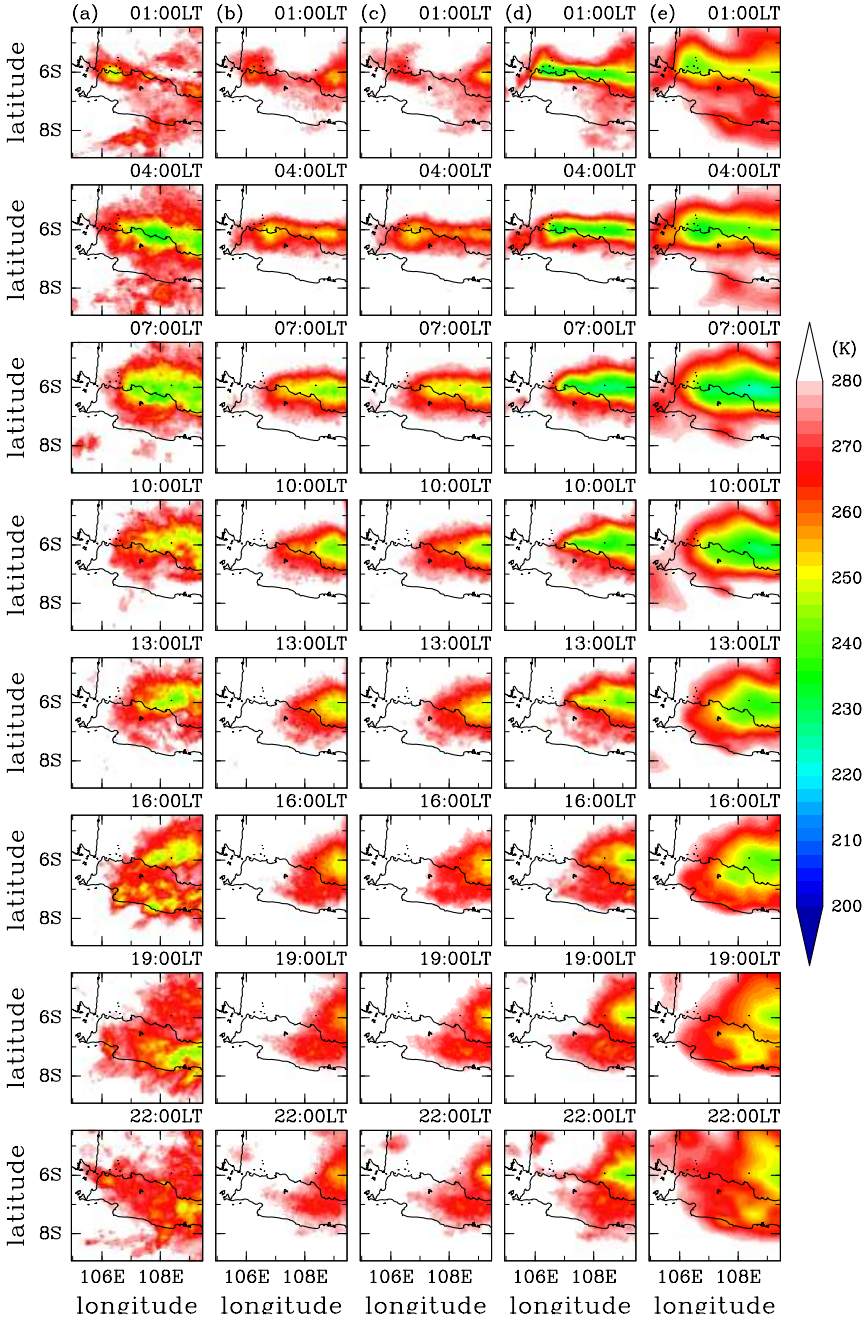

Figure 4.8: Horizontal distributions of cloud top temperature of (left to right)(a) MTSAT IR1 data, (b) EXP2km, (c) EXP4km, (d) EXP5km, and (e) EXP20km averaged over the 5-day period from 0000 UTC 31 January to 2300 UTC 4 February 2007. The plotted local times (top to bottom) are 0100, 0400, 0700, 1000, 1300, 1600, 1900, and 2200 LT.

Figure 4.9 shows the time–latitude cross sections of the TRMM 3B42 estimated precipitation rate (Fig. 4.9a) and the ensemble mean of the model-simulated precipitation rate of EXP2km (Fig. 4.9b), EXP4km (Fig. 4.9c), EXP5km (Fig. 4.9d), and EXP20km

(Fig. 4.9e) in mm hr^{-1} averaged between 106.5°and 108.5°E. In TRMM 3B42 (Fig. 4.9a), most of heavy precipitation ($\geq$ 10 mm hr^{-1}) occurs in the northern coast region, but not in the other three, throughout the five days. The meridional extent of the heavy precipitation is typically 2°, from 5°–7°S. Midnight enhancements of precipitation appear both in the northern and southern coast regions. The enhancement is clear in the northern coast region during the entire five-day period, whereas in the southern coast region, it is absent on 4 February.

In all of the models (Figs. 4.9b–e), high precipitation rate in the northern coast region is reproduced well during the entire simulation period. The meridional extent of high precipitation rate is about the same or greater than that of TRMM 3B42. Large-scale features in EXP2km, EXP4km, and EXP5km are largely dependent on EXP20km, although we notice some differences from resolution to resolution. The diurnal cycle is clear in all of the models, but not in TRMM 3B42. Note that passive microwave sensors used in TRMM 3B42 may underestimate precipitation systems that lack the ice phase over land (Huffman et al. 2007). The midnight enhancements of precipitation both in the northern and southern coast regions also appear in all of the models. EXP2km and EXP4km show the midnight enhancements of precipitation around 8°S in the southern coast region during the entire modeling period, whereas EXP5km and EXP20km do not show clear enhancements on 2 or 3 February. Propagation of enhanced precipitation signal from south to north in the mountains region, which starts around noon, is clear in EXP2km, EXP4km, and EXP5km, particularly on 31 January–2 February, whereas in EXP20km, the propagation is more like north-to-south. Propagation of enhanced precipitation signal from north to south is also discernible in the ocean region in EXP2km and EXP4km.

In TRMM 3B42 (Fig. 4.9a), propagation systems of precipitation are not clear. However, precipitation systems inferred from the cold cloud tops of MTSAT IR can be seen propagating from the ocean to the northern coast region during the five-day period (Fig. 4.10). In this figure, propagation of precipitation signal from south to north in the mountains region is also clear, particularly on 1 January. The diurnal cycle in Fig. 4.10

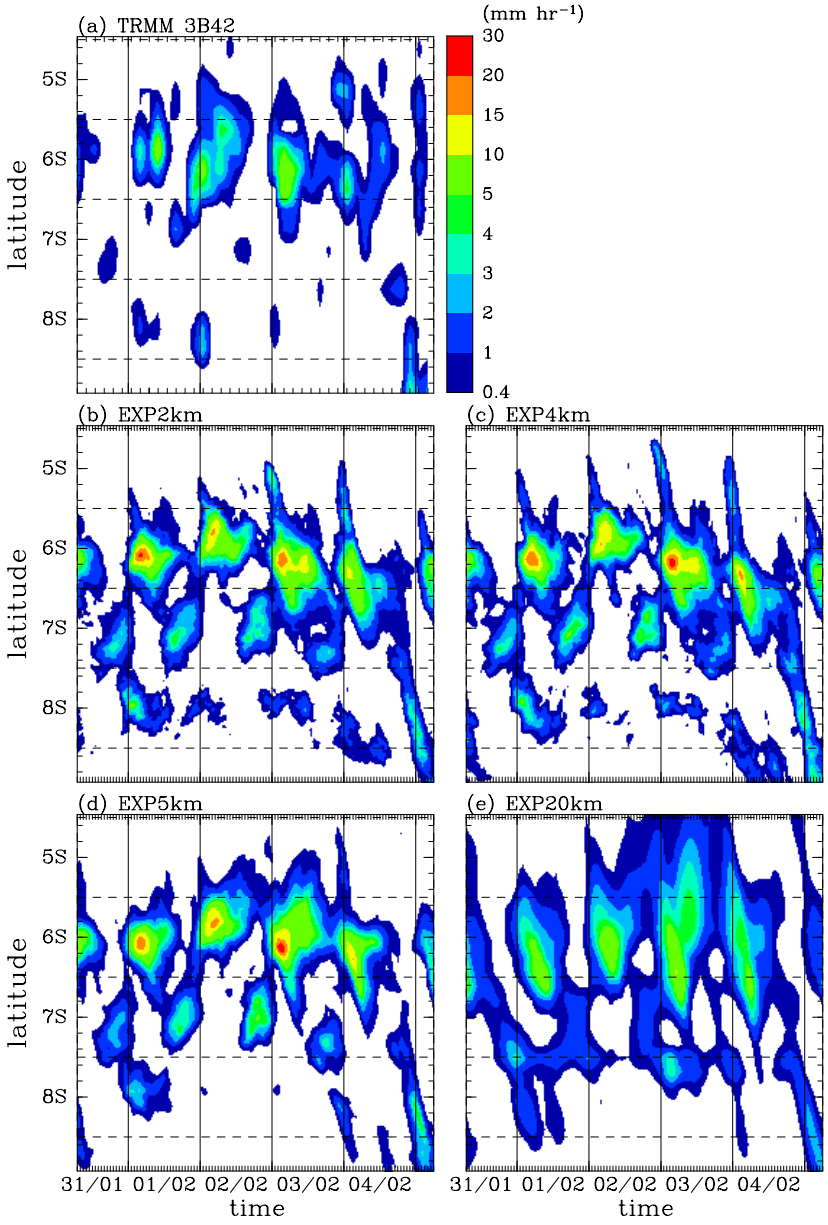

Figure 4.9: Time–latitude cross sections of (a) the TRMM 3B42 estimated precipitation rate (mm hr^{-1}) and the ensemble mean of the model-simulated precipitation rate (mm hr^{-1}) for (b) EXP2km, (c) EXP4km, (d) EXP5km, and (e) EXP20km averaged between 106.5°–108.5°E for the 5-day period from 0700 LT 31 January to 0600 LT 4 February 2007. The horizontal dashed lines show the latitudinal boundaries of the four boxes defined in Fig. 4.6. The vertical lines denote local midnight (0000 LT at Jakarta).

is clearer than in Fig. 4.9a.

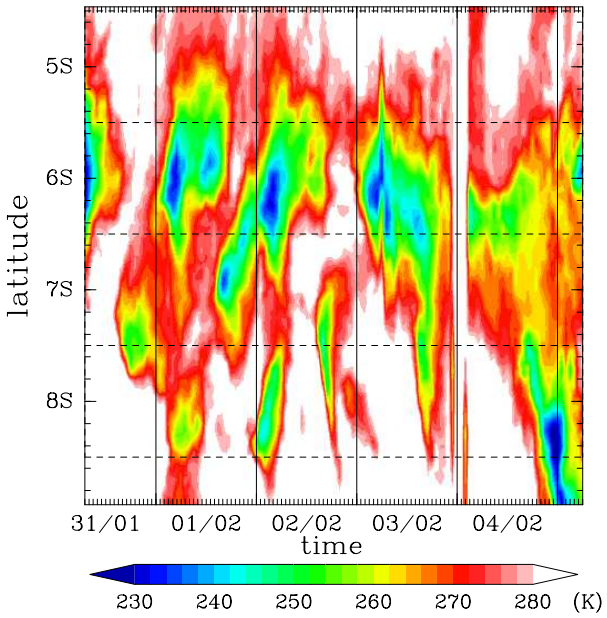

Figure 4.10: As in Fig. 4.9, but for the MTSAT IR1.

4.3.3 Precipitation rate statistics

Figure 4.11 shows a histogram of precipitation rate for (left to right) EXP2km, EXP4km, EXP5km, and EXP20km for (top to bottom) the ocean, the northern coast, the mountains, and the southern coast for all members. There is a large variation of values for different resolutions and different regions in the upper tail of the histogram. All the models show a high value of precipitation in the northern coast region, regardless of their adoption of cumulus parameterization scheme. Although, we notice that EXP5km has its highest intensity on the southern coast. However, EXP4km shows the highest value of precipitation in the northern coast region compare to the other resolutions. Higher resolutions tend to show a more gradual decrease of rainfall frequency as function of rainfall value. To further explore the characteristics of the upper tail, we analyze the CDFs of precipitation rates.

Figure 4.12 shows the (CDFs) of precipitation rates in mm hr^{-1} of TRMM 3B42 data (Fig. 4.12a), EXP2km (Fig. 4.12b), EXP4km (Fig. 4.12c), EXP5km (Fig. 4.12d), and EXP20km (Fig. 4.12e). These CDFs show the upper tail of the distributions (94%–100%) only, as we focus on the heavy rainfall part. To make a direct comparison, we compute

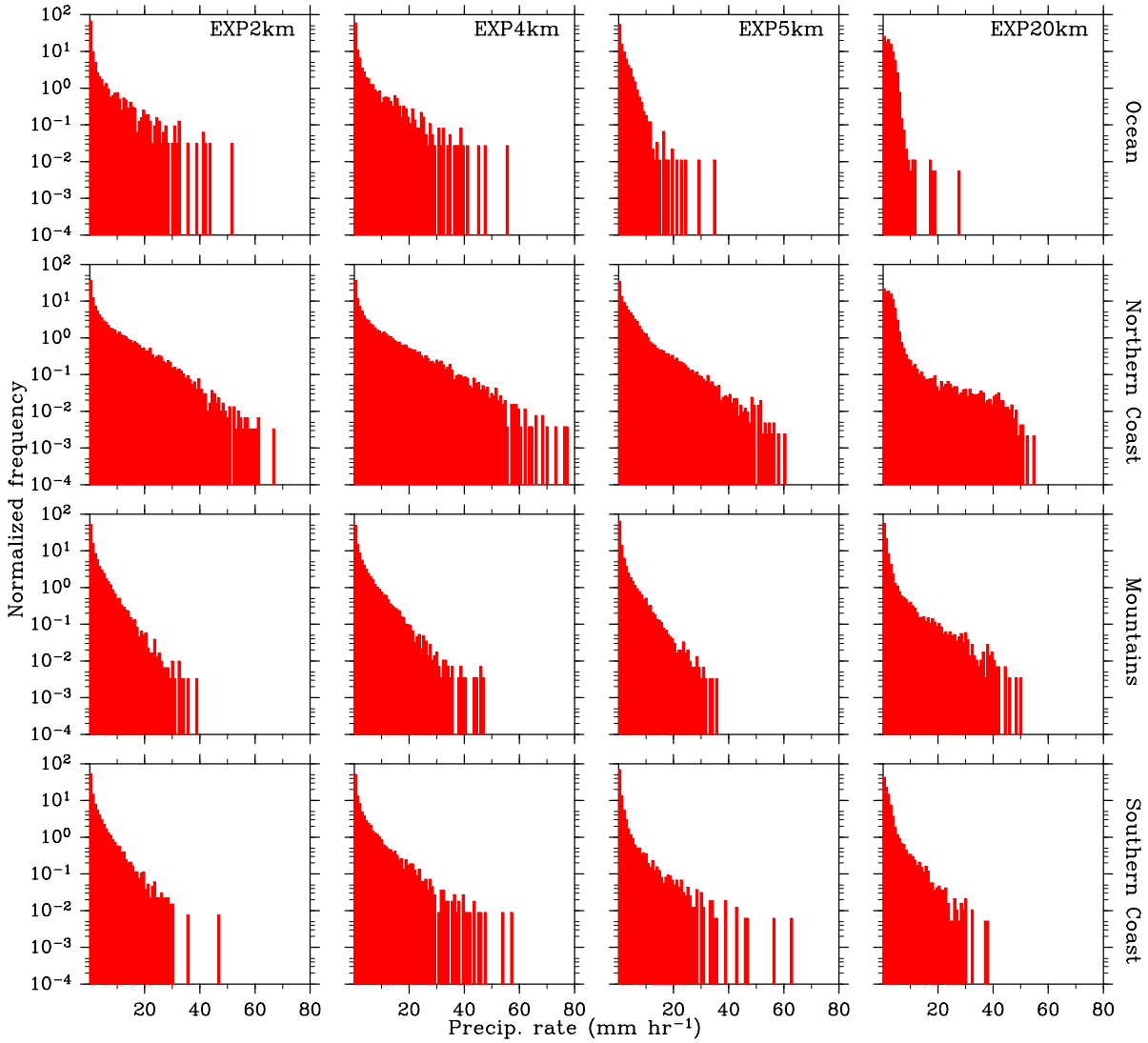

Figure 4.11: A histogram of model-simulated precipitation rate for (left to right) EXP2km, EXP4km, EXP5km, and EXP20km over (top to bottom) the ocean, the northern coast, the mountains, and the southern coast for all members.

a two-dimensional running mean of the EXP2km, EXP4km, and EXP5km results with a 20 km × 20 km grid and then interpolate the smoothed data to the EXP20km grids before computing the CDF. In TRMM 3B42 data (Fig. 4.12a), the CDF for the northern coast (red) shows the highest contribution of heavy precipitation to the total amount (over 12 mm hr^{-1} for the top 6%), whereas the lowest one is in the mountains region (green) — below 10 mm hr^{-1} for 100%. The lack of extreme precipitation, especially in the mountains region, may partly be due to the limitation of passive microwave sensors

over land, as noted in the previous subsection.

In the models (Figs. 4.12b–e), the fact that the northern coast region shows the highest contribution of heavy precipitation is well reproduced, except for EXP20km, indicating that the downscaling improves the statistical nature of heavy precipitation. EXP2km and EXP4km (Figs. 4.12b–c) show order of the CDF curves for the four regions consistent with that of TRMM 3B42, and EXP4km shows the highest precipitation rate for the upper tail of the CDF in the northern coast region. The maximum precipitation rate of the EXP4km is 77 mm hr^{-1}. The numbers in each panel contain information for the ultra high-end part of the CDFs; the maximum value of precipitation rate minus the precipitation rate at the 99% of the CDF for each region. In TRMM 3B42, the highest value of this measure is obtained for the northern coast region, and that value is greater than for the other regions by a factor of 50 or more. The only exception is EXP5km, in which the highest value is in the southern coast region. This is consistent with the histogram of precipitation rate previously shown in Fig. 4.11.

Figure 4.13 shows the frequency of heavy precipitation as a function of local time for TRMM 3B42 and EXP2km over the regions of the ocean (Fig. 4.13a), the northern coast (Fig. 4.13b), the mountains (Fig. 4.13c), and the southern coast (Fig. 4.13d). EXP4km shows a similar result, but EXP2km outperforms EXP4km in terms of the phase and amplitude of the diurnal variation (see Fig. B.1 for EXP4km). A robust result can be obtained using three different thresholds for each dataset: 2, 3, and 4 mm hr^{-1} for TRMM 3B42, and 20, 30, and 40 mm hr^{-1} for the models. In general, the model-simulated diurnal variation of heavy precipitation agrees well with that of TRMM 3B42. In the northern coast region, where the extreme rainfall probability is maximal, a broad peak with a minor local minimum extends from 0100 to 1000 LT for TRMM 3B42, whereas in the models, a relatively sharp peak exists at around 0400 LT (Fig. 4.13b). The midnight peak in the ocean region (Fig. 4.13a) is a few hours ahead of the peak in the northern coast region, whereas the morning peak in the mountains region in the model (Fig. 4.13c) is a few hours behind the one on the northern coast region. This is consistent with the propagation of precipitation from north to south shown in Fig. 4.9, as well as with the

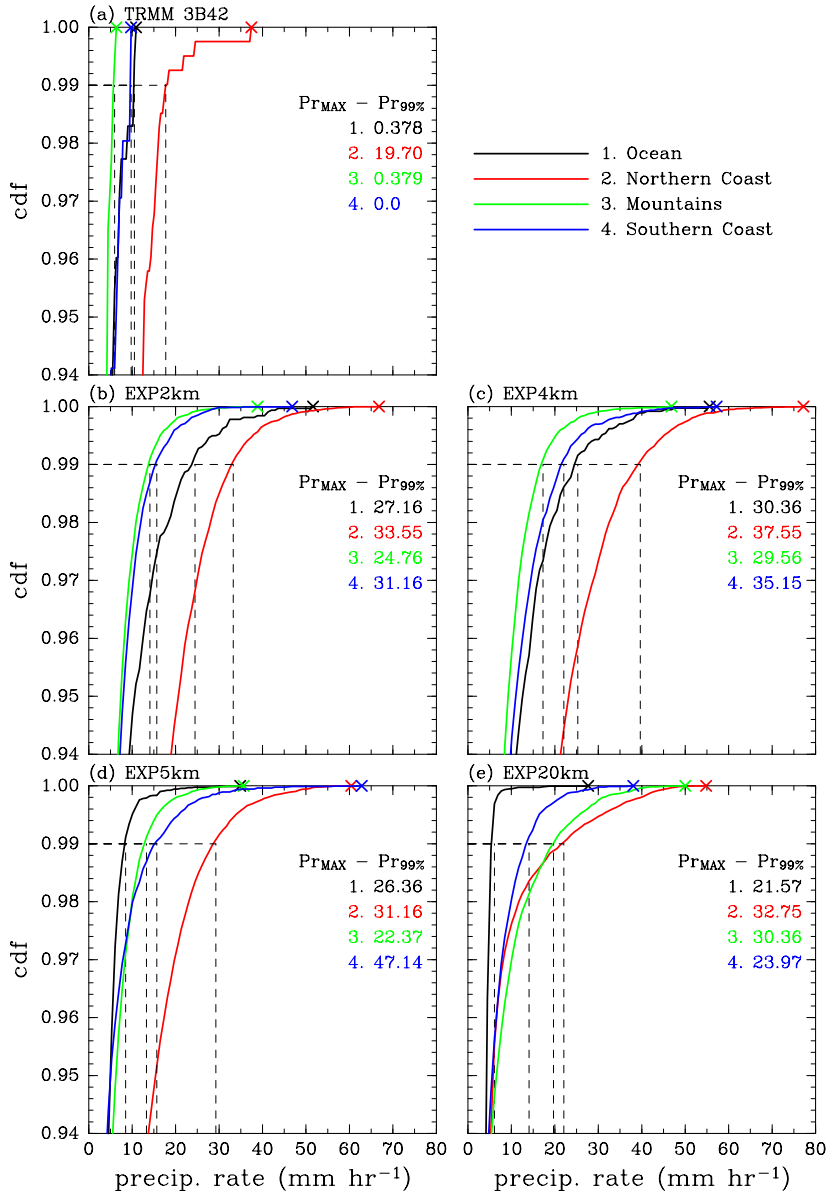

Figure 4.12: Cumulative distribution function (CDF) of precipitation rate (mm hr^{-1}) of (a) TRMM 3B42 and all of the ensemble members of (b) EXP2km, (c) EXP4km, (d) EXP5km, and (e) EXP20km for the regions of (1) the ocean, (2) the northern coast, (3) the mountains, and (4) the southern coast for the 5-day period. The cross denotes the maximum precipitation rate for each region. The vertical and horizontal dashed lines show the intersection of the 99% of CDF and the precipitation rate. The number in each plot is the maximum precipitation rate minus the precipitation rate at the 99% of the CDF for each region.

description in Chapter 3. Although the southward propagation is not clear in TRMM 3B42 due to limitation of the measurement, the propagation is clear in the MTSAT IR1 (see Fig. 4.10).

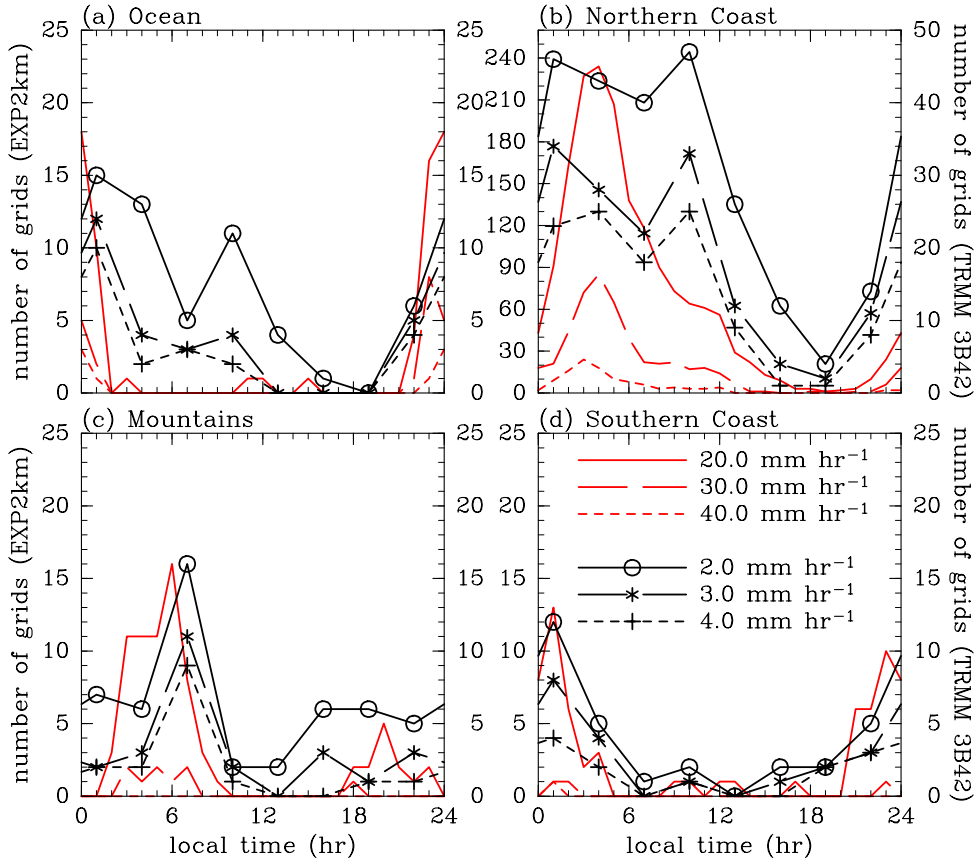

Figure 4.13: The frequency of heavy precipitation as a function of local time for TRMM 3B42 (black lines with symbols) and all the ensemble members of EXP2km (red lines) over (a) the ocean, (b) the northern coast, (c) the mountains, and (d) the southern coast. The right y-axis is for TRMM 3B42 and the left is for EXP2km. The legend inside Fig. 4.13d shows the threshold values for heavy rainfall, used for all the plots in Fig. 4.13.

4.4 Discussion

The models show good reproducibility of a strong convective system to the north of Java at a given time, as shown in Fig. 4.6. In particular, the characteristic horizontal scale of deep convections identified from black body temperature in EXP4km and EXP5km is comparable to that of the MTSAT IR1 data, regardless of the adoption of cumulus parameterization. However, EXP4km shows higher precipitation rates compared to EXP5km (Figs. 4.12c–d). The differences not only in the maximum value but also in the upper tail of the CDFs suggest that the cumulus parameterization scheme is also responsible for the frequency of heavy precipitation in the models.

Both TRMM 3B42 and the models show that most of heavy precipitation occurs in the northern coast region that includes Jakarta than the other three regions throughout the period of interest (Figs. 4.9, 4.13). Daily propagation of enhanced precipitation signal from south to north starting at around noon in the mountains region is clear in EXP2km, EXP4km, and EXP5km, particularly on 31 January–2 February (Fig. 4.9). The propagation in the mountains region was captured by the X-band radar, sited at the Pondok Betung Meteorological Observatory, Jakarta on 1 and 2 February, as shown in Fig. 4.14 (Fig. 6 of Wu et al. 2007). Daily propagation from north to south is also discernible in the ocean region in EXP2km and EXP4km. It is interesting to note that the heavy precipitation in the northern coast region in the first three days occurs at the time when the signals from north and south meet there.

In order to investigate the characteristics of heavy precipitation for the four regions (the ocean, the northern coast, the mountains, and the southern coast), we perform a statistical analysis with a CDF with all nine ensemble members (Fig. 4.12). The CDFs for the northern coast region show the highest contribution of heavy precipitation to the total for both TRMM 3B42 and the model results except EXP20km, demonstrating that the downscaling improves the accuracy of precipitation predictions. The diurnal variation of the frequency of heavy precipitation exhibits good agreement between TRMM 3B42 and the EXP2km (Fig. 4.12). In the northern coast region, TRMM 3B42 shows a broad peak in the frequency of heavy precipitation from 0100 to 1000 LT, whereas in the models, a relatively sharp peak exists at around 0400 LT.

4.5 Conclusions

Here, we have performed time-lagged ensemble downscaling experiments with a regional numerical model, JMA-NHM, to study dependence of precipitation on horizontal resolution. We ran the model with horizontal resolutions of 2, 4, and 5 km (downscaled from the 20-km runs). All the models demonstrate good reproducibility of the precipitation rate and cloud top temperature, in particular to the north of Java as shown in Figs.

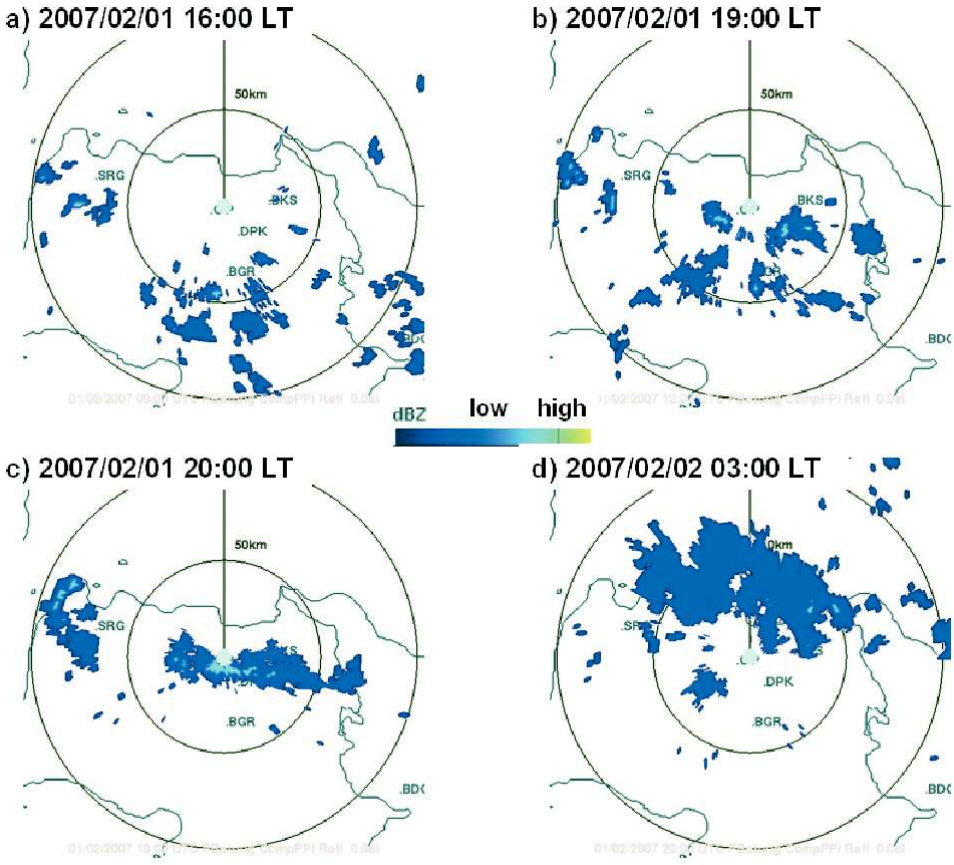

Figure 4.14: The X-band radar Plan Position Indicator (PPI) reflectivity display at the 0.5-degree elevation angle obtained at the Pondok Betung Meteorological Observatory, Jakarta for (a) 1600, (b) 1900, (c) 2000 LT on 1 February and (d) 0300 LT on 2 February 2007 (from Wu et al. 2007).

4.6 and 4.7. The characteristic horizontal scale of deep convections identified from black body temperature in EXP4km and EXP5km is comparable to that of the MTSAT IR1 data, regardless of the adoption of cumulus parameterization (Fig. 4.5).

The diurnal variation of cloud top temperature shows a strong zonally elongated of convective activity over the northern coast of Java in the morning (0400–0700 LT) in the TRMM 3B42 and all the models (Fig. 4.8). In both TRMM 3B42 and the models, most of heavy precipitation occur in the northern coast of Java that includes Jakarta than the other three regions throughout the five days of interest (Fig. 4.9). Daily propagation of enhanced precipitation signal from south to north starting at around noon in the mountains region is clear in EXP2km, EXP4km, and EXP5km, particularly between 31

January and 2 February (Fig. 4.9).

Moreover, we have applied analysis methods introduced in Chapter 3 in order to reveal statistical nature of heavy precipitation in the downscaling ensemble experiments for the four regions around West Java (Fig. 4.12) The CDFs for the northern coast shows the highest contribution of heavy precipitation compared to the other regions for all the experiments as well as for satellite-based precipitation estimates. The diurnal variation of heavy precipitation produced by the 2-km resolution model agrees well in terms of the timing and location of the diurnal cycle with that of the satellite-based precipitation estimates (Fig. 4.13).

In general, the performance of downscaling is good in the situation of Jakarta Flood event in February 2007, in which convective activities play an important role in the heavy precipitation. Finer resolution results show better performance on the precipitation over complex terrain of the mountains region.

Chapter 5

General Discussion

During the boreal winter monsoon, periods of strong northerly winds and anomalously low temperatures dominate the synoptic weather from Siberia to the South China Sea. These phenomena are known as "the cold surges." Although there are various definitions of cold surges, consensus exists on a few important characteristics in East Asia: a sharp drop in temperature, accompanied by a strengthening of the climatological northerly winds and an increase in surface pressure (Compo et al. 1999). Absolute agreement on a definition for surges is difficult to find, probably because individual researchers construct definitions based on the local response to the surge. Different properties have been attributed to cold surges — pressure surges (e.g., Boyle and Chen 1987; Compo et al. 1999), because cold-air outbreaks are accompanied by increasing surface pressure, or "northerly surge" — a term preferred by Wu and Chan (1995, 1997) to highlight the increase in wind speed that is predominantly from the north. During the two-month period of simulation in January–February 2007, several monsoon surges have been simulated in the model, among them only the surge during the Jakarta flood event was associated with a cold anomaly. This suggests that the sharp drop in temperature does not always accompany the intensified northwesterly monsoon surge over the Java Sea. Moreover, presumably the anomalous low temperatures over the Java Sea occur only during the strong cold surges.

Cyclonic vortices often form in the troughs of the lower troposphere over the equato-

rial regions of the South China Sea and the West Pacific during the boreal winter monsoon (e.g., Cheang 1977; Johnson and Houze 1987; Chang et al. 2003). Although cyclonic circulation may not be completely closed on the east side of Borneo, it is often referred to as the Borneo vortex and is often associated with deep convection and intense heat release (Cheang 1977; Chen et al. 1986; Lau and Chang 1987; Johnson and Houze 1987; Chang et al. 2003). Our model shows that the Borneo vortex with a horizontal scale of 1000 km and a vertical scale of 3 km has a slantwise structure within such a thin layer under weak constraint of geostrophy near the equator. Furthermore, a distinct center of the Borneo vortex in pentad 3 and 5 is obvious, as shown in Fig. 3.7, which gives the horizontal distributions of the ensemble mean of the model-simulated precipitation rate and horizontal winds at 850 hPa. In pentad 3, the winds are mostly southwesterly over the Indian Ocean (8°–12°S, 104°–116°E), Java and the Java Sea. The area of precipitation is confined near the center of the Borneo vortex at 0°, 108°E. This description is similar to the characteristic of convection over the South China Sea as described by Chang et al. (2005) in the presence of vortex during no-surge days. In pentad 5, however, the center of the Borneo vortex shifts southeastward and is over 1°S, 111°E. The precipitation distribution in pentad 5 is similar to the vortex and surge cases in the description by Chang et al. (2005). This suggests that the variability of the center position of the Borneo vortex may be affected by a northerly surge associated with the Asian winter monsoon.

The diurnal cycle of precipitation is a prominent feature in tropical convective systems. Therefore, simulating the diurnal cycle is one of the parameters in judging the success of a numerical experiment and at the same time is a challenging subject in the tropics. Because of the existence of spinup process, ensemble simulations in the tropics may have biases in the diurnal precipitation cycle if all the ensemble members are started from a single local time, as shown in Figs. 2.4 and 4.3. However, we notice a different local time for the precipitation peak between these figures. In Fig. 2.4, which is composite over 2-month period, we see that the maximum precipitation rate occurs before midnight, while in Fig. 4.3, which is a 5-day composite, the maximum of precipitation rate occurs in the early morning. In other words, there is a local time shift of precipitation peak in composite time series between two-month and five-day data. This shift is manifestation

of a midnight enhancement of precipitation on the northern coast of Java and southward propagation of enhanced precipitation signal in the ocean region to the north of Java (Fig. 4.9). The midnight enhanced precipitation is probably also related to the active period of the northwest monsoon associated with a cross-equatorial cold surge.

Cumulative distributions are a commonly used in statistical analyses to describe the probability distribution of a variable. There have been many studies to date that applied analysis methods with CDFs to hydrology. However, to our knowledge, little has been done in analyzing tropical precipitation on the time scale of less than a day. In the present study, we employ CDF to analyze the characteristic statistical features of heavy precipitation in January–February 2007. In Chapter 3, CDFs allowed us to see the modulation of the probability of rainfall rate based on the samples over the land region of West Java with all ensemble members for each pentad as shown in Fig. 3.13. This indicates the possibility of using this kind of quantity for forecasting heavy precipitation in the future as a product of ensemble forecasts. In Chapter 4, we have analyzed the CDFs of precipitation rate for four different regions: the ocean, the northern coast, the mountains, and the southern coast. The distinct statistical nature of heavy precipitation for the four regions can be seen in the CDFs shown in Fig. 4.12. This is a positive indication that CDF can be used to distinguish precipitation over the different regions.

Chapter 6

General Conclusions

We have carried out a numerical experiment on the modulation of precipitation over West Java in the two-month period of January–February 2007, which includes the Jakarta flood event in 31 January–4 February, in order to describe the temporal modulation of heavy precipitation over West Java and related three-dimensional structures due to cross-equatorial monsoon surges around Southeast Asia. Based on the ensemble simulations data, we investigated the temporal modulation of precipitation and three-dimensional synoptic fields in which these subjects were not addressed by previous studies. A comparison between the numerical results and the TRMM 3B42 data shows a fundamental agreement on the temporal modulation of the spatial distributions of precipitation, as well as the surface winds in the model and the QuikSCAT data. In the two-month period of simulation, a clear evidence of synoptic-scale disturbances interaction between a cold surge and a Borneo vortex and their impact on heavy precipitation was found. The impact of the cross-equatorial monsoon surge on precipitation over the Java Sea and Java was more significant when accompanied by a cold anomaly. The depth of the cold surge and the Borneo vortex is shallow as revealed from the vertical structures of the synoptic fields. In addition, we employed a statistical method to investigate the modulation of the CDFs. We found that pentad 7 (31 Jan-4 Feb) marked one of the highest values for the contribution of heavy precipitation.

In order to obtain further understanding of heavy precipitation during the Jakarta flood event, in Chapter 4, we describe time-lagged ensemble downscaling experiments for the crucial five-day period (31 January-4 February 2007) of the Jakarta flood event. We analyze the dependence of precipitation distribution simulated by the model on the horizontal resolutions (2, 4, 5, and 20 km). The results demonstrate the model's ability to reproduce a region of strong convective activity to the north of Java. Daily meridional propagation of enhanced precipitation signals is obtained for 2- and 4-km resolutions. We have moreover analyzed the CDFs of precipitation rate for four different regions: the ocean, the northern coast, the mountains, and the southern coast. The northern coast shows the highest contribution of heavy precipitation compared to the other regions for all the experiments as well as for satellite-based precipitation estimates. The diurnal variation of heavy precipitation produced by the 2-km resolution model agrees well in terms of the timing and location of the diurnal cycle with that of the satellite-based precipitation estimates.

This work focused on the extreme rainfall event that occurred in January–February 2007, using a regional non-hydrostatic model. It was our intention to create better understanding of extreme precipitation events over the region and synoptic circulations that modulate these events. We have employed a relatively new yet manageable and useful method to accomplish this study — a time-lagged ensemble technique. In particular, we have analyzed the relationship between synoptic-scale events such as a cold surge and a Borneo vortex and mesoscale intensive rainfall. This work on the interaction of synoptic-scale disturbances and their impact on convection and precipitation over a region should be shared with field researchers who study the Asian monsoon, diurnal-cycle, and weather prediction in Maritime Continent.

We have introduced cumulative distribution functions (CDFs) as a method of analysis in order to reveal statistical nature of heavy precipitation. There is a possibility of using this kind of quantity for forecasting heavy precipitation in the future as a product of ensemble forecasts. Further investigations with ensemble hindcast datasets are needed to examine the effect of cumulus parameterization on the statistical distribution of the

heavy precipitation. Further numerical experiments with 4- and 5-km resolutions with and without cumulus parameterization are needed in order to clarify the dependency of model-simulated heavy precipitation on horizontal resolutions and parameterization scheme.

List of publications

The thesis is based on the two articles listed below.

1. A time-lagged ensemble simulation on the modulation of precipitation over West Java in January–February 2007
   Monthly Weather Review, 2011, doi: 10.1175/MWR-D-11-00094.1 (in press)
   Nurjanna J. Trilaksono, Shigenori Otsuka, and Shigeo Yoden

2. Dependence of model-simulated heavy rainfall on the horizontal resolution during the Jakarta flood event in January–February 2007
   SOLA, 7, 193–196, 2011, doi: 10.2151/sola.2011-049
   Nurjanna J. Trilaksono, Shigenori Otsuka, Shigeo Yoden, Kazuo Saito, and Syugo Hayashi.

The numerical experiments and analyses in all the papers are carried out by Nurjanna Joko Trilaksono with the guidance, assistance, and discussion from Prof. Shigeo Yoden and Dr. Shigenori Otsuka. The guidance and assistance on the model specifications and parameter settings of the JMA-NHM in the second paper are provided by Dr. Kazuo Saito and Mr. Syugo Hayashi. Basically, the materials described in Chapter 3 of this thesis are based on the first article, whereas those in Chapter 4 are based on the second and the third articles.

Appendix A

Figure to complement Section 3.3.1

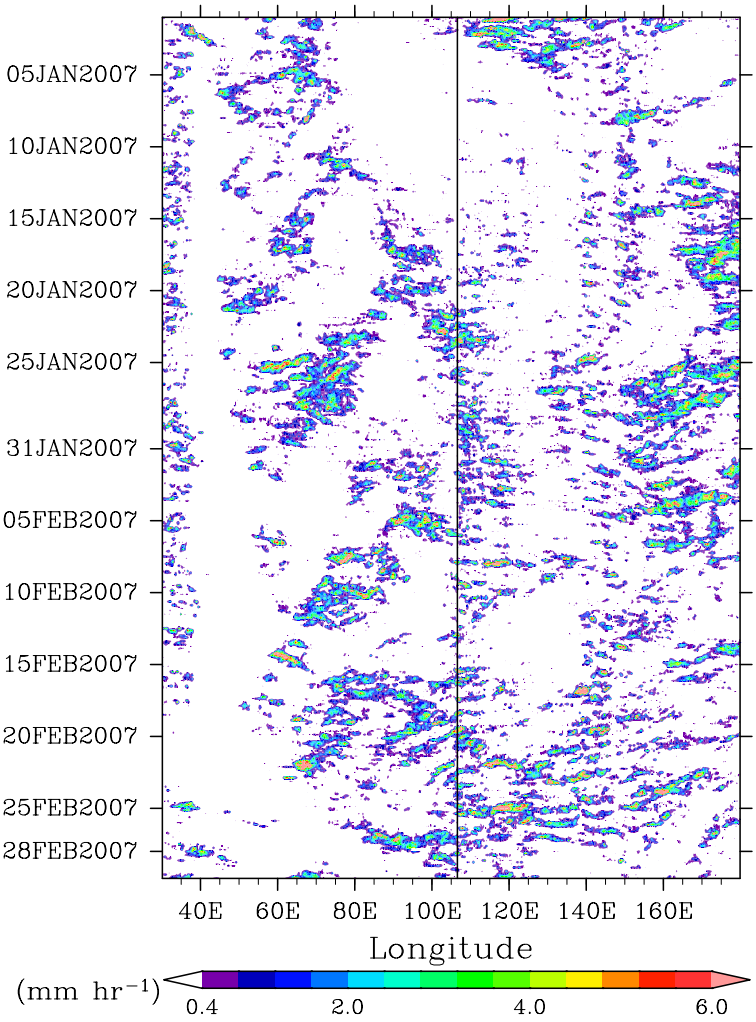

Figure A.1: Time–longitude cross sections of the TRMM data averaged between 5.5°and 8°S. The vertical line denote the longitude of 106.6°E.

Appendix B

Figure to complement Section 4.3.3

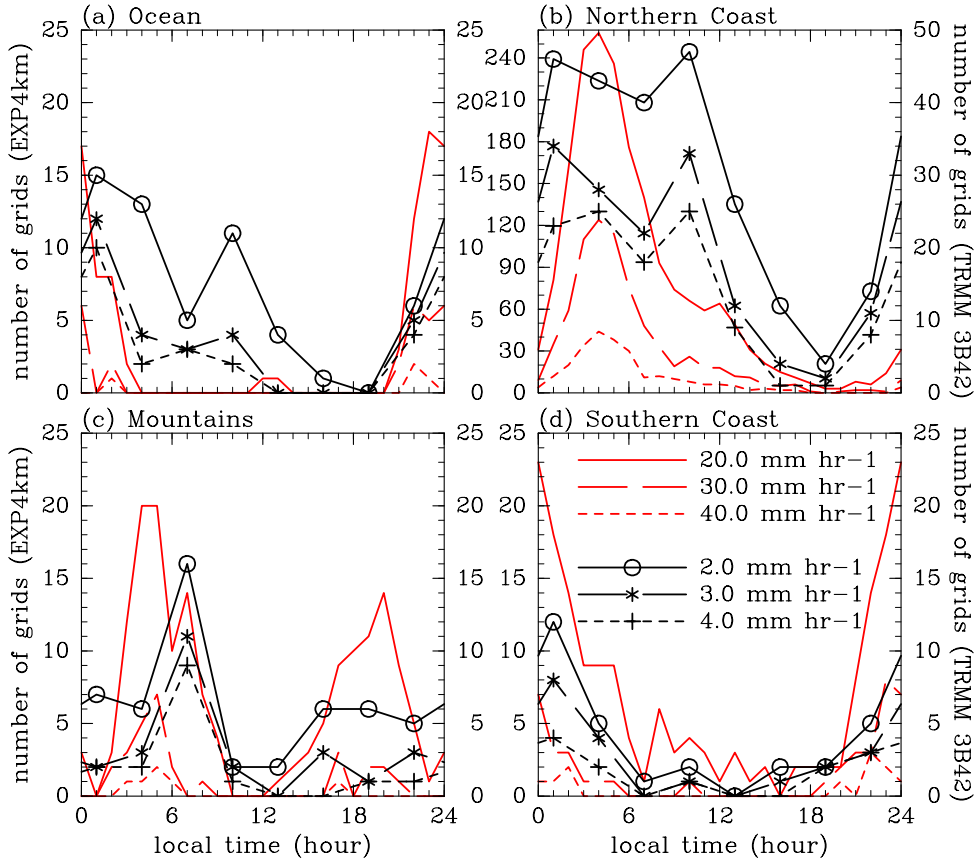

Figure B.1: The frequency of heavy precipitation as a function of local time for TRMM 3B42 (black lines with symbols) and all the ensemble members of EXP4km (red lines) over (a) the ocean, (b) the northern coast, (c) the mountains, and (d) the southern coast. See Fig. 4.13 for detailed caption.

References

Albright, M. D., D. R. Mock, E. E. Recker, and R. J. Reed, 1981: A diagnostic study of the diurnal rainfall variation in the GATE B-scale area. *J. Atmos. Sci.*, **38**, 1429–1445.

Albright, M. D., E. E. Recker, R. J. Reed, and R. Dang, 1985: The diurnal variation of deep convection and inferred precipitation in the central tropical Pacific during January–February 1979. *Mon. Wea. Rev.*, **113**, 1663–1680.

Aldrian, E. and R. D. Susanto, 2003: Identification of three dominant rainfall regions within Indonesia and their relationship to sea surface temperature. *Int. J. Climatol.*, **23**, 1435–1452.

BAPPENAS, 2007: Report on damage and loss assessment post flood disaster in early February 2007 in JABODETABEK region (Jakarta, Bogor, Depok, Tangerang, and Bekasi). Tech. rep., Ministry of National Development Planning/National Development Planning Agency of Indonesia, 63 pp. (in Bahasa Indonesia).

Barros, A., G. Kim, E. Williams, and S. Nesbitt, 2004: Probing orographic controls in the Himalayas during the monsoon using satellite imagery. *Natural Hazards and Earth System Sciences*, **4**, 29–51.

Boyle, J. S. and T.-J. Chen, 1987: Synoptic aspects of the wintertime East Asian monsoon. *Monsoon Meteorology*, C.-P. Chang and T. N. Krishnamurti, Eds., Oxford University Press., 125–160.

Brakenridge, G. R., cited 2011: Global active archive of large flood events.

Dartmouth Flood Observatory, University of Colorado, [Available online at http://floodobservatory.colorado.edu/Archives/index.html].

Branković, Č., T. N. Palmer, F. Molteni, S. Tibaldi, and U. Cubasch, 1990: Extended-range predictions with ECMWF models: Time-lagged ensemble forecasting. *Quart. J. Roy. Meteor. Soc.*, **116**, 867–912.

Chang, C.-P., P. A. Harr, and H.-J. Chen, 2005: Synoptic disturbances over the equatorial South China Sea and western Maritime Continent during boreal winter. *Mon. Wea. Rev.*, **133**, 489–503.

Chang, C.-P., C. H. Liu, and H. C. Kuo, 2003: Typhoon Vamei: An equatorial tropical cyclone formation. *Geophys. Res. Lett.*, **30**, 1150, doi:10.1029/2002GL016365.

Cheang, B. K., 1977: Synoptic features and structures of some equatorial vortices over the South China Sea in the Malaysian region during the winter monsoon of December 1973. *Pure Appl. Geophys.*, **115**, 1303–1333.

Chelton, D. B. and M. H. Freilich, 2005: Scatterometer-based assessment of 10-m wind analyses from the operational ECMWF and NCEP numerical weather prediction models. *Mon. Wea. Rev.*, **133**, 409–429.

Chen, G. T. J., T. E. Gerish, and C.-P. Chang, 1986: Structure variations of the synoptic-scale cyclonic disturbances near Borneo during the WMONEX period. *Pap. Meteor. Res.*, **9**, 117–135.

Chen, S. S. and R. A. Houze, Jr., 1997: Diurnal variation and life-cycle of deep convective systems over the tropical Pacific warm pool. *Quart. J. Roy. Meteor. Soc.*, **123**, 357–388.

Cifelli, R., S. Nesbitt, S. Rutledge, W. Petersen, and S. Yuter, 2008: Diurnal characteristics of precipitation features over the tropical East Pacific: A comparison of the EPIC and TEPPS regions. *J. Climate*, **21**, 4068–4086.

Compo, G. P., G. N. Kiladis, and P. J. Webster, 1999: The horizontal and vertical structure of east Asian winter monsoon pressure surges. *Quart. J. Roy. Meteor. Soc.*, **125**, 29–54.

Dilley, M., and Coauthors, 2005: *Natural Disaster Hotspots: A Global Risk Analysis*, Disaster Risk Management Series, Vol. 5. The World Bank and Columbia University, 148 pp.

Freilich, M. H. and R. S. Dunbar, 1999: The accuracy of the NSCAT 1 vector winds: Comparisons with National Data Buoy Center buoys. *J. Geophys. Res.*, **104**, 11 231–11 246.

Garratt, J. R. and R. J. Francey, 1978: Bulk characteristics of the heat transfer in the unstable baroclinic atmospheric boundary layer. *Bound.-Layer Meteor.*, **15**, 399–421.

Gray, W. M. and R. W. Jacobson, 1977: Diurnal variation of deep cumulus convection. *Mon. Wea. Rev*, **105**, 1171–1188.

Hamada, J.-I., M. D. Yamanaka, J. Matsumoto, S. Fukao, P. A. Winarso, and T. Sribimawati, 2002: Spatial and temporal variations of the rainy season over Indonesia and their link to ENSO. *J. Meteor. Soc. Japan*, **80**, 285–310.

Hattori, M., S. Mori, and J. Matsumoto, 2011: The cross-equatorial northerly surge over the Maritime Continent and its relationship to precipitation patterns. *J. Meteor. Soc. Japan*, **89A**, 27–47, doi:10.2151/jmsj.2011-A02.

Hayashi, S., 2011: Statistical verification of short-range forecasts by the NHM and WRF-ARW models with fine resolution. *International Research for Prevention and Mitigation of Meteorological Disasters in Southeast Asia*, MRI, Tech. Rep. MRI, chap. C-2, in press.

Hayashi, S., K. Aranami, and K. Saito, 2008: Statistical verification of short term NWP by NHM and WRF-ARW with 20 km horizontal resolution around Japan and Southeast Asia. *SOLA*, **4**, 133–136.

Hendon, H. H., 2003: Indonesian rainfall variability: Impacts of ENSO and local air-sea interaction. *J. Climate*, **16**, 1775–1790.

Hendon, H. H. and K. Woodberry, 1993: The diurnal cycle of tropical convection. *J. Geophys. Res.*, **98**, 16 523–16 637.

Hirose, M. and K. Nakamura, 2005: Spatial and diurnal variation of precipitation systems over Asia observed by the TRMM Precipitation Radar. *J. Geophys. Res.*, **110**, D05106, doi:10.1029/2004JD004815.

Hirose, M., R. Oki, S. Shimizu, M. Kachi, and T.Higashiuwatoko, 2008: Finescale diurnal rainfall statistics refined from eight years of TRMM PR data. *J. Appl. Meteor. Climatol.*, **47**, 544–561.

Hoffman, R. N. and E. Kalnay, 1983: Lagged average forecasting, an alternative to Monte Carlo forecasting. *Tellus*, **35A**, 100–118.

Houze, R. A., Jr., S. G. Geotis, F. D. Marks, Jr., and A. K. West, 1981: Winter monsoon convection in the vicinity of north Borneo. Part I: Structure and time variation of the clouds and precipitation. *Mon. Wea. Rev.*, **109**, 1595–1614.

Houze, R. A., Jr., D. Wilton, and B. Smull, 2007: Monsoon convection in the Himalayan region as seen by the TRMM Precipitation Radar. *Quart. J. Roy. Meteor. Soc.*, **133**, 1389–1411.

Huffman, G. J., and Coauthors, 2007: The TRMM multisatellite precipitation analysis (TMPA): Quasi-global, multiyear, combined-sensor precipitation estimates at fine scales. *J. Hydrometeor.*, **8**, 38–55.

Ikawa, M. and K. Saito, 1991: Description of a non-hydrostatic model developed at the Forecast Research Department of the MRI. MRI Tech. Rep. Vol. 28, Meteorological Research Institute, JMA, 238 pp.

JMA, cited 2011: New geostationary meteorological satellite - Multi-functional Transport Satellite (MTSAT) series -. JMA, [Available online at http://ds.data.jma.go.jp/obd/sat/data/web/brochure2.pdf].

Johnson, R. H. and R. A. J. Houze, 1987: Precipitating cloud systems of the Asian monsoon. *Monsoon Meteorology*, C.-P. Chang and T. N. Krishnamurti, Eds., Oxford University Press., 298–353.

Juneng, L., F. T. Tangang, and C. J. C. Reason, 2007: Numerical case study of an extreme rainfall event during 9–11 December 2004 over the east coast Peninsular Malaysia. *Meteorol. Atmos. Phys.*, **98**, 81–98.

Kain, J., 2004: The Kain–Fritsch convective parameterization: An update. *J. Appl. Meteor.*, **43**, 170–181.

Kato, T., 1995: Box-Lagrangian rain-drop scheme. *J. Meteor. Soc. Japan*, **73**, 97–128.

Kitagawa, H., 2000: Radiation processes. NPD Rep. Vol. 46, Numerical Prediction Division, JMA, 16-31 pp. (in Japanese).

Koh, T.-Y. and C.-K. Teo, 2009: Toward a mesoscale observation network in Southeast Asia. *Bull. Amer. Meteor. Soc.*, **90**, 481–488.

Lau, K.-M. and C.-P. Chang, 1987: Planetary scale aspects of winter monsoon and teleconnections. *Monsoon Meteorology*, C.-P. Chang and T. N. Krishnamurti, Eds., Oxford University Press, 161–202.

Liebmann, B. and C. A. Smith, 1996: Description of a complete (interpolated) Outgoing Longwave Radiation dataset. *Bull. Amer. Meteor. Soc.*, **77**, 1275–1277.

Lin, Y. H., R. D. Farley, and H. D. Orville, 1983: Bulk parameterization of the snow field in a cloud model. *J. Climate Appl. Meteor.*, **22**, 1065–1092.

Liu, C., E. J. Zipser, and S. W. Nesbitt, 2007: Global distribution of tropical deep convection: different perspectives from TRMM infrared and radar data. *J. Climate*, **20**, 489–503.

Louis, J. F., M. Tiedtke, and J. F. Geleyn, 1982: A short history of the operational PBL parameterization at ECMWF. *Workshop on Planetary Boundary Layer Parameterization*, England, ECMWF, 59–79.

Mapes, B., T. Warner, M. Xu, and A. Negri, 2003: Diurnal patterns of rainfall in northwestern South America. part I: Observations and context. *Mon. Wea. Rev.*, **131**, 799–812.

Matsumoto, J., 1997: Seasonal transition of summer rainy season over indochina and adjacent monsoon region. *Adv. Atmos. Sci*, **14**, 231–245.

McGarry, M. M. and R. J. Reed, 1978: Diurnal variations in convective activity and precipitation during phases II and III of GATE. *Mon. Wea. Rev*, **106**, 101–113.

Mittermaier, M. P., 2007: Improving short-range high-resolution model precipitation forecast skill using time-lagged ensembles. *Quart. J. Roy. Meteor. Soc.*, **133**, 1487–1500.

Mori, S., and Coauthors, 2004: Diurnal land-sea rainfall peak migration over Sumatera Island, Indonesian Maritime Continent, observed by TRMM satellite and intensive rawinsonde soundings. *Mon. Wea. Rev.*, **132**, 2021–2039.

Nakanishi, M. and H. Niino, 2004: An improved Mellor–Yamada level 3 model with condensation physics: Its design and verification. *Bound.-Layer Meteor.*, **112**, 1–31.

Nakanishi, M. and H. Niino, 2006: An improved Mellor–yamada level-3 model: Its numerical stability and application to a regional prediction of advection fog. *Bound.-Layer Meteor.*, **119**, 397–407.

Nesbitt, S. and E. Zipser, 2003: The diurnal cycle of rainfall and convective intensity according to three years of TRMM measurements. *J. Climate*, **16**, 1456–1475.

Ohmori, S. and Y. Yamada, 2004: Implementation of the Kain–Fritsch convective parameterization scheme in JMA's non-hydrostatic model. *CAS/JSC WGNE Res. Activ. Atmos. Oceanic Modell.*, **34**, 0425–0426.

Otsuka, S. and S. Yoden, 2005: Numerical experiments on the layered structures in the mid-troposphere over the equatorial Pacific. *SOLA*, **1**, 69–72.

Romatschke, U., S. Medina, and R. A. Houze, Jr., 2010: Regional, seasonal, and diurnal variations of extreme convection in the South Asian region. *J. Climate*, **23**, 419–439.

Saito, K., 1994: A numerical study of the local downslope wind "Yamaji-kaze" in Japan. Part 3: Numerical simulation of the 27 September 1991 windstorm with a non-hydrostatic multinested model. *J. Meteor. Soc. Japan*, **72**, 301–329.

Saito, K., H. Eito, and C. Muroi, 2001a: Documentation of the Meteorological Research Institute/Numerical Prediction Division unified nonhydrostatic model. Mri tech. rep., Meteorological Research Institute, JMA, 133 pp.

Saito, K., J. Ishida, K. Aranami, T. Hara, T. Segawa, M. Narita, and Y. Honda, 2007: Nonhydrostatic atmospheric models and operational development at JMA. *J. Meteor. Soc. Japan*, **85B**, 271–304.

Saito, K., T. Keenan, G. Holland, and K. Puri, 2001b: Numerical simulation of the diurnal evolution of tropical island convection over the Maritime Continent. *Mon. Wea. Rev.*, **129**, 378–400.

Saito, K., and Coauthors, 2006: The operational JMA nonhydrostatic mesoscale model. *Mon. Wea. Rev.*, **134**, 1266–1298.

Seko, H., S. Hayashi, M. Kunii, and K. Saito, 2008: Structure of the regional heavy rainfall system that occurred in Mumbai, India, on 26 July 2005. *SOLA*, **4**, 129–132.

Simpson, J., C. Kummerow, W.-K. Tao, and R. F. Adler, 1996: On the tropical rainfall measuring mission (TRMM). *Meteorol. Atmos. Phys.*, **60**, 19–36.

Sugi, M., K. Kuma, K. Tada, K. Tamiya, N. Hasegawa, T. Iwasaki, S. Yamada, and T. Kitade, 1990: Description and performance of the JMA operational global spectral model (JMA-GSM88). *Geophys. Mag.*, **43**, 105–130.

Suppiah, R. and X. Wu, 1998: Surges, cross-equatorial flows and their links with the Australian summer monsoon circulation and rainfall. *Aust. Met. Mag.*, **47**, 113–130.

Tangang, F. T., L. Juneng, E. Salimun, P. N. Vinayachandran, Y. K. Seng, C. J. C. Reason, S. K. Behera, and T. Yasunari, 2008: On the roles of the northeast cold surge, the Borneo vortex, the Madden-Julian Oscillation, and the Indian Ocean Dipole during the extreme 2006/2007 flood in southern Peninsular Malaysia. *Geophys. Res. Lett.*, **35**, L14S07, doi:10.1029/2008GL033429.

Wang, B. and LinHo, 2002: Rainy season of the Asian-Pacific summer monsoon. *J. Climate*, **15**, 386–398.

Wangwongchai, A., S. Zhao, and Q. Zeng, 2005: A case study on a strong tropical disturbance and record heavy rainfall in Hat Yai, Thailand during winter monsoon. *Adv. Atmos. Sci.*, **20**, 436–450.

Wheeler, M. C. and H. H. Hendon, 2004: An all-season real-time multivariate MJO index: Development of an index for monitoring and prediction. *Mon. Wea. Rev.*, **132**, 1917–1932.

Wilks, D. S., 2006: *Statistical methods in the atmospheric sciences*, International Geophysics Series, Vol. 91. 2nd ed., Academic Press, 627 pp.

Wu, M. C. and J. C. L. Chan, 1995: Surface features of winter monsoon surges over South China. *Mon. Wea. Rev.*, **123**, 662–680.

Wu, M. C. and J. C. L. Chan, 1997: Upper-level features associated with winter monsoon surges over South China. *Mon. Wea. Rev.*, **125**, 317–340.

Wu, P., M. Hara, H. Fudeyasu, M. D. Yamanaka, J. Matsumoto, F. Syamsudin, R. Sulistyowati, and Y. S. Djajadihardja, 2007: The impact of trans-equatorial monsoon flow on the formation of repeated torrential rains over Java Island. *SOLA*, **3**, 93–96.

Yabu, S., S. Murai, and H. Kitagawa, 2005: Clear-sky radiation scheme. NPD Rep. Vol. 51, Numerical Prediction Division, JMA, 53-64 pp. (in Japanese).

Yang, G.-Y. and J. Slingo, 2001: The diurnal cycle in the tropics. *Mon. Wea. Rev.*, **129**, 784–801.

Yoden, S., 2007: Atmospheric predictability. *J. Meteor. Soc. Japan*, **85B**, 77–102.